AN INTEGRATED SYNTHETIC APERTURE RADAR/ GLOBAL POSITIONING SYSTEM/ INERTIAL NAVIGATION SYSTEM FOR TARGET GEOLOCATION IMPROVEMENT

THESIS

Brian James Young
Captain, United States Air Force

AFIT/GE/ENG/99M-32

Approved for public release; distribution unlimited

AFIT/GE/ENG/99M-32

AN INTEGRATED SYNTHETIC APERTURE RADAR/GLOBAL POSITIONING SYSTEM/INERTIAL NAVIGATION SYSTEM FOR TARGET GEOLOCATION IMPROVEMENT

THESIS

Presented to the Faculty of the Graduate School of Engineering

of the Air Force Institute of Technology

In Partial Fulfillment of the

Requirements for the Degree of

Master of Science in Electrical Engineering

Brian James Young, B.S.E.E.

Captain, United States Air Force

March, 1999

Approved for public release; distribution unlimited

AFIT/GE/ENG/99M-32

AN INTEGRATED SYNTHETIC APERTURE RADAR/GLOBAL POSITIONING SYSTEM/INERTIAL NAVIGATION SYSTEM FOR TARGET GEOLOCATION IMPROVEMENT

Brian James Young, B.S.E.E
Captain, United States Air Force

Approved:

_____ _____
Major Mikel M. Miller Date
Assistant Professor, Thesis Advisor

_____ _____
Captain John Raquet Date
Assistant Professor, Thesis Reader

Preface

First and foremost, I would like to thank my wife Corina for enduring another round of long days, late nights, and all around time away from home. I could not have done this without her support. Sometimes I wonder how the single guys take the pressure of AFIT without having someone to come home to every night. My children, Sara, Sadie, and Kemper, all deserve thanks as well. Daddy will be less pre-occupied from now on!!

My thesis advisor, Major Mikel Miller deserves a lot of credit for this body of work. He was always there to give encouragement and keep me focused on the most important aspects of the work and not the tiny, exasperating problems associated with working in Fortran. Being his first thesis student, I was a little apprehensive, but he more than made up for any initial jitters by being constantly available even though he was the busiest professor at AFIT. Thank you for the advice both personal and professional.

Dr. Pete Maybeck, Captain John Raquet, and Stan Musick also deserve credit for getting this work out the door. Dr. Maybeck is the premier Kalman filter wealth of knowledge in the world and it was truly an honor to have him review my work. Thank you for getting me off on the right foot. Capt Raquet was always there to test new ideas and concepts for this research. Without his constant help in the beginning, I don't think it would have been possible to perform this research. Stan, you truly are the god of MSOFE and it is a credit to you that you are still willing to help new users!

Thanks to my classmates in the guidance and control department: Lt Barry Vanek, Lt Jamey Sillence, Lt Ken Fisher, Capt Steve Chastain, and Capt Andy Proud. Late nights in the lab, BW3 on Tuesdays, and the regular daily grind made us all friends, lets keep it that way. A special thanks to Barry for being the constant voice of reason.

Table of Contents

Page

Preface i

Table of Contents ii

List of Figures vi

List of Tables viii

Abstract x

1. Introduction 1-1

1.1. Background 1-2

1.1.1. Inertial Navigation Systems 1-2

1.1.2. Global Positioning System 1-3

1.1.3. Synthetic Aperture Radar 1-4

1.1.4. System Integration and Kalman Filtering 1-6

1.1.5. Integration Methods 1-6

1.2. Current Research 1-7

1.3. Problem Definition 1-9

1.4. Scope 1-10

1.5. Assumptions 1-11

1.6. Literature Review 1-13

1.6.1. Sensor Fusion 1-13

1.6.2. Airborne Mapping 1-14

1.6.3. Multi- Sensor / Multi-Target Tracking 1-14

1.7. Methodology Overview 1-15

1.8. Overview of Thesis 1-16

1.9. Summary 1-17

2. Theory 2-1

2.1. Overview 2-1

2.2. Extended Kalman Filter 2-1

Page

2.2.1. State and Measurement Model Equations 2-2
2.2.2. State and Measurement Model Linearization 2-2
2.2.3. Extended Kalman Filter Equations 2-4
2.2.4. Truth Model 2-6
2.2.5. Filter Model 2-7
2.2.5.1. Order Reduction 2-8
2.2.5.2. Filter Tuning 2-9
2.3. System Integration 2-11
2.4. Coordinate Frame Transformations 2-13
2.4.1. Inertial to ECEF 2-14
2.4.2. ECEF to Navigation 2-15
2.4.3. Wander Azimuth Reference Frame 2-16
2.4.4. Other Reference Frames 2-17
2.4.5. Reference Frame Perturbation 2-18
2.5. Summary 2-20

3. Modeling Methodology 3-1

3.1. Overview 3-1
3.2. Overall System Description 3-1
3.3. Inertial Navigation System Model 3-4
3.4. Barometric / Radar Altimeter Model 3-6
3.5. Global Positioning System Model 3-7
3.5.1. Stand-Alone GPS 3-8
3.5.1.1. Stand-Alone GPS Error Model Equations 3-8
3.5.1.2. Stand-Alone GPS Measurement Model 3-11
3.5.2. Differential GPS 3-13
3.5.2.1. Differential GPS Error Model Equations 3-14
3.5.2.2. Differential GPS Measurement Model 3-15
3.5.3. Carrier Phase Differential GPS 3-16
3.5.3.1. Carrier Phase Differential GPS Error Model Equations 3-19
3.5.3.2. Carrier Phase Differential GPS Measurement Model 3-20
3.6. Synthetic Aperture Radar Model 3-21
3.6.1. SAR Error Model 3-23

3.6.2. SAR Measurement Model 3-25

Page

3.7. Integrated System Models 3-29
3.7.1. Integrated Truth Model 3-30
3.7.2. Integrated Filter Model 3-31
3.7.3. Integrated System/Filter Measurement Model 3-33
3.8. Simulation Software 3-33
3.8.1. MSOFE 3-34
3.8.2. MPLOT 3-35
3.8.3. PROFGEN 3-36
3.8.4. GPSADD 3-37
3.9. Summary 3-37

4. Simulation Results 4-1

4.1. Overview 4-1
4.2. U-2 Flight Profile 4-1
4.3. Case Definition 4-3
4.3.1. Case 1, Stand-Alone GPS 4-4
4.3.2. Case 2, Differential GPS 4-4
4.3.3. Case 3, Carrier-Phase GPS 4-5
4.4. Simulation Results 4-5
4.4.1. Case 1 4-7
4.4.1.1. Aircraft Position/Velocity/Attitude Accuracy 4-7
4.4.1.2. Target Position Accuracy 4-10
4.4.2. Case 2 4-12
4.4.2.1. Aircraft Position/Velocity/Attitude Accuracy 4-12
4.4.2.2. Target Position Accuracy 4-14
4.4.3. Case 3 4-15
4.4.3.1. Aircraft Position/Velocity/Attitude Accuracy 4-16
4.4.3.2. Target Position Accuracy 4-18
4.4.4. Cross-Case Comparison 4-19
4.5. Summary 4-21

5. Conclusions 5-1

5.1. Overview 5-1

5.2. Conclusions 5-1

Page

5.3. Recommendations 5-3

Appendix A. Acronym List A-1

Appendix B. Model State Definitions and System Matrices B-1

B.1. Truth Model Error States B-1

B.2. Simulation Filter States B-2

B.3. Model Dynamics and Noise Matrices [2, 8] B-2

B.4. Tuning Values B-2

Appendix C. Stand-Alone GPS Results C-1

Appendix D. Differential GPS Results D-1

Appendix E. Carrier Phase GPS Results E-1

Appendix F. Flight Profile Plots F-1

Bibliography BIB-1

Vita VIT-1

List of Figures

Page

Figure 1. GPS Scenario....1-4
Figure 2. Synthetic Aperture Radar Techniques....1-5
Figure 3. Tight vs. Loose Integration....1-8
Figure 4. Loose INS/GPS Integration....2-12
Figure 5. Tight INS/GPS Integration....2-13
Figure 6. Inertial/ECEF Reference Frame Geometry....2-14
Figure 7. ECEF/Navigation Frame Geometry....2-16
Figure 8. GPS/INS/SAR Integrated Block Diagram....3-2
Figure 9. Stand-Alone GPS Technique....3-9
Figure 10. Differential GPS Technique....3-14
Figure 11. Carrier Phase GPS Scenario [20]....3-18
Figure 12. U-2 Flight Profile and Targeting Scenario....4-2
Figure 13. Plot Legend....4-6
Figure 14. SGPS Aircraft Position Error Estimates....4-8
Figure 15. SGPS User Clock Bias Error Estimate....4-10
Figure 16. SGPS Target Position Accuracy....4-11
Figure 17. DGPS Aircraft Position Error Estimates....4-13
Figure 18. DGPS Target Position Accuracy....4-15
Figure 19. CPGPS Aircraft Position Error Estimates....4-17
Figure 20. CPGPS Target Position Accuracy....4-18
Figure 21. Case-by-Case Integrated System Summary....4-22
Figure 22. SGPS Latitude and Longitude Errors....C-2
Figure 23. SGPS Altitude and Barometric Altimeter Bias Errors....C-3
Figure 24. SGPS User Clock Bias and Clock Bias Drift Errors....C-4
Figure 25. SGPS North, East, and Down Velocity Errors....C-5
Figure 26. SGPS North, East, and Down Attitude Errors....C-6
Figure 27. SGPS SAR X, Y, and Z-Target Position Errors....C-7
Figure 28. SGPS SAR Range and Range Rate Bias Errors....C-8

Page

Figure 29. DGPS Latitude and Longitude Errors D-2
Figure 30. DGPS Altitude and Barometric Altimeter Bias Errors D-3
Figure 31. DGPS User Clock Bias and Clock Bias Drift Errors D-4
Figure 32. DGPS North, East, and Down Velocity Errors D-5
Figure 33. DGPS North, East, and Down Attitude Errors D-6
Figure 34. DGPS SAR X, Y, and Z-Target Position Errors D-7
Figure 35. DGPS SAR Range and Range Rate Bias Errors D-8
Figure 36. CPGPS Latitude and Longitude Errors E-2
Figure 37. CPGPS Altitude and Barometric Altimeter Bias Errors E-3
Figure 38. CPGPS North, East, and Down Velocity Errors E-4
Figure 39. CPGPS North, East, and Down Attitude Errors E-5
Figure 40. CPGPS SAR X, Y, and Z-Target Position Errors E-6
Figure 41. CPGPS SAR Range and Range Rate Bias Errors E-7
Figure 42. CPGPS Carrier Phase Ambiguity Errors E-8
Figure 43. U-2 Flight Profile Latitude, Longitude, and Altitude F-2
Figure 44. U-2 Flight Profile 2-D Position, Velocity Magnitude, and Wander Angle F-3
Figure 45. U-2 Flight Profile X-, Y-, and Z-Velocities F-4
Figure 46. U-2 Flight Profile Roll, Pitch, and Yaw Angles F-5
Figure 47. U-2 Flight Profile Roll, Pitch, and Yaw Rates F-6

List of Tables

Page

Table 1. SAR Performance Characteristics 3-29
Table 2. Integrated Truth Model States 3-30
Table 3. Integrated Filter Model States 3-31
Table 4. SGPS Aircraft Errors 4-7
Table 5. SGPS Targeting Errors 4-10
Table 6. DGPS Aircraft Errors 4-13
Table 7. DGPS Targeting Errors 4-14
Table 8. CPGPS Aircraft Errors 4-16
Table 9. CPGPS Targeting Errors 4-18
Table 10. Error Analysis per GPS Type 4-19
Table 11. Velocity Error Analysis per GPS Type 4-20
Table 12. Target Geolocation Improvement by GPS Type 4-20
Table 13. Aircraft Location Improvement (SGPS Baseline) 4-21
Table 14. 93-State INS Truth Model, States 1-31 ..... B-4
Table 15. 93-State INS Truth Model, States 32-63 ..... B-5
Table 16. 93-State INS Truth Model, States 64-93 ..... B-6
Table 17. 39-State Reduced Order INS Truth Model, States 1-20 ..... B-7
Table 18. 39-State Reduced Order INS Truth Model, States 21-39 ..... B-8
Table 19. 30-State Stand-Alone GPS Truth Model B-9
Table 20. 22-State Differential GPS Truth Model B-10
Table 21. 4-State Carrier Phase GPS Truth Model B-11
Table 22. 6-State SAR Truth Model B-11
Table 23. Filter Model, Single/Differential GPS B-12
Table 24. Filter Model, Carrier Phase GPS B-13
Table 25. Elements of the Dynamics Submatrix F_{11} B-14
Table 26. Elements of the Dynamics Submatrix F_{12} B-15
Table 27. Elements of the Dynamics Submatrix F_{13} B-15
Table 28. Elements of the Dynamics Submatrix F_{14} B-16
Table 29. Elements of the Dynamics Submatrix F_{22} B-17

Page

Table 30. Non-Zero Elements of Process Noise Submatrix Q_{11} B-17
Table 31. Non-Zero Elements of Process Noise Submatrix Q_{22} B-18
Table 32. Measurement Noise Strengths, Truth and Filter B-19
Table 33. Tuning Values for Filter States, All GPS Models B-19

Abstract

A significant amount of military and civilian research has been aimed at the sensor fusion technology area. However, there has been little research into the fusion between synthetic aperture radar (SAR) sensors and navigation sensors like the inertial navigation sensor (INS) and the global positioning system (GPS). SAR is used in civilian and military applications to image ground based targets in reconnaissance and fighter targeting missions. The SAR range and range rate measurements are generally obtained and processed independently from the aircraft navigation system. This thesis explores a potential integration technique to fuse information from the navigation sensors with the SAR target measurements. Using Kalman filtering techniques, an INS/GPS/SAR integrated system was simulated in a single Kalman filter to analyze the SAR target geolocation accuracy benefits. Three different GPS receiver models were used in the integrated system: stand-alone, differential, and carrier-phase differential (using floating ambiguity resolution). Each of these GPS models were integrated with a common INS/SAR combination to determine the target geolocation accuracy improvements due only to GPS receiver type. Thesis results show that SAR targeting can be enhanced, through tight integration of an INS/GPS navigation system, without increasing the SAR resolution.

AN INTEGRATED SYNTHETIC APERTURE RADAR/GLOBAL POSITIONING SYSTEM/INERTIAL NAVIGATION SYSTEM FOR IMAGERY GEOLOCATION IMPROVEMENT

1. Introduction

Sensor fusion is an emerging technology in today's Air Force. From reconnaissance sensors to navigation sensors, tight sensor integration is showing improvement in aircraft avionics accuracy and targeting performance. Sensor fusion typically requires a Kalman Filter to combine the measurements from these sensors. To date, there has been very little research into the area of reconnaissance and navigation sensor fusion using Kalman Filter techniques. However, the Air Force Institute of Technology (AFIT) has provided a wealth of research and analysis regarding the benefits of Kalman Filtering as applied to navigation sensor fusion [1-3, 8, 11, 19-21, 23-25, 27-30]. This thesis extends previous AFIT research by combining synthetic aperture radar (SAR) measurements to an existing navigation Kalman Filter. The results of this research shows significant potential improvements in the targeting accuracy of the SAR without modifying the actual radar. This work, along with Layne [32], presents some of the first research into the potential real world performance improvements attainable with a tightly integrated Inertial Navigation System (INS), Global Positioning System (GPS), and SAR.

1.1. Background

There are four technology areas presented in this thesis: inertial navigation systems (INS), Global Positioning System (GPS), synthetic aperture radar (SAR), system integration, and Kalman filtering. A general overview of each of these topics is presented below.

1.1.1. Inertial Navigation Systems

Inertial navigation systems use the outputs of accelerometers and gyroscopes to provide an autonomous indication of aircraft position, velocity and attitude. Because the INS operates with respect to inertial space, it is theoretically not subject to errors associated with the earth's rotation, aircraft dynamics, or other sensors onboard the aircraft. There are two major types of INS implementations: platform and strapdown. A platform INS contains an inertially stabilized platform that uses gimbals to maintain its stability. A strapdown INS utilizes mathematical algorithms to determine a computational platform. In all INS implementations there are inherent instabilities in the vertical channel [13]. Usually, an altitude sensor, i.e. barometric or radar altimeter, is integrated with the INS to compensate for the instability. However, there are errors inherent to the design and fabrication of both platform and strapdown INSs that induce a drift in the INS indicated position, velocity, and attitude. These errors, small at first, can become large and will continue to drift with time unless the INS is corrected. Without additional position and velocity updates from off-board integrated sensors, the INS will drift and produce poor velocity and position information. Integration of GPS with an INS can provide the position and velocity updates needed to correct the INS drift.

1.1.2. Global Positioning System

The Global Positioning System is a constellation of 24 satellites that transmit electromagnetic signals to GPS receivers located on the user's platform. The GPS receiver determines the range between each satellite within view of the receiver and the user. The range provided by the receiver is called "pseudorange" due to presence of several signal errors. Each of these errors, including clock, atmospheric, bias, and drift, will be described in future sections. There are four unknown parameters involved with GPS positioning: three-dimension position parameters (x, y, and z) and GPS time. Therefore, as long as there are at least four GPS satellite vehicles (SV) within view of the receiver, the pseudoranges provided from the SVs are used to determine the user's position with respect to the earth. Figure 1 shows a typical GPS scenario. SV geometry plays an important part in GPS positioning. Poor SV geometry with respect to the receiver produces high geometric dilution of precision (GDOP) which can wreak havoc on GPS position solutions [12].

A GPS receiver's position and velocity output can be very accurate, but the accuracy depends heavily on the type of receiver. Civil single positioning service (SPS) receivers are subjected to selective availability (SA), an error injected into the GPS signal by the GPS Mission Control Segment. SA decreases the positioning accuracy of stand-alone receivers to within 100-meters RMS. Military receivers account for SA by using de-encryption techniques, providing position accuracy within 10-meters root-mean-square (RMS). Differential GPS (DGPS) receivers can provide accuracy within 3-meters CEP [12].

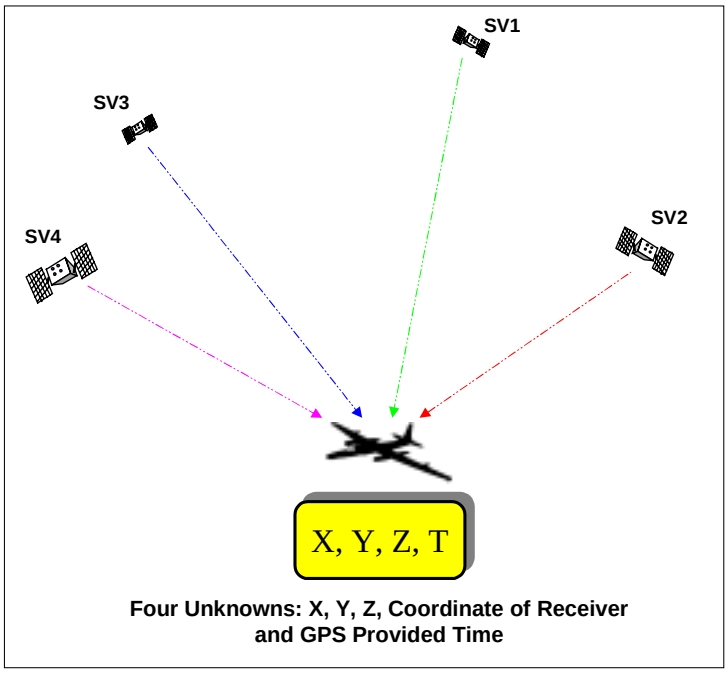

Figure 1. GPS Scenario

These receivers take advantage of differential correction signals that account for atmospheric errors, SA, and other errors. However, there must be a DGPS correction transmitter located within range of the DGPS receiver. Another type of receiver is a Carrier Phase Differential GPS (CPGPS) receiver. These receivers use the actual signal carrier frequency and phase to determine the position of the GPS receiver. CPGPS receivers have accuracies down in the 10-cm range and are considered the most accurate (i.e. generally more expensive) type of GPS receiver. All accuracies mentioned in this paragraph account for stationary positioning. Aircraft mounted GPS receivers are usually subjected to harsh, dynamic environments where sub-meter accuracy is hard to provide.

1.1.3. Synthetic Aperture Radar

One of the most widely used reconnaissance sensors is the synthetic aperture radar (SAR). The SAR produces high-resolution images of surface target areas and has the

ability to operate in all-weather conditions. Since SAR can operate through clouds, unlike electro-optical sensors, it is a key sensor for reconnaissance imagery [9]. Because radar imagery resolution is a function of the radar sensor's aperture, a larger aperture produces higher resolution imagery. A SAR uses the motion of the airborne platform to synthesize a large aperture antenna from the true, smaller aperture antenna. Typical SAR sensors provide two modes of operation: search and spotlight. In search mode, a SAR will radiate a swath of land providing a large area (and usually lower resolution) image. In spotlight mode, the SAR radiates a smaller area multiple times producing a higher resolution image. Figure 2 shows a typical SAR mission with both search and spotlight mode. A SAR utilizes typical radar techniques by measuring the time between the transmission and reception of a SAR signal [11]. SAR targets are typically designated prior to a reconnaissance mission; however, the SAR operator can image targets of opportunity any time during the mission.

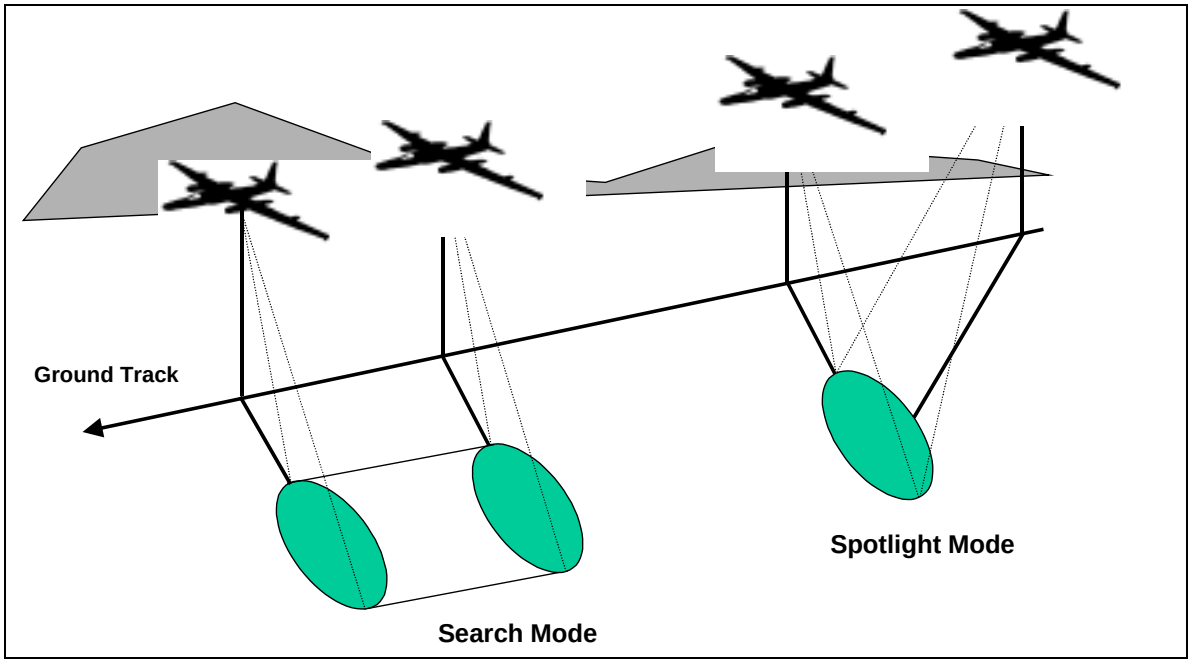

Figure 2. Synthetic Aperture Radar Techniques

1.1.4. System Integration and Kalman Filtering

There have been numerous AFIT Master's theses covering a broad range of INS/GPS integration topics [1-3, 8, 11, 19-21, 23-25, 27-30]. The integration of INS and GPS is normally accomplished using a Kalman Filter. In this case, the Kalman Filter estimates the drift errors in the INS position, velocity, and attitude measurements. The filter also estimates the errors in the GPS pseudorange measurements due to clock bias, clock drift, and atmospheric errors. With proper modeling, these errors can be estimated with very high accuracy. The more detailed the model, the more accurately the model represents the true, real world system. These complex models are called "*truth models*". However, there is a significant trade off between a complex Kalman Filter model and the computer hardware necessary to implement it. Therefore, most truth models are reduced in complexity and simulated with lower resolution models called "*filter models*". It is the Kalman Filter designer's job to develop a filter model that represents the truth model adequately, thus simulating the true, real world system.

1.1.5. Integration Methods

There are different system integration methods in navigation systems. Two methods typically implemented are "tight" and "loose" integration. The loose integration method is a filter-aided-filter technique [23]. In this case, each sensor in the navigation system uses its own Kalman filter to process its measurements. The processed measurements are then combined through another Kalman filter to obtain the final integrated position solution.

Tight navigation system integration combines unprocessed measurements from the sensors through a single Kalman filter. Figure 3 shows the difference between a tightly coupled sensor fusion system and a loosely coupled system. Tight integration provides the Kalman Filter with access to the raw measurement instead of pre-processed measurement information, provides the filter designer a means to develop the filter with one complete set of algorithms, and decreases the overall complexity of the system. Also, a tight integration scheme allows for continued operation when there are less than the four required satellite vehicles for GPS [9]. As previously mentioned, there are four unknown variables in GPS positioning. Therefore, without four available satellites the GPS position solution degrades quickly. In loosely integrated INS/GPS systems these poor position solutions are combined with drifting INS position solutions complicate the pilot's situational awareness. Tight integration of the INS and GPS in this case removes the GPS's own Kalman filter and outputs GPS pseudoranges straight into the navigation Kalman filter. Even though there are less than four satellites, the GPS receiver still processes the GPS space signals into pseudoranges which can be used by the navigation Kalman filter. The pseudoranges are then used as measurements to correct the INS drift errors.

1.2. Current Research

As previously stated, there has been a volume of work produced at AFIT regarding the benefits of INS/GPS integration. The work of Stacey and Negast produced a reduced order filter model simulation of an integrated INS and GPS [8, 24, 29]. Their work

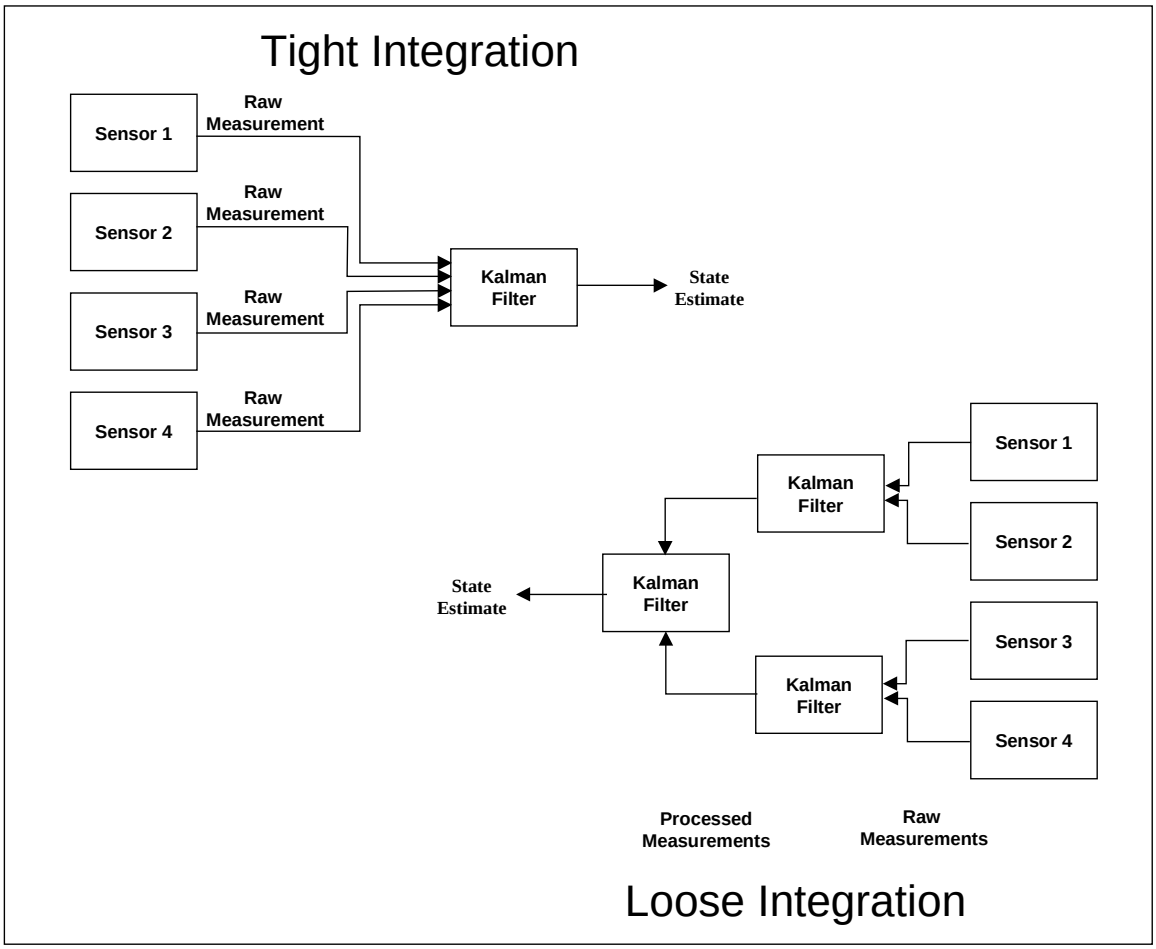

Figure 3. Tight vs. Loose Integration

reduced the 128-state integrated truth model down to a fully tuned 13-state filter model. Gray provided a performance analysis of this truth and filter model as it applies to aircraft precision landing [3]. Gray's work also added a barometric and radar altimeter model and a GPS pseudolite model to the existing simulation software. Britton then followed Gray's work by simulating the precision landing scenario with a differential GPS model [25]. Sokol implemented a filter-driving-filter simulation to test the performance of a loosely integrated INS/GPS [23].

Another set of AFIT students began simulating carrier-phase differential GPS (CPGPS) integration with the reduced order INS from Negast. Beginning with Hansen,

the initial CPGPS model was integrated into the Negast navigation reference system (NRS) [28]. Hansen also simulated the effects of cycle slips on CPGPS measurements. Mosle then investigated ways of implementing failure detection and recovery from CPGPS cycle slips using Chi-Squared techniques and likelihood ratios [30]. From this point, Bohenek finished up this line of research removing an unrealistic "perfect velocity" measurement from Mosle and Hansen's research [20].

1.3. Problem Definition

In order to perform targeting with SAR sensors, a high-resolution sensor is needed for targeting accuracy. Typically, it is very expensive to build high-resolution SAR reconnaissance sensors. It is even more expensive to modify existing sensors to achieve a higher resolution capability. Therefore, increasing SAR targeting accuracy without modifying the SAR sensor would prove very valuable. This thesis presents a method for increasing SAR targeting accuracy by modifying the navigation Kalman filter onboard a typical SAR airborne platform. With an integrated GPS/INS navigation system, the aircraft position, velocity, and attitude is known with very high accuracy. Aircraft position accuracy, combined with SAR range and range rate measurements can then be integrated in the navigation filter to provide a better estimate of the actual target position. Additionally, radar errors will be estimated in the existing navigation filter to help further refine the target position.

The work presented entails simulating the INS, GPS, and SAR onboard a U-2S Reconnaissance aircraft during a typical SAR targeting mission. There is an ongoing program in the U-2 Reconnaissance Mission Area Group to enhance the capability of the

SAR mission by providing GPS capability to the U-2 [26]. Therefore, this work will simulate the addition of GPS to the U-2's navigation system. A new flight profile was created to simulate a typical U-2 reconnaissance mission. Three GPS implementations will be simulated: stand-alone, differential positioning, and carrier-phase differential positioning. Results presented herein will define the potential SAR targeting performance increase specific to the type of GPS receiver used onboard the U-2. In addition, every attempt was made to obtain similar aircraft position and velocity results from previous research [3, 8, 25, 27-30].

1.4. Scope

There are many tasks associated with implementing this type of research:

a) Review major research work. Theses regarding different INS/GPS integration techniques, DGPS/CPGPS simulation, and radar simulation.

b) Determine flight dynamics characteristics of the U-2 to generate a proper flight profile for use in this research. Currently, the flight profile used in past theses was a KC-135 flight [1-3, 8, 11, 19-21, 23-25, 27-30].

c) Research SAR reconnaissance mission techniques. It is important to generate SAR measurements that are typical of a U-2 SAR missions to simulate the scenario properly

d) Remove all extraneous information and code from existing Fortran software. This includes: removal of "dead" states, i.e. transponder model states, unused subroutines, and references to unnecessary commands and routines. The end result of this step is to provide future Multimode Simulation of Optimal Filter Equation (MSOFE) users with

efficient well documented source code. Also, all previous code generated using UNIX-based Fortran 77 will be upgraded to PC-based Fortran 90.

e) Combine the new SAR model with existing integrated INS/GPS simulation software. This includes both the truth model and filter model. Also, if the truth model can be reduced, analyze the potential reduced order filter model.

f) Tune the filter model to reproduce the INS/GPS/SAR error characteristics as closely as possible. While this filter is not intended to be flight worthy, this step proves the validity of the filter model's ability to track the true errors of the integrated system.

g) Generate up to a 50 test Monte Carlo analysis of all integrated system designs.

h) Conduct a performance analysis of each integrated system: stand-alone, differential and carrier-phase differential GPS. Determine the aircraft position and velocity errors and their effects on SAR targeting errors.

i) Provide results in a manner that a decision analysis may be undertaken to determine which type of GPS would perform adequately with regards to U-2 GPS upgrade specifications. The cost-to-performance issue regarding GPS type is not presented in this thesis.

1.5. Assumptions

Typical of any simulation, assumptions were made in this thesis to facilitate the development, design, and analysis of the GPS/INS/SAR models.

a) The flight profile of the U-2 was a straight-and-level racetrack pattern, which is typical of U-2 mission standards.

b) Typical performance characteristics were used to define the accuracy of each GPS model used in this work. All GPS ephemeris data were provided through the Coast Guard from 21 May 1994 [3]. GPS measurements will be provided at 1-second intervals in accordance with previous research [1-3, 8, 11, 19-21, 23-25, 27-30].

c) The Barometric altimeter stabilizes the INS vertical channel.

d) SAR measurements will be provided as range and range rate from the aircraft to the target. Typically, a SAR is programmed, pre-mission, to image specific areas for spotlight mode operation. Therefore, it is assumed that the target position is known and the SAR sensor will be pointed at the target location with some amount of error in the range and range rate information.

e) The double-precision computer simulation using the Multi-mode Simulation for Optimal Filter Evaluation (MSOFE) provides accurate numerical precision for this simulation [6]. Real world results are provided through the full-order error-state truth model and adequately represent real world performance.

f) The truth data (flight information), generated through PROFGEN, a flight profile generation software package, properly represents a U-2 aircraft reconnaissance mission.

g) Plotted outputs generated using the commercial package MATLAB [31] as a result of 50 Monte Carlo simulations provide proper statistical analysis.

h) Taylor series approximations truncated to first order are used to linearize all nonlinear equations in the navigation system. Perturbations about a nominal trajectory create the error-state equations [3].

1.6. Literature Review

This section outlines the current areas of research and development regarding INS/GPS integration and SAR targeting.

1.6.1. Sensor Fusion

Sensor fusion has become an extremely important topic in the defense industry. The fusion of sensor data from multiple imagery systems can provide enhancements to stand alone systems for imagery analysts. Navigation sensor fusion, as previously mentioned, can enhance aircraft position and velocity accuracy by using multiple sensors that have varying complementary characteristics. For example, an INS has very good high frequency characteristics, but poor low frequency characteristics. GPS on the other hand has the opposite characteristics; GPS is subject to several high frequency error sources, including atmospheric and multipath noise. Thus, fusing the data from these two sensors in a single Kalman filter provides the user with extremely reliable and accurate position and velocity information.

Observability considerations are also important to sensor fusion techniques. In some applications, the parameter that needs to be measured and estimated may be related to several different sensors. In this case, the more sensors provided, the better the estimate of the necessary parameter. Another consideration is the fusion technique. Proven fusion methods, like the Kalman filter, must be used to provide the best possible estimate of the parameter. Some areas that could take advantage of sensor fusion techniques include remote sensing, air and surface target tracking, and imagery analysis.

Layne developed an INS/GPS/SAR model which he used to simulate the targeting performance of the SAR in relative and absolute targeting modes [11, 32]. Using both SAR and monopulse radar measurements, Layne proved that optimal integration of SAR measurements into an INS/GPS Kalman filter provides a aircraft and targeting positions within 10-*ft* circular error probability (CEP). However, in most SAR reconnaissance missions, including the U-2, a monopulse radar is not available.

1.6.2. Airborne Mapping

An emerging sensor fusion area in the civilian arena is airborne mapping. There are multitudes of papers regarding the importance of very accurate GPS/INS integration techniques in large scale mapping [14, 16, 17]. Producing high-resolution ground maps is important in both the civilian and military sectors. Work in this area includes reconnaissance sensor and navigation system integration as well as integration with multiple reconnaissance sensors on one airborne platform. There are also important considerations regarding the ability to process information both real time and post mission. Most work in this area to date involves post processing accurate aircraft position with the mapping imagery. Real time processing of mapping information with accurate aircraft location would be critical in a military battlefield scenario.

1.6.3. Multi- Sensor / Multi-Target Tracking

The Air Force Research Laboratory (AFRL), Sensors Directorate is currently researching multi-target, multi-sensor tracking in the theater battlefield [17, 33, 34]. This research takes into consideration the performance of each sensor aircraft (reconnaissance,

fighter, bomber, etc.) navigation system and sensor suite. Statistical information based on the navigation system and sensor suite is also included in the multi-target, multi-sensor scenario to determine the accuracy of each aircraft's ability to track a ground based target. Inherent in this study is the need to determine the best collection and *integration* of onboard sensors, to derive the best possible estimate of the target geolocation (location on the earth). Current research does not include tight integration of the reconnaissance sensors with the navigation sensors onboard each aircraft.

A critical area of multi-sensor systems includes differences in sensor resolution and measurement rates. In most cases, two different imagery sensors will have different resolutions and measurement rates. One technique currently being researched is wavelet data transformations [33, 34]. This technique gives a designer the capability to match measurement rates between sensors thus providing the ability to optimally fuse the information as it's provided by each sensor. Wavelet compression and decompression techniques are very accurate and are currently being studied in multi-sensor arenas [34].

1.7. Methodology Overview

The research presented here was started by studying the integrated GPS aided INS models developed from Bohenek [20], Negast [8], White [2], Gray [3], and Miller [1]. This also included a review of the Litton LN-93 Error Model [24]. A review of existing SAR models was performed to determine the relationships between SAR measurements and INS/GPS measurements and dynamics. Once the GPS/INS model was reviewed and duplicated, the SAR model was designed and implemented in the MSOFE simulation

software. MSOFE runs both a covariance analysis and Monte Carlo simulation of the integrated sensor models.

Three different cases were simulated using MSOFE: integrated INS/GPS/SAR using stand-alone GPS, differential GPS, and carrier-phase differential GPS implementations. The performance of these three cases were than compared to determine the theoretical SAR targeting performance based on each type of GPS receiver. All data generated by MSOFE was manipulated into data files by a second program called MPLOT. The data files produced from MPLOT were than passed to MATLAB for tuning analysis and thesis presentation.

1.8. Overview of Thesis

Chapter 2 presents the theory used to develop the INS, GPS, and SAR mathematical models. Kalman filter theory is defined and presented using Maybeck as a guide [4]. The mathematical relationships defining the characteristics of INS, GPS, and SAR are also presented in this chapter.

Chapter 3 describes the specific dynamics and measurement models for the INS, GPS, barometric and radar altimeters, and SAR. The error models presented here are based on the Litton LN-93 error models for a typical INS. The filter model and truth model for each sensor is presented as well as the final integrated Kalman filter model.

Chapter 4 presents the results of each case simulated in this study. Analysis of the targeting performance based on each GPS receiver type is the focus of this chapter.

Chapter 5 summarizes the research effort and provides recommendation for future enhancements and research areas as an extension to this work.

1.9. Summary

This chapter provided an overview of the plan of attack for determining the characteristic performance of an integrated INS/GPS/SAR navigation Kalman filter. Previous research into this subject was presented as well as current research into the fields of multi-sensor fusion and navigation system analysis. Chapter 2 will further develop the theory behind Kalman filter development and navigation reference frames.

2. Theory

2.1. Overview

This chapter provides a development of the extended Kalman filter (EKF) used to integrate the INS, GPS, and SAR sensors mentioned in Chapter 1. An EKF used is often used when integrating nonlinear, time-varying dynamic systems. A detailed discussion on the specific characteristics of each sensor is also presented in this chapter, with several figures graphically describing the sensor suites and their performance characteristics.

2.2. Extended Kalman Filter

The Kalman filter is an optimal recursive data processing algorithm [4,5]. The filter is optimal meaning all information available to the filter is processed and incorporated. The filter is recursive in that the filter does not require all of the previous data to be kept in storage and reprocessed every time a new measurement is available. The Kalman filter processes all available measurements of the variable of interest, regardless of their accuracy, based on knowledge of the system and measurement dynamics, the statistical description of the system noises, measurement errors, and model uncertainties [4]. In some cases, the models may be linear, but most system models are nonlinear in nature. For nonlinear system models, an extended Kalman filter (EKF) is implemented. The EKF linearizes the nonlinear system model allowing the designer to utilize the linear assumptions and equations in the following sections. During operation, an EKF is relinearized based on the most current optimal estimate of the variable of interest. In this way, the variable estimate is not subjected to a fixed nominal trajectory.

2.2.1. State and Measurement Model Equations

Following the Kalman filter development in [2-5, 6-10, 19-21, 23], let a system model be defined as a state equation in the form shown in Equation (1),

$$\dot{\mathbf{x}}(t) = \mathbf{f}[\mathbf{x}(t), t] + \mathbf{G}(t)\mathbf{w}(t) \tag{1}$$

where the state dynamics vector $\mathbf{f}[\mathbf{x}(t), t]$ could be a linear or nonlinear function of the state vector $\mathbf{x}(t)$ and time t. The matrix $\mathbf{G}(t)$ is a noise distribution matrix assumed to be identity for this system. The vector $\mathbf{w}(t)$ is considered a white Gaussian noise with a mean value and strength shown in Equations (2) and (3) respectively.

$$E[\mathbf{w}(t)] = 0 \tag{2}$$

$$E[\mathbf{w}(t)\mathbf{w}^T(t+\tau)] = \mathbf{Q}(t)\delta(\tau) \tag{3}$$

Let the discrete time measurements, $\mathbf{z}(t_i)$, be modeled as a function (linear or nonlinear) of the state vector and time, $\mathbf{h}[\mathbf{x}(t_i), t_i]$, and additive white noise:

$$\mathbf{z}(t_i) = \mathbf{h}[\mathbf{x}(t_i), t_i] + \mathbf{v}(t_i) \tag{4}$$

The discrete time measurement noise vector, $\mathbf{v}(t_i)$, is another zero-mean white noise process, assume independent of $\mathbf{w}(t)$, and having covariance $\mathbf{R}(t_i)$ defined by:

$$E[\mathbf{v}(t_i)\mathbf{v}^T(t_i)] = \begin{cases} \mathbf{R}(t_i) & for\ \ t_i = t_j \\ 0 & for\ \ t_i \neq t_j \end{cases} \tag{5}$$

2.2.2. State and Measurement Model Linearization

As previously mentioned, Equations (1) and (4) can be nonlinear. Assuming they are nonlinear, the EKF filter equations must be linearized to produce a first order estimate of the state vector $\mathbf{x}(t)$. The linearization technique used in [2-5, 6-10, 19-21, 23-25, 27-30]

involves perturbations about a nominal state trajectory. The perturbation technique that follows will produce a linearization of Equations (1) and (4) for use in an EKF.

Assume a nominal state trajectory, $\mathbf{x}_n(t)$, exists satisfying the initial condition $\mathbf{x}_n(t_0) = \mathbf{x}_{n_0}$ and the noise-free dynamics equation

$$\dot{\mathbf{x}}_n(t) = \mathbf{f}[\mathbf{x}_n(t), t] \tag{7}$$

using the same $\mathbf{f}[\cdot,\cdot]$ as in Equation (1). The nominal measurements, noise-free, are also based on the nominal state trajectory defined by

$$\mathbf{z}(t_i) = \mathbf{h}[\mathbf{x}(t_i), t_i] + \mathbf{v}(t_i) \tag{8}$$

using the same $\mathbf{h}[\cdot,\cdot]$ as given in Equation (4).

To perturb the state from its assumed nominal trajectory, Equation (1) is subtracted from Equation (7) producing the perturbation state $\delta\mathbf{x}(t)$:

$$\delta\dot{\mathbf{x}}(t) \equiv [\dot{\mathbf{x}}(t) - \dot{\mathbf{x}}_n(t)] = \mathbf{f}[\mathbf{x}(t), t] - \mathbf{f}[\mathbf{x}_n(t), t] + \mathbf{G}(t)\mathbf{w}(t) \tag{9}$$

A Taylor series expansion about $\mathbf{x}_n(t)$ on $\mathbf{f}[\mathbf{x}(t), t]$ produces Equation (10):

$$\mathbf{f}[\mathbf{x}(t), t] = \mathbf{f}[\mathbf{x}_n(t), t] + \left.\frac{\partial \mathbf{f}[\mathbf{x}(t), t]}{\partial \mathbf{x}}\right|_{\mathbf{x}=\mathbf{x}_n(t)} [\mathbf{x}(t) - \mathbf{x}_n(t)] + h.o.t. \tag{10}$$

where *h.o.t.* is defined as the higher order terms of $\partial\mathbf{x}(t)$ with powers greater than one. Substituting a first order approximation of Equation (10) into Equation (9) forms the perturbation state equation:

$$\delta\dot{\mathbf{x}}(t) = \mathbf{F}[t; \mathbf{x}_n(t)]\delta\mathbf{x}(t) + \mathbf{G}(t)\mathbf{w}(t) \tag{11}$$

where the matrix $\mathbf{F}[t; \mathbf{x}_n(t)]$ is defined by the first order partial fraction term shown in Equation (10): $\left.\frac{\partial \mathbf{f}[\mathbf{x}(t), t]}{\partial \mathbf{x}}\right|_{\mathbf{x}=\mathbf{x}_n(t)} \delta\mathbf{x}(t)$. Equation (11) thus becomes the linearized dynamics equation used in the EKF.

This same procedure is performed for the discrete time measurement equations; subtracting Equations (4) and (8) produces the perturbation measurement $\delta\mathbf{z}(t_i)$:

$$\delta\mathbf{z}(t_i) \equiv [\mathbf{z}(t_i) - \mathbf{z}_n(t_i)] = \mathbf{h}[\mathbf{x}(t_i), t_i] - \mathbf{h}[\mathbf{x}_n(t_i), t_i] + \mathbf{v}(t_i) \tag{12}$$

Another Taylor series expansion is performed, this time about $\mathbf{z}_n(t_i)$ on $\mathbf{h}[\mathbf{x}(t_i), t_i]$, producing the linearized perturbed discrete time measurement equation used in the EKF:

$$\delta\mathbf{z}(t_i) = \mathbf{H}[t_i, \mathbf{x}_n(t_i)] + \mathbf{v}(t_i) \tag{13}$$

where $\mathbf{H}[t_i, \mathbf{x}_n(t_i)]$ is defined by:

$$\mathbf{H}[t_i, \mathbf{x}_n(t_i)] = \left.\frac{\partial\mathbf{h}[\mathbf{x}(t_i), t_i]}{\partial\mathbf{x}}\right|_{\mathbf{x}=\mathbf{x}_n(t_i)} \tag{14}$$

It is important to remember that the EKF is only a first order approximation due to the truncated Taylor Series represented above. However, the nonlinear dynamics and measurement models have now been linearized to produce perturbation or "error" state equations. This is important because now the filter designer can implement a linear Kalman filter to perform all state propagation and update equations.

2.2.3. Extended Kalman Filter Equations

This section addresses the EKF equations implemented in this research effort. Using Equation (11) as the error dynamics model and Equation (13) as the discrete time measurement error model, the EKF will produce the optimal estimate of the state error vector $\delta\mathbf{x}(t)$, represented as $\delta\hat{\mathbf{x}}(t)$. Using the error state estimate, the whole state estimate can be calculated using:

$$\hat{\mathbf{x}}(t) = \mathbf{x}_\mathbf{n}(t) + \delta\hat{\mathbf{x}}(t) \tag{15}$$

Normally, if the true state trajectory differs from the nominal state trajectory, large errors could occur. The EKF reduces this effect by relinearizing about the most recent state estimate as shown in Equation (15), as opposed to just the nominal state value (like the linearized Kalman filter). Using the most recent state estimate takes away the need for a nominal trajectory as long as the error model is accurate. Therefore, using the EKF method allows the designer to declare a new nominal trajectory at every estimate thus ensuring deviations from the nominal trajectory remains small.

As previously mentioned, a Kalman filter is a recursive algorithm. There are two steps involved in this recursion: propagation and update. The state estimate, $\hat{\mathbf{x}}(t)$, and the covariance of that estimate, $\mathbf{P}(t)$, are both propagated from the last time sample , t_{i-1}, and updated at every time, t_i. Sampled data EKF equations utilize the following notations:

$t|t_i$ -- value of a given variable at time t, conditioned on the measurements taken through time t_i.

t_i^- -- value of a variable after propagation from t_{i-1} but prior to measurement update.

t_i^+ -- value of a variable after propagation from t_{i-1} and measurement update.

The subscript i is used to describe the discrete time points when measurements are available. Using these time notations, the state estimates $\hat{\mathbf{x}}(t|t_i)$ and covariance values $\mathbf{P}(t|t_i)$ are propagated from t_i to t_{i+1} using the following differential equations:

$$\dot{\hat{\mathbf{x}}}(t|t_i) = \mathbf{f}[\hat{\mathbf{x}}(t|t_i), t] \tag{16}$$

$$\dot{\mathbf{P}}(t|t_i) = \mathbf{F}[t; \hat{\mathbf{x}}(t|t_i)]\mathbf{P}(t|t_i) + \mathbf{P}(t|t_i)\mathbf{F}^T[t; \hat{\mathbf{x}}(t|t_i)] + \mathbf{G}(t)\mathbf{Q}(t)\mathbf{G}^T(t) \tag{17}$$

where:

$$\mathbf{F}[t;\hat{\mathbf{x}}(t|t_i)] = \left.\frac{\partial \mathbf{f}[\mathbf{x}(t),t]}{\partial \mathbf{x}}\right|_{\mathbf{x}=\hat{\mathbf{x}}(t|t_i)} \tag{18}$$

and the differential equation initial conditions are given by:

$$\hat{\mathbf{x}}(t_i|t_i) = \hat{\mathbf{x}}(t_i^+) \tag{19}$$

$$\mathbf{P}(t_i|t_i) = \mathbf{P}(t_i^+) \tag{20}$$

When discrete time measurements, $\mathbf{z}_i$, become available, the EKF update cycle is performed using the following equations:

$$\mathbf{K}(t_i) = \mathbf{P}(t_i^-)\mathbf{H}^T[t_i;\hat{\mathbf{x}}(t_i^-)]\{\mathbf{H}[t_i;\hat{\mathbf{x}}(t_i^-)]\mathbf{P}(t_i^-)\mathbf{H}^T[t_i;\hat{\mathbf{x}}(t_i^-)] + \mathbf{R}(t_i)\}^{-1} \tag{21}$$

$$\hat{\mathbf{x}}(t_i^+) = \hat{\mathbf{x}}(t_i^-) + \mathbf{K}(t_i)\{\mathbf{z}_i - \mathbf{h}[\hat{\mathbf{x}}(t_i^-),t_i]\} \tag{22}$$

$$\mathbf{P}(t_i^+) = \mathbf{P}(t_i^-) - \mathbf{K}(t_i)\mathbf{H}[t_i;\hat{\mathbf{x}}(t_i^-)]\mathbf{P}(t_i^-) \tag{23}$$

$$\mathbf{P}(t_i^-) = \mathbf{P}(t|t_{i-1}) \text{ and } \hat{\mathbf{x}}(t_i^-) = \hat{\mathbf{x}}(t|t_{i-1}) \tag{24}$$

Notice that $\hat{\mathbf{x}}(t_i^+)$ and $\mathbf{P}(t_i^+)$ from Equations (22) and (23) are used to start the next t_{i+1} propagation/update cycle; $\hat{\mathbf{x}}(t_i^+)$ is also used for the calculation of Equation (18) rather than the nominal value $\mathbf{x_n}(t)$.

These equations are implemented in the MSOFE filter evaluation package [6]. Numerical techniques are used to perform all integration and derivative options as described in [6]. Also, the U-D factorization method is used in MSOFE to reduce computation loads and increase numerical stability [5]. The reader is referred to [4, 5] for a complete derivation of each equation and topic presented in Section 2.2.

2.2.4. Truth Model

A truth model is defined as a true model of the variables of interest. The truth model is a result of extensive analysis of the system of interest and its associated error

characteristics thereof. Through this extensive analysis, an extremely accurate representation of the system can be obtained. There still exists some small amount of error in the model since nature itself cannot be modeled perfectly. However, a truth model should provide the highest fidelity model to represent the "real world". The truth model for a typical dynamics/measurement system can be extremely vast. A good truth model could have over 100-states and 3rd or 4th order accuracy. For example, the Litton LN-93 Strapdown INS contains 93-states in its truth model. In addition, a GPS truth model can have up to 30-states. The benefits of a truth model are clear: in a simulation the truth model will define the true, "real world" dynamics and measurements of a system. However, due to online computing restrictions, these large state models become computationally burdensome. Therefore, in most cases a reduced order Kalman filter model is used which "adequately" tracks the performance of the truth model.

2.2.5. Filter Model

When designing a Kalman filter for error state estimation, its important to keep the number of states to a manageable level. However, the best model to use would be the system truth model. Therefore, the filter designer must make a tradeoff between the number of states in the filter and the accuracy of the filter. Another consideration is the amount of computer resources available. Typically, the filter designer must tailor his filter to operate under limited processing speed and memory allocation. A high-order filter design has the potential of taking too much processing time during the Kalman filter update cycle. For example, if the computer is still calculating during the propagation cycle, the measurement update may be delayed, thus losing the information gained by the

measurements. While this concern is being alleviated by state-of-the-art digital computers, there is still a limit to the amount of states the filter model can use compared to the truth model. Generally, the computing power of the simulation tool or hardware implementation will determine how many states can be included in the Kalman filter design.

The end result of the online Kalman filter design is a filter model that accurately tracks the system truth model but has a smaller, more manageable number of states. Two steps are important in designing a proper filter model: state order reduction and filter tuning. If done properly, these two steps should produce a filter model which adequately represents the system in the "real world" and can be implemented within the limited computer resources available to the designer.

2.2.5.1. Order Reduction

The first step in filter model design process is truth model order reduction. This step involves analyzing the less dominant states of the truth model and either absorbing them into existing states or eliminating them altogether. Starting with the truth model, a thorough engineer will begin deleting states that he/she deems unnecessary for the final, online filter implementation. Then, through trial and error, other states may be eliminated or rolled into existing states to further diminish the number of states left in the filter. One important facet of order reduction is to first determine which states must not be removed. For navigation filters, the position, velocity, and attitude error states are the most important states and cannot be removed. However, there has been a significant amount of research performed [4, 8] in the reduction of error states from an INS truth

model. Negast [8] showed that the LN-93 Strapdown INS truth model with 93-states could be reduced down to 10-states (with Barometric Altimeter included) and still maintain similar, but degraded performance compared to the full-order truth model. Any further reduction of states causes the filter's performance to diverge from the truth model.

As expected, the removal of states in any truth model must be accounted for in some matter. If the removal of the state does not affect the truth model in any way, it probably should not have been included in the first place. So, the filter designer must compensate for truth model state reduction using a technique called filter "tuning" [4].

2.2.5.2. Filter Tuning

Filter tuning compensates for the elimination and absorption of states in the truth model. As previously mentioned, the filter designer desires the performance of a truth model using a reduced order model in the online filter. However, without adequate tuning, filter model performance may suffer compared to that of the truth model. Therefore, the filter designer must modify the various noise strengths associated with the filter model to account for the missing states from the truth model.

Tuning a filter model involves adjusting the **Q** and **R** matrices of the filter model. The **Q**-matrix represents the dynamics driving noise and the **R**-matrix represents the measurement noise (as explained in Section 2.2). Using a filter analysis tool, such as MSOFE, allows the filter designer to tune the filter model to the truth model through trial and error. Since states are being removed from the truth model, they are accounted for in the reduced order filter model by increasing the noise values.

Increasing the dynamics noise strengths in the **Q**-matrix during tuning is important for several reasons [2, 4, 5, 8, 20]. First, because an EKF is used, the nonlinear aspects of the dynamics equations are only accurate to first order. Adding noise to linearized states helps the filter designer account for any loss of behavior caused by linearization. Another benefit of adding noise to the tuned states is to keep their associated Kalman filter gains from going to zero. As shown in Equation (22), as a state's Kalman filter gain approaches zero, the incoming measurement will be ignored and new information will not be provided to the Kalman filter. Adding dynamics driving noise ensures that the filter gain remains non-zero and new measurement information will be incorporated by the Kalman filter.

Another benefit of **Q**-matrix tuning occurs when the eigenvalues of the filter covariance matrix, **P**, become negative. Numerical precision problems can causes this phenomenon to occur in some filters [4]. Increasing the noise in a state with a potential negative covariance can ensure that the state stays positive.

There are also tuning benefits achieved by adjusting the **R**-matrix in reduced order filter models [2, 4, 5, 8, 20]. Like in the dynamics equations, the EKF also contains linearized measurement models. Increasing the measurement noise of linearized measurement equations can help reduce the impact of the loss of higher order terms. Also, when states are removed from the truth model, the filter measurement models may be affected. Adjusting the **R**-matrix noise strengths can help account for the missing states as in the dynamics model.

2.3. System Integration

As mentioned in Section 1.1.5, there are several different techniques used to integrate different sensor suites. Figure 3 shows two such techniques used at AFIT, tight and loose integration. Tight integration is defined as the integration of multiple sensors through manipulation of unprocessed measurements. A single Kalman filter is often used during tight integration to process the dynamics and measurements of the sensors. Other filter types could be used, but the Kalman filter is the best choice for combining all information from the sensor suite optimally [4, 5].

Loose integration involves integrating pre-processed sensor information; this data can also be manipulated using a Kalman filter. In cases where existing sensors are to be integrated (e.g. an aircraft already has an INS or SAR and a GPS is to be integrated), loose integration techniques may be the only technique available. These cases tend to have more mathematical complexity due to the addition of Kalman filters (or other filters) for each sensor suite. In addition, because the data processed in the final integration filter has been pre-processed, information may be lost and data correlation could be prevalent (refer to the GPS degradation with less than four available satellites example from Section 1.1.5).

There has been a vast array of work in the area of tight verse loose integration methods for integrating INS and GPS sensors [9, 23, 34]. Tight integration of an INS/GPS system involves processing the raw measurement data provided by the GPS receiver. Loose integration processes position and velocity information from the GPS's filter to an integrated navigation filter. Sokol showed there are inherent instabilities in a loosely integrated INS/GPS system under highly dynamic situations [23]. Lewantowicz

also showed that a loosely integrated GPS/INS system doesn't handle GPS information very well when situations are sub-optimal [9]. As can be seen in Figure 4, a loosely coupled GPS/INS system manipulates fully calculated GPS positions and velocities. When the GPS receiver does not have access to at least 4 SVs, the position and velocity calculations may become unstable. The second Kalman filter will still process these poor measurements which may lead to large errors [9]. However, a tightly integrated system, shown in Figure 5, processes the raw pseudorange measurements directly. Since pseudoranges are raw ranges between receiver and satellite, poor position solutions produced by the GPS receiver are not processed by the navigation filter. It is important to note that while loose integration has the potential for large errors in an integrated INS/GPS case, proper modeling can reduce this potential. In the Sokol case, a very poor INS model was the main culprit in leading to most of the errors [23]. Section 3.5 will describe the tight integration of a GPS and INS in much greater detail.

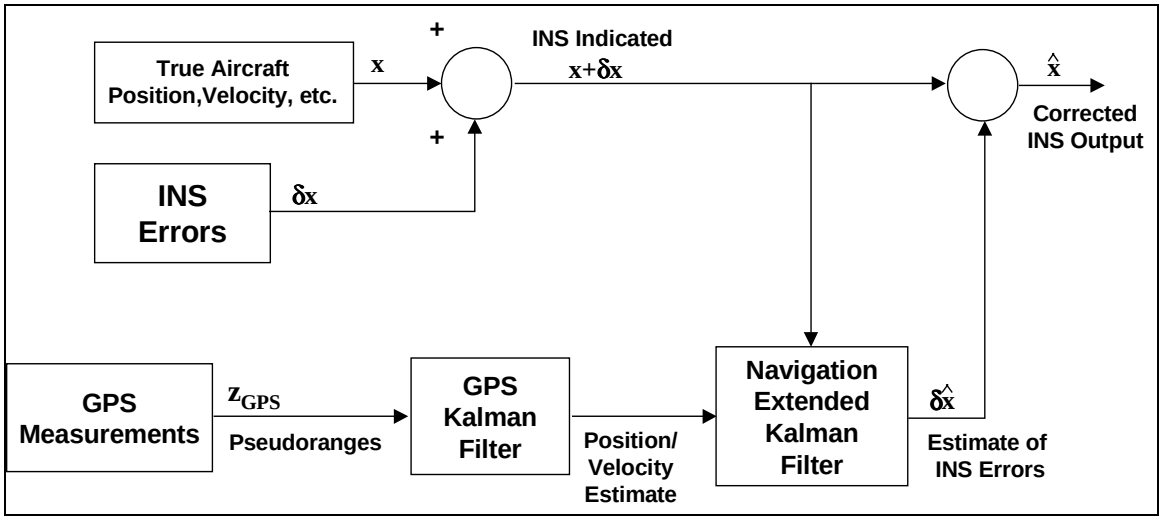

Figure 4. Loose INS/GPS Integration

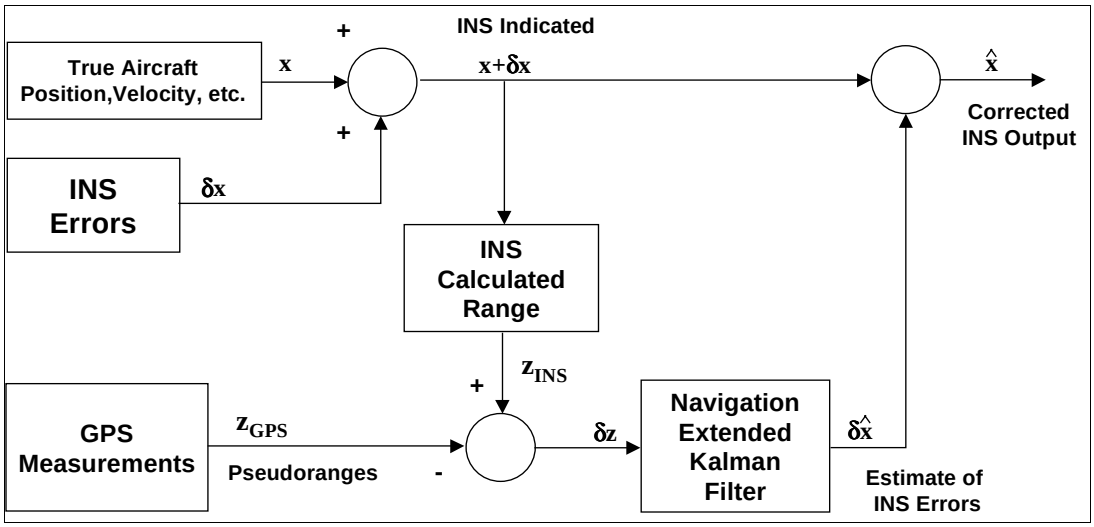

Figure 5. Tight INS/GPS Integration

2.4. Coordinate Frame Transformations

There are many array of methods for representing position and velocity of an aircraft with respect to the earth. The Litton LN-93 documentation, for example, defines up to eight different reference frames to represent the INS error model [24]! It is extremely important as a system designer and modeler to be knowledgeable about coordinate reference frames and the transformations between them. One technique for representing coordinate frame transformation is the direction cosine matrix (DCM). The DCM is a computationally efficient method of transforming and rotating one reference frame to another based on a three-dimensional position. In general, a three-dimensional position is defined in reference frame "A", $\mathbf{r}^{A}$. It is desired that the position be defined in another reference frame, "B", $\mathbf{r}^{B}$. To rotate all three A-referenced positions to B-referenced positions, the following equation can be used:

$$\mathbf{r}^{B} = \mathbf{C}_{A}^{B}\mathbf{r}^{A} \tag{26}$$

where $\mathbf{C}_A^B$ is the DCM transformation matrix between reference frame "A" and reference frame "B". A typical reference frame for navigation applications is the earth-centered-earth-fixed (ECEF) frame. This frame will be the base frame for representing the terrestrial navigation simulated in this thesis. Following the techniques of Britting [18] and Bagley [21], three coordinate transformation DCMs are developed: inertial-to-ECEF, ECEF-to-Navigation, and ECEF-to-Wander Azimuth.

2.4.1. Inertial to ECEF

The inertial reference frame is defined as an orthogonal reference frame with its origin at the center of the earth and three axis as follows: *x*- and *y*- axis in the earth's equatorial plane and *z*-axis coincident with the earth's spin axis angular velocity [18]. Figure 6 shows the inertial reference frame with axis x^i, y^i, and z^i. The ECEF reference frame is also represented in Figure 6.

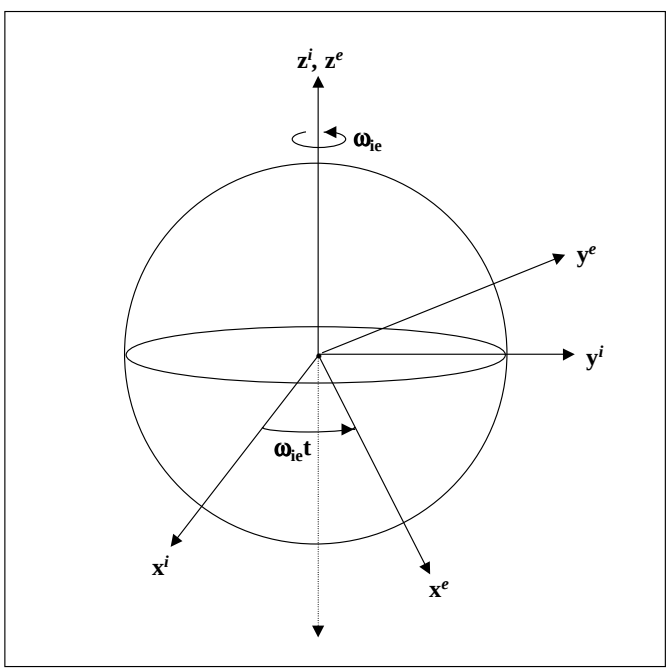

Figure 6. Inertial/ECEF Reference Frame Geometry

The ECEF frame has the same axes as the inertial frame, but it rotates with the earth after a specific time, $t=0$, by the earth's rotational velocity, $\boldsymbol{\omega}_{ie}$, about the z-axis. Therefore, the relationship DCM between the inertial and ECEF frames is shown in Equation (27).

$$\mathbf{C}_e^i = \begin{bmatrix} \cos\omega_{ie}t & -\sin\omega_{ie}t & 0 \\ \sin\omega_{ie}t & \cos\omega_{ie}t & 0 \\ 0 & 0 & 1 \end{bmatrix} \tag{27}$$

For example, the x-dimension position in inertial space, in terms of ECEF coordinates would be:

$$\mathrm{x}^i = \cos\omega_{ie}t(\mathrm{x}^e) - \sin\omega_{ie}t(\mathrm{y}^e) \tag{28}$$

To transform back to ECEF from inertial coordinates, the matrix transpose of Equation (27) would be used. This is only true for transformations that utilize orthonormal reference frames [18].

2.4.2. ECEF to Navigation

For airborne navigation purposes, it is generally useless for pilots to know their position relative to the earth's center. Therefore, the navigation frame is used to define a position with respect to the earth's surface (latitude, longitude, and altitude). Figure 7 describes the physical interpretation of the Navigation frame with respect to the earth. The navigation frame is defined as an orthogonal, right-handed coordinate system; its origin is at the location of the INS and its axes are aligned with North, East, and Down directions [21].

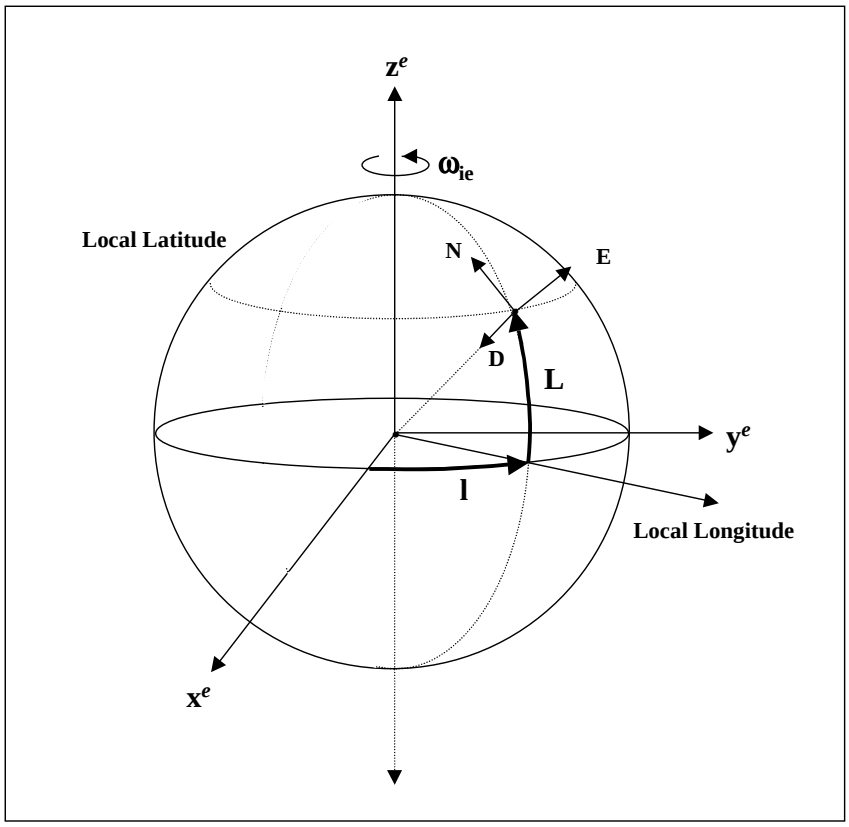

Figure 7. ECEF/Navigation Frame Geometry

2.4.3. Wander Azimuth Reference Frame

The Litton LN-93 error model [24] uses a wander azimuth reference frame. The wander azimuth frame is a variation of the navigation frame presented in the last section. The wander azimuth frame, represented by an *a* superscript, coincides with the platform frame when the wander angle, α, equals 0°. The wander angle is a computed angle between a wander azimuth platform and north [21]. The purpose of the wander azimuth coordinate frame is to provide a proper INS navigation solution during flight over the polar regions of earth. These regions cause problems in a platform INS due to the 180° shifts in geographic latitude.

The DCM to transform from the wander azimuth frame to the navigation frame is

$$\mathbf{C}_a^n = \begin{bmatrix} \cos\alpha & -\sin\alpha & 0 \\ \sin\alpha & \cos\alpha & 0 \\ 0 & 0 & 1 \end{bmatrix} \tag{29}$$

where α is the wander angle. The DCM to transform from the wander azimuth frame to the ECEF frame is

$$\mathbf{C}_a^e = \begin{bmatrix} \cos l\cos\alpha - \sin L\sin l\sin\alpha & -(\cos l\sin\alpha + \sin L\sin l\cos\alpha) & \sin l\cos L \\ \cos L\sin\alpha & \cos L\cos\alpha & \sin L \\ -(\sin l\cos\alpha + \cos l\sin L\sin\alpha) & \sin l\sin\alpha - \cos l\sin L\cos\alpha & \cos l\cos L \end{bmatrix} \tag{30}$$

2.4.4. Other Reference Frames

In addition to the four reference frames presented in the previous sections, there are two more frames specifically applicable to this thesis research, the body frame and error-angle frame [21, 24]. The body frame, represented by a *b* superscript, is an orthogonal, right hand frame that describes an aircraft's attitude in terms of roll, pitch, and yaw. Britting shows some excellent pictorial representations of this frame in terms of aircraft attitudes [18]. Assuming the origin of the body frame coincides with the origin of the navigation frame, the following DCM describes the transformation from wander azimuth to body frame:

$$\mathbf{C}_a^b = \begin{bmatrix} \cos P\sin Y & \cos P\cos Y & \sin P \\ \sin R\sin P\sin Y + \cos R\cos Y & \sin R\sin P\cos Y - \cos R\sin Y & \sin R\cos P \\ \cos R\sin P\sin Y - \sin R\cos Y & \cos R\sin P\cos Y + \sin R\cos Y & -\cos R\cos P \end{bmatrix} \tag{31}$$

where *R* is aircraft roll, *P* is aircraft pitch, and *Y* is aircraft yaw.

The error angle frame, represented by an *ea* superscript, is defined in [24] as the difference between the wander azimuth frame and another frame designated the "computer" frame. The computer frame is a Litton frame used to define the INS

indicated position. Thus, the computer frame is subject to INS related drift errors and does not equal the "true" wander azimuth frame defined above. The error angle frame has the following parameters:

$$\begin{bmatrix} \delta\theta_x \\ \delta\theta_y \\ \delta\theta_z \\ \delta h \end{bmatrix} \begin{array}{l} x\text{ - dimension angle between wander azimuth and computer frame} \\ y\text{ - dimension angle between wander azimuth and computer frame} \\ z\text{ - dimension angle between wander azimuth and computer frame} \\ \text{error in altitude above referenced ellipsoid} \end{array}$$

For the error state representations as defined in Section 2.2, another set of reference variables are used. This set, defined as the navigation error space is represented as follows:

$$\begin{bmatrix} \delta L \\ \delta l \\ \delta\alpha \\ \delta h \end{bmatrix} \begin{array}{l} \text{latitude error} \\ \text{longitude error} \\ \text{wander azimuth angle error} \\ \text{error in altitude above referenced ellipsoid} \end{array}$$

The DCM used to transform from error angle coordinates to the navigation error space, represented by an *ne* superscript, is

$$\mathbf{C}_{ea}^{ne} = \begin{bmatrix} -\cos\alpha & \sin\alpha & 0 & 0 \\ \sin\alpha\sec L & \cos\alpha\sec L & 0 & 0 \\ \sin\alpha\tan L & -\cos\alpha\tan L & 1 & 0 \\ 0 & 0 & 0 & 1 \end{bmatrix} \tag{32}$$

2.4.5. Reference Frame Perturbation

When a transformation is computed between two orthogonal reference frame, if there are errors present in the variables within the DCM, the DCM itself could be subject to errors. These errors in DCM transformations can be analytically represented by a DCM

perturbation equation such as the errors in transforming body coordinates to the navigation frame:

$$\overline{\mathbf{C}}_b^n = \mathbf{C}_b^n + \delta\mathbf{C}_b^n \tag{33}$$

where the indicated DCM, $\overline{\mathbf{C}}_b^n$, is the sum of the true DCM and a small error (using small angle assumptions [18]). The DCM error term, $\delta\mathbf{C}_b^n$, is a function of the aircraft body attitude errors (roll, pitch, and yaw errors) and is generally nonorthogonal. Britting highlights the importance of working with orthogonal reference frames due to the following characteristic:

$$\mathbf{C}_b^n(\mathbf{C}_b^n)^T = \mathbf{I} \tag{34}$$

meaning the transformation from body to navigation frame is equal to the transpose of the transformation from navigation to body frame [18]. Since the DCM perturbation technique could produce nonorthogonal matrices, the following orthogonalization equation may be used to orthogonalize the $\overline{\mathbf{C}}_b^n$ term [11, 18]:

$$(\overline{\mathbf{C}}_b^n)_o = \{\mathbf{I} + \tfrac{1}{2}[\delta\mathbf{C}_b^n\mathbf{C}_n^b - \mathbf{C}_b^n(\delta\mathbf{C}_b^n)^T]\}\mathbf{C}_b^n \tag{35}$$

Britting also shows that the bracketed term in Equation (35) is a skew symmetric matrix since it involves the difference between a matrix and its transpose. Therefore, Equation (35) can be written

$$(\overline{\mathbf{C}}_b^n)_o = (\mathbf{I} - \boldsymbol{\Psi})\mathbf{C}_b^n \tag{36}$$

where $\boldsymbol{\psi}$ is a skew-symmetric matrix of aircraft attitude angles (including the attitude errors to be estimated by the Kalman filter):

$$\boldsymbol{\Psi} = \begin{bmatrix} 0 & -\Psi_z & \Psi_y \\ \Psi_z & 0 & -\Psi_x \\ -\Psi_y & \Psi_x & 0 \end{bmatrix} \tag{37}$$

2.5. Summary

This chapter has presented the basic theory behind Kalman filtering techniques and coordinate reference frame transformations. Linearization and perturbation techniques were also described. These topics were used extensively throughout the simulation software. Chapter 3 will describe in detail the modeling and simulation software, the INS, GPS, and SAR models, and the integration technique used to combine the INS, GPS, and SAR into a single Kalman filter.

3. Modeling Methodology

3.1. Overview

This chapter provides a complete description of the system models, integration methods, and simulation techniques used in this research effort. An overall system description is presented followed by a detailed description of each sensor model. The truth and filter models for each sensor is developed and the final augmented dynamics and measurement model is defined. Finally, the simulation methodology will be presented along with a description of each software package used to perform this research. Following the description of the system and simulation techniques, Chapter 4 will discuss the completed results based on the aforementioned goals.

3.2. Overall System Description

Figure 8 describes a top level view of the system integration technique used in this research. A USAF U-2 Reconnaissance aircraft is presented as the airborne platform in which the sensor integration is to be performed. The U-2 supports all three sensor suites: the GPS, INS and SAR reconnaissance sensor. The GPS and INS is tightly integrated in accordance with Section 2.3 and Figure 5, where the raw pseudorange information is available to the centralized navigation Kalman filter. The GPS measurements are used to update the Kalman filter's estimate of INS position, velocity, and attitude errors. These errors are then subtracted from the indicated position, velocity, and attitude provided from the INS forming an optimal estimate of the true aircraft position, velocity, and

attitude. The simulation and modeling of a tightly integrated INS/GPS has been proven extensively through the works of [1-4, 8, 9, 21-24].

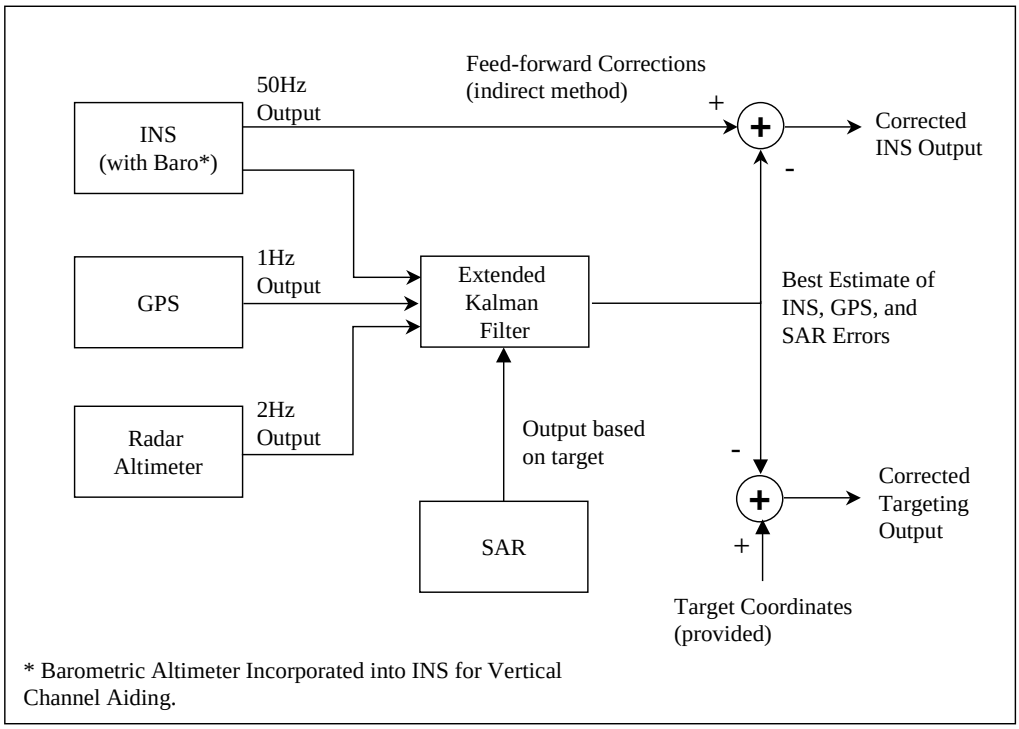

Figure 8. GPS/INS/SAR Integrated Block Diagram

This research effort focuses on the addition of the SAR model to the existing INS/GPS tight integration. The following model development will allow for the addition of SAR range and range rate measurements into the existing navigation Kalman filter. The navigation filter will be augmented by several new error states including SAR errors and SAR targeting errors. The coupling of INS/GPS aircraft position errors and SAR targeting errors into a single Kalman filter will reduce the overall complexity of the system integration and take advantage of the tight integration benefits described in Section 2.3. It is expected from this research, that a highly accurate aircraft position and velocity estimate will produce better targeting accuracy without improving the

performance of the SAR sensor. The dynamics and measurement equations to be used in this integration will follow in subsequent paragraphs.

The simulation will be typical of a U-2 SAR reconnaissance mission. During the U-2 mission, the SAR collection deck is produced prior to aircraft launch. A collection deck provides the order of reconnaissance imagery collection performed during a U-2 SAR mission. The sensor is programmed to take images in both search and spotlight modes throughout the mission at pre-specified locations based on aircraft position. When the U-2 arrives at the proper location, the sensor will image the area in accordance with its collection plan. For simulation purposes, several target areas will be provided along the flight trajectory simulation file. Therefore, the simulation software, MSOFE, will be programmed to receive SAR measurements, when they become available, as specified prior to running the simulation. The INS/GPS position and velocity estimates are provided at an extremely high rate with respect to the SAR measurements. This will provide the highly accurate aircraft position and velocity estimate needed for reducing the SAR targeting error.

To simulate the effect a highly accurate aircraft position estimate has on SAR targeting errors, three different GPS implementations will be simulated: single, differential, and carrier phase. Each receiver provides measurements to the navigation filter which in turn provides an estimate of the aircraft position, velocity, and attitude as well as SAR targeting error. It is expected that a highly accurate GPS will provide a reduction in SAR targeting errors. This phenomenon will be analyzed by determining the covariance of the SAR targeting errors to determine how accurate the target position was estimated. SAR targeting results will be produced for each separate GPS simulation.

3.3. Inertial Navigation System Model

The INS presented in this simulation is the LN-93 strapdown, wander azimuth INS. This model has been used in several simulation research projects and has proven to provide real world characteristics [1-3, 8, 20, 21, 23-25, 27-30]. The following section will outline the model used to represent this INS for the system integration research. Since the INS provides no actual measurements to the navigation Kalman filter, all states associated with the INS are modeled in the state dynamics matrix. The barometric and radar altimeters augment the INS to account for vertical channel instabilities and are presented in Section 3.4. The altimeters provide measurements of aircraft altitude which are accounted for in the navigation Kalman filter.

Litton developed a 93-state error model describing the error characteristics of the LN-93 INS [2, 8, 24]. These error states, represented by the vector $\delta\mathbf{x}$, have been split into 6 different categories:

$$\delta\mathbf{x} = [\delta\mathbf{x}_1^T \delta\mathbf{x}_2^T \delta\mathbf{x}_3^T \delta\mathbf{x}_4^T \delta\mathbf{x}_5^T \delta\mathbf{x}_6^T]^T \tag{38}$$

where $\delta\mathbf{x}$ is a 93x1 column vector with the following characteristics

$\delta\mathbf{x}_1$ represents the most often used general error vector containing 13 position, velocity, and vertical channel errors.

$\delta\mathbf{x}_2$ consists of 16 gyro, accelerometer, and baro-altimeter exponentially time-correlated errors, and “trend” states. These states are modeled as first order Markov processes in both the truth model and in the Kalman filter model.

$\delta\mathbf{x}_3$ represents gyro bias errors. These 18 states are modeled as random constants in the truth model and are modeled as random walks (with small magnitude pseudo-noises [4, 5]) in the Kalman filter.

$\delta\mathbf{x}_4$ is composed of the accelerometer bias error states. These 22 states are modeled in exactly the same manner as the gyro bias states.

$\delta\mathbf{x}_5$ depicts accelerometer and initial thermal transients. The 6 thermal transient states are first order Markov processes in the system and Kalman filter.

$\delta\mathbf{x}_6$ models the gyro compliance errors. These 18 error states are modeled as biases in the system model and as random walks in the Kalman filter.

The INS truth model state space differential equation has the following form:

$$\begin{bmatrix} \dot{\delta\mathbf{x}}_1 \\ \dot{\delta\mathbf{x}}_2 \\ \dot{\delta\mathbf{x}}_3 \\ \dot{\delta\mathbf{x}}_4 \\ \dot{\delta\mathbf{x}}_5 \\ \dot{\delta\mathbf{x}}_6 \end{bmatrix} = \begin{bmatrix} \mathbf{F}_{11} & \mathbf{F}_{12} & \mathbf{F}_{13} & \mathbf{F}_{14} & \mathbf{F}_{15} & \mathbf{F}_{16} \\ 0 & \mathbf{F}_{22} & 0 & 0 & 0 & 0 \\ 0 & 0 & 0 & 0 & 0 & 0 \\ 0 & 0 & 0 & 0 & 0 & 0 \\ 0 & 0 & 0 & 0 & \mathbf{F}_{55} & 0 \\ 0 & 0 & 0 & 0 & 0 & 0 \end{bmatrix} \begin{bmatrix} \delta\mathbf{x}_1 \\ \delta\mathbf{x}_2 \\ \delta\mathbf{x}_3 \\ \delta\mathbf{x}_4 \\ \delta\mathbf{x}_5 \\ \delta\mathbf{x}_6 \end{bmatrix} + \begin{bmatrix} \mathbf{w}_1 \\ \mathbf{w}_2 \\ 0 \\ 0 \\ 0 \\ 0 \end{bmatrix} \tag{39}$$

using the full 93-state truth model.

Negast provides a reduced order truth model, reducing the truth model order from 93 to 39-states, using the tuning process defined in Sections 2.2.5.1and 2.2.5.2. This reduced order truth model is represented by the following state space differential equation:

$$\begin{bmatrix} \dot{\delta\mathbf{x}}_1 \\ \dot{\delta\mathbf{x}}_2 \\ \dot{\delta\mathbf{x}}_3 \\ \dot{\delta\mathbf{x}}_4 \end{bmatrix} = \begin{bmatrix} \mathbf{F}_{(red)11} & \mathbf{F}_{(red)12} & \mathbf{F}_{(red)13} & \mathbf{F}_{(red)14} \\ 0 & \mathbf{F}_{(red)22} & 0 & 0 \\ 0 & 0 & 0 & 0 \\ 0 & 0 & 0 & 0 \end{bmatrix} \begin{bmatrix} \delta\mathbf{x}_1 \\ \delta\mathbf{x}_2 \\ \delta\mathbf{x}_3 \\ \delta\mathbf{x}_4 \end{bmatrix} + \begin{bmatrix} \mathbf{w}_1 \\ \mathbf{w}_2 \\ 0 \\ 0 \end{bmatrix} \tag{40}$$

The sub-matrices in Equation (40) are similar to those in Equation (39), however additional tuning was performed to create the reduced order model. Appendix B contains a complete list of the 93-state INS truth model, the 39-state INS truth model used in this research, and the tuning values used to compensate for the reduced order model [1-3, 24].

3.4. Barometric / Radar Altimeter Model

The barometric and radar altimeters provide the only measurements from the integrated INS/Altimeter model [2]. The altimeters compensate for the INS's inherent instability in the vertical channel. The altimeter output, Alt_{Baro}, is modeled as the sum of the true altitude h_t, the total error in the barometric altimeter, δh_B, and a random measurement noise v. In order to utilize the difference measurement described by Equation (13), the barometric altimeter measurement is differenced with an INS calculated altitude, Alt_{INS}. The INS calculated altitude is the sum of the true altitude and the INS error in vehicle altitude above the referenced ellipsoid, δh. The following difference measurement equation eliminates the unknown true altitude resulting in:

$$\begin{aligned} \delta z &= Alt_{INS} - Alt_{BARO} \\ &= [h_t + \delta h] - [h_t + \delta h_B - v] \\ &= \delta h - \delta h_B + v \end{aligned} \tag{41}$$

The INS error in vehicle altitude above the reference ellipsoid, δh, and total barometric altimeter correlated error, δh_B, are included in the 39-state error model for the INS, shown in Appendix B with barometric aiding.

The differenced measurement equation of the radar altimeter is similar to the barometric altimeter. Errors in the radar altimeter measurement, Alt_{Ralt}, are modeled as

white noise (no time correlated component as in the barometric altimeter). Thus, the difference measurement for the radar altimeter is:

$$\begin{aligned} \delta z &= Alt_{INS} - Alt_{Ralt} \\ &= [h_t + \delta h] - [h_t - v] \\ &= \delta h + v \end{aligned} \tag{42}$$

The radar altimeter measurement noise covariance, R_{Ralt}, is a function of altitude above ground level (AGL), is altitude dependent, and represented by the following relationship:

$$R_{Ralt} = \{[0.01]^2 [\mathrm{AGL}_{true}\, ft]^2\} + 0.25\, ft^2 \tag{43}$$

It should be noted that the radar altimeter is modeled to provide altitude measurements after the aircraft drops below 3000-*ft* AGL. However, the simulated flight trajectory for the U-2 in this research will never drop below the radar altimeter threshold. This model however is integral to the existing software code from previous theses [1-3, 8, 27-30]. Therefore, the description of the radar altimeter and its function is provided here in case a different flight profile is used (i.e. for an F-15E SAR integration simulation).

3.5. Global Positioning System Model

GPS receivers process signals from the GPS satellite constellation to produce a very accurate receiver position. The position is based on the pseudorange measurement from several satellites to the receiver. For this research, the GPS receiver has four channels, meaning the receiver can track up to four satellites. It is relatively simple to simulate more channels. However, in doing so, the Kalman filter model and truth model order is increased by four-states per channel. For ease of computation and simulation speed, a four channel GPS receiver model provides an adequate representation of the performance

of the GPS portion of the INS/GPS/SAR integration. Three different GPS receiver implementations are modeled and will be developed in the following sections. The stand-alone and Differential GPS simulation models follow the development of White and Negast [2, 8]. The Carrier Phase GPS model follows the development of Bohenek [20].

3.5.1. Stand-Alone GPS

The stand-alone GPS receiver scenario is represented in Figure 9. The range between multiple SVs and the receiver is processed into a highly accurate receiver position. However, each SV is subject to many errors that affect the measurement. Atmospheric errors, clock errors, satellite position errors, etc. all contribute to an error filled range measurement. As shown in Figure 9, these errors increase or decrease the range distance between the receiver and transmitting satellite. Since the receiver clock can produce a large error in the range measurement, the range between the satellite and receiver is called a "pseudorange." The following paragraphs will describe how each of these errors is modeled to simulate the GPS environment for the truth model. The filter models for stand-alone GPS dynamics and measurements will be developed in Sections 3.7.2 and 3.7.3, respectively.

3.5.1.1. Stand-Alone GPS Error Model Equations

Negast developed a 30-state GPS truth model which has proven to be an effective model of GPS error sources [8]. Appendix B contains a tabular listing of each state used in the 30-state stand-alone GPS truth model. The first two states of the truth model represent the receiver clock bias, x_{Uclk_b}, and clock bias drift errors, $x_{Uclk_{dr}}$; the state

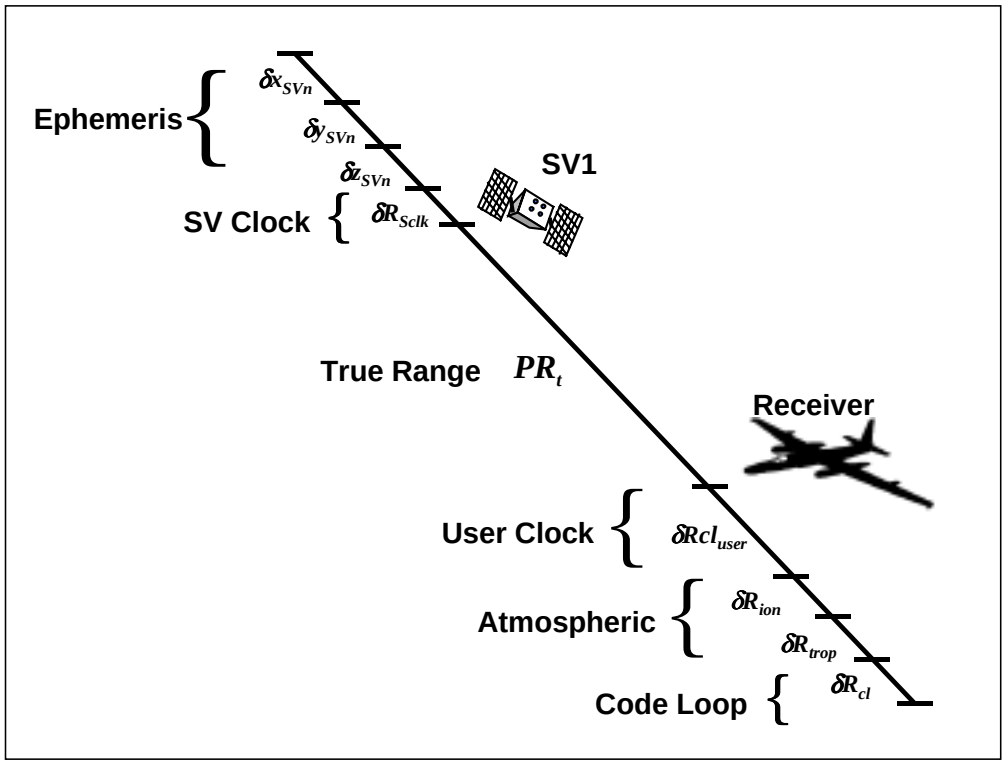

Figure 9. Stand-Alone GPS Technique

differential equation model is:

$$\begin{bmatrix} \dot{x}_{Uclk_b} \\ \dot{x}_{Uclk_{dr}} \end{bmatrix} = \begin{bmatrix} 0 & 1 \\ 0 & 0 \end{bmatrix} \begin{bmatrix} x_{Uclk_b} \\ x_{Uclk_{dr}} \end{bmatrix} \tag{44}$$

where the initial state estimate for each state is zero, with covariances:

$$\mathbf{P}_{Uclk_b,Uclk_{dr}}(t_0) = \begin{bmatrix} 9.0\text{x}10^{14}\ ft^2 & 0 \\ 0 & 9.0\text{x}10^{10}\ ft^2\ /\ \sec^2 \end{bmatrix} \tag{45}$$

The huge covariances associated with the receiver clock bias and drift terms is typical of military airborne receivers. Until the clock error is determined, it is the dominant error source in the system.

The next 22 states in the GPS truth model are associated with each individual SV (of which there are four). The GPS receiver uses code and carrier tracking loops to lock onto a satellite transmitter. The tracking loops help match an internal GPS code generator to the GPS signal which in turn provides the pseudorange information and ephemeris data from each respective SV. The error in the code tracking loop is a typical error for GPS and is modeled as part of the GPS truth model. Code tracking loop error, δR_{cl}, is modeled as a first order Markov process [2, 4, 8]. Atmospheric errors, per satellite, are included in the GPS truth model. The tropospheric error, δR_{trop}, and ionospheric error, δR_{ion}, are also modeled as first order Markov processes. The final two error sources are the specific SV clock error, δR_{Sclk}, and SV position error: δx_{SVj}, δy_{SVj}, and δz_{SVj}. All GPS error sources are modeled using the following state differential equations, initial covariances, and zero mean, white noise components:

$$\begin{bmatrix} \delta\dot{R}_{cl} \\ \delta\dot{R}_{trop} \\ \delta\dot{R}_{ion} \\ \delta\dot{R}_{Sclk} \\ \delta\dot{x}_{SVj} \\ \delta\dot{y}_{SVj} \\ \delta\dot{z}_{SVj} \end{bmatrix} = \begin{bmatrix} -1 & 0 & 0 & 0 & 0 & 0 & 0 \\ 0 & -\frac{1}{500} & 0 & 0 & 0 & 0 & 0 \\ 0 & 0 & -\frac{1}{1500} & 0 & 0 & 0 & 0 \\ 0 & 0 & 0 & 0 & 0 & 0 & 0 \\ 0 & 0 & 0 & 0 & 0 & 0 & 0 \\ 0 & 0 & 0 & 0 & 0 & 0 & 0 \\ 0 & 0 & 0 & 0 & 0 & 0 & 0 \end{bmatrix} \begin{bmatrix} \delta R_{cl} \\ \delta R_{trop} \\ \delta R_{ion} \\ \delta R_{Sclk} \\ \delta x_{SVj} \\ \delta y_{SVj} \\ \delta z_{SVj} \end{bmatrix} + \begin{bmatrix} w_{cl} \\ w_{trop} \\ w_{ion} \\ 0 \\ 0 \\ 0 \\ 0 \end{bmatrix} \tag{46}$$

$$\mathbf{P}_{GPS}(t_0) = \begin{bmatrix} 0.25\,ft^2 & 0 & 0 & 0 & 0 & 0 & 0 \\ 0 & 1.0\,ft^2 & 0 & 0 & 0 & 0 & 0 \\ 0 & 0 & 1.0\,ft^2 & 0 & 0 & 0 & 0 \\ 0 & 0 & 0 & 25\,ft^2 & 0 & 0 & 0 \\ 0 & 0 & 0 & 0 & 25\,ft^2 & 0 & 0 \\ 0 & 0 & 0 & 0 & 0 & 25\,ft^2 & 0 \\ 0 & 0 & 0 & 0 & 0 & 0 & 25\,ft^2 \end{bmatrix} \tag{47}$$

$$E\{\mathbf{w}_{GPS}(t)\mathbf{w}_{GPS}(t+\tau)\} = \begin{bmatrix} 0.5 & 0 & 0 & 0 & 0 & 0 & 0 \\ 0 & 0.004 & 0 & 0 & 0 & 0 & 0 \\ 0 & 0 & 0.004 & 0 & 0 & 0 & 0 \\ 0 & 0 & 0 & 0 & 0 & 0 & 0 \\ 0 & 0 & 0 & 0 & 0 & 0 & 0 \\ 0 & 0 & 0 & 0 & 0 & 0 & 0 \\ 0 & 0 & 0 & 0 & 0 & 0 & 0 \end{bmatrix} m^2 / sec \cdot \delta(\tau) \tag{48}$$

The 30-state truth model contains both user error states and four versions of Equation (46), one per SV.

3.5.1.2. Stand-Alone GPS Measurement Model

As shown in Figure 9, the pseudorange provided by the stand-alone GPS receiver is the sum of the true range from satellite to receiver plus errors, including random measurement noise. Equation (49) shows the total calculation of the GPS filter pseudorange measurement:

$$R_{GPS} = R_{t_j} + \delta R_{cl_j} + \delta R_{trop_j} + \delta R_{ion_j} + \delta R_{Sclk_j} + \delta R_{Uclk_j} - v_j \tag{49}$$

where j = 1 through 4 for each SV. Since the true range, R_t, from SV to receiver can never be measured perfectly, a difference measurement (Equation (13)) is performed to eliminate this term. This difference measurement is formulated by calculating a "range" from the INS position and the ephemeris provided satellite position, and subtracting the INS range from the GPS pseudorange. The INS Range, R_{INS}, can be calculated as follows:

$$R_{INS} = \left|\mathbf{X}_U - \mathbf{X}_S\right| = \left|\begin{bmatrix} x_U \\ y_U \\ z_U \end{bmatrix} - \begin{bmatrix} x_S \\ y_S \\ z_S \end{bmatrix}\right| \tag{50}$$

where $\mathbf{X}_U$ is the aircraft position as provided by the INS and $\mathbf{X}_S$ is the SV position (in ECEF coordinates). R_{INS} can also be represented by:

$$R_{INS} = \sqrt{(x_U - x_S)^2 + (y_U - y_S)^2 + (z_U - z_S)^2} \tag{51}$$

Since the INS calculated range is a nonlinear function of the aircraft and satellite position, a truncated first order Taylor series is performed to linearize Equation (51) for use in the EKF for this research. Linearizing the INS range equation also reformats the INS range in terms of the error states needed in the perturbation models for the EKF, δx, δy, δz. Evaluating the Taylor expansion yields,

$$R_{INS} = R_t + \left.\frac{\partial R_{INS}(\mathbf{X}_S, \mathbf{X}_U)}{\partial \mathbf{X}_S}\right|_{(\mathbf{X}_S, \mathbf{X}_U)_{nom}} \cdot \delta \mathbf{X}_S \;+\; \left.\frac{\partial R_{INS}(\mathbf{X}_S, \mathbf{X}_U)}{\partial \mathbf{X}_U}\right|_{(\mathbf{X}_S, \mathbf{X}_U)_{nom}} \cdot \delta \mathbf{X}_U \tag{52}$$

then substitute Equation (51) into Equation (52) and compute the partial derivative to produce the linearized INS calculated range:

$$\begin{aligned} R_{INS} = R_t &- \left[\frac{x_S - x_U}{|R_{INS}|}\right] \cdot \delta x_U - \left[\frac{y_S - y_U}{|R_{INS}|}\right] \cdot \delta y_U - \left[\frac{z_S - z_U}{|R_{INS}|}\right] \cdot \delta z_U \\ &+ \left[\frac{x_S - x_U}{|R_{INS}|}\right] \cdot \delta x_S + \left[\frac{y_S - y_U}{|R_{INS}|}\right] \cdot \delta y_S + \left[\frac{z_S - z_U}{|R_{INS}|}\right] \cdot \delta z_S \end{aligned} \tag{53}$$

in terms of the perturbation aircraft position states, δx_u, δy_u, δz_u. The *truth model* GPS pseudorange difference measurement is provided by subtracting Equation (53) from Equation (49):

$$\begin{aligned} \delta z_{PR_j} &= R_{INS\,j} - R_{GPS\,j} \\ &= -\left[\frac{x_S - x_U}{|R_{INS}|}\right] \cdot \delta x_U - \left[\frac{y_S - y_U}{|R_{INS}|}\right] \cdot \delta y_U - \left[\frac{z_S - z_U}{|R_{INS}|}\right] \cdot \delta z_U \\ &\quad + \left[\frac{x_S - x_U}{|R_{INS}|}\right] \cdot \delta x_S + \left[\frac{y_S - y_U}{|R_{INS}|}\right] \cdot \delta y_S + \left[\frac{z_S - z_U}{|R_{INS}|}\right] \cdot \delta z_S \\ &\quad - \delta R_{cl_j} - \delta R_{trop_j} - \delta R_{ion_j} - \delta R_{Sclk_j} - \delta R_{Uclk} + v \end{aligned} \tag{54}$$

3.5.2. Differential GPS

Differential positioning GPS (DGPS) is slightly more complex than stand-alone GPS. Figure 10 describes the DGPS positioning technique using an accurate surveyed position for the location of the ground based receiver. This reference receiver processes the pseudorange data from all available satellites. The ground receiver usually contains highly accurate clocks which reduce the user clock errors previously discussed. Since the ground receiver's position is precisely known and its own clock errors are extremely small, each SV's position, clock, and atmospheric errors become observable in the pseudorange measurement [8]. This allows the ground receiver to estimate the errors associated with each SV very precisely. The estimates of the SV errors are called differential corrections and can be transmitted from the ground receiver to an airborne DGPS receiver. The airborne receiver will than use the differential corrections to remove the proper errors from its own pseudorange measurement.

There are a few assumptions that are critical to modeling this DGPS technique. First, it is assumed that the airborne receiver has access to the same satellites as the ground based receiver. Second, it is also assumed for modeling purposes that the differential corrections are all timed correctly to correspond to the right airborne pseudorange measurement. Last, when processing DGPS measurements, it is assumed that the differential corrections have been applied to the raw pseudorange measurements from the airborne receiver [8]. During standoff reconnaissance missions, like those typically flown by the U-2, these assumptions can be properly invoked as the aircraft will likely fly near a differential transmitter.

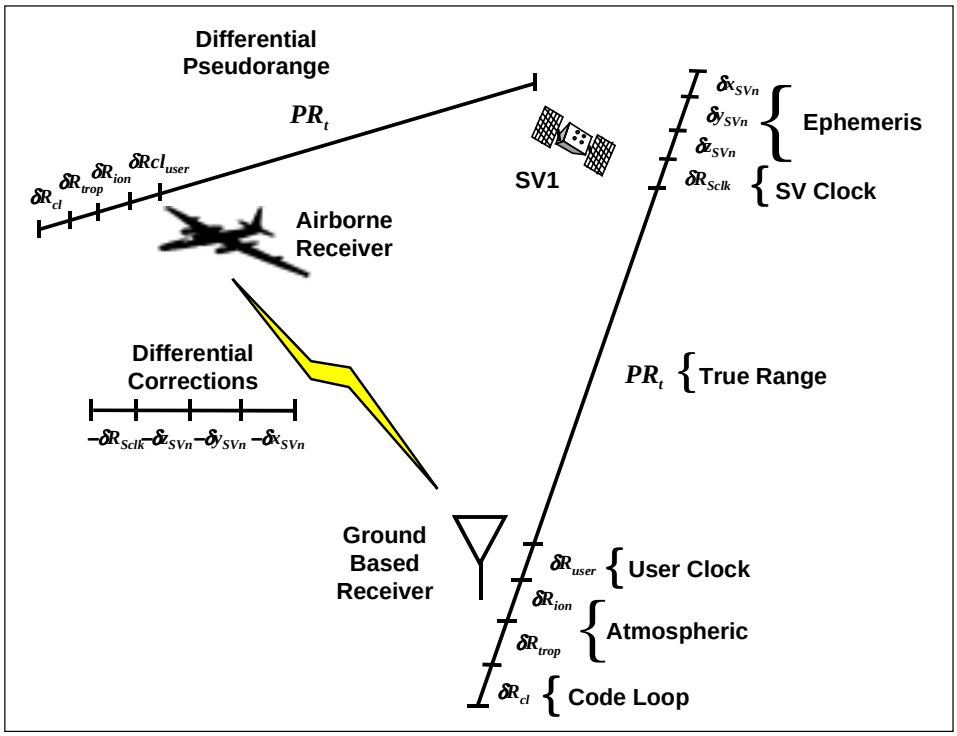

Figure 10. Differential GPS Technique

3.5.2.1. Differential GPS Error Model Equations

The DGPS error model is fabricated almost exactly as the stand-alone GPS error model. As previously mentioned the first difference is the removal of the SV clock error through differential corrections. A second difference is the absorption of the receiver code loop error into the noise variance in the pseudorange measurement [8]. This leaves the user clock errors, atmospheric errors, and satellite position errors which comprise a 22-state DGPS truth model. However, only the user clock errors retain the same characteristics as the stand-alone GPS model (Section 3.5.1.1, Equations (44) and (45)). Appendix B, contains a list of all 22 states of the DGPS truth model used in this research.

The *j*-satellite specific atmospheric and position DGPS error models are slightly different than the stand-alone GPS model. All truth model DGPS error sources are

modeled using the following state differential equations, initial covariances, and zero mean, white noise components [8]:

$$\begin{bmatrix} \delta\dot{R}_{trop} \\ \delta\dot{R}_{ion} \\ \delta\dot{x}_{SVj} \\ \delta\dot{y}_{SVj} \\ \delta\dot{z}_{SVj} \end{bmatrix} = \begin{bmatrix} -\frac{1}{1500} & 0 & 0 & 0 & 0 \\ 0 & -\frac{1}{1500} & 0 & 0 & 0 \\ 0 & 0 & 0 & 0 & 0 \\ 0 & 0 & 0 & 0 & 0 \\ 0 & 0 & 0 & 0 & 0 \end{bmatrix} \begin{bmatrix} \delta R_{trop} \\ \delta R_{ion} \\ \delta x_{SVj} \\ \delta y_{SVj} \\ \delta z_{SVj} \end{bmatrix} + \begin{bmatrix} w_{trop} \\ w_{ion} \\ 0 \\ 0 \\ 0 \end{bmatrix} \tag{55}$$

$$\mathbf{P}_{DGPS}(t_0) = \begin{bmatrix} 1.0\,ft^2 & 0 & 0 & 0 & 0 \\ 0 & 1.0\,ft^2 & 0 & 0 & 0 \\ 0 & 0 & .35\,ft^2 & 0 & 0 \\ 0 & 0 & 0 & .35\,ft^2 & 0 \\ 0 & 0 & 0 & 0 & .35\,ft^2 \end{bmatrix} \tag{56}$$

$$E\{\mathbf{w}_{DGPS}(t)\mathbf{w}_{DGPS}(t+\tau)\} = \begin{bmatrix} 0.001 & 0 & 0 & 0 & 0 \\ 0 & 0.0004 & 0 & 0 & 0 \\ 0 & 0 & 0 & 0 & 0 \\ 0 & 0 & 0 & 0 & 0 \\ 0 & 0 & 0 & 0 & 0 \end{bmatrix} ft^2 / sec \cdot \delta(\tau) \tag{57}$$

The three equations above correlate back to a specific j-satellite. Coupled with the two user clock states, four sets of the equations above (for 4 SVs) provides a total of 22 DGPS error states. These states are listed in Table 20.

3.5.2.2. Differential GPS Measurement Model

Like the stand-alone GPS pseudorange measurement, Equation (49), the DGPS pseudorange measurement equation is modeled as:

$$R_{DGPS} = R_t + \delta R_{trop} + \delta R_{ion} + \delta R_{Uclk} + v \tag{58}$$

where all differential corrections have been applied and v is zero-mean white gaussian measurement noise. In order to use the difference measurement technique previously

discussed, Equation (58) is subtracted from the INS calculated range to form *the truth model* DGPS difference measurement:

$$\begin{aligned}\delta z_{PR_j} &= R_{INS\,j} - R_{DGPS\,j} \\ &= -\left[\frac{x_S - x_U}{|R_{INS}|}\right]\cdot \delta x_U - \left[\frac{y_S - y_U}{|R_{INS}|}\right]\cdot \delta y_U - \left[\frac{z_S - z_U}{|R_{INS}|}\right]\cdot \delta z_U \\ &\quad + \left[\frac{x_S - x_U}{|R_{INS}|}\right]\cdot \delta x_S + \left[\frac{y_S - y_U}{|R_{INS}|}\right]\cdot \delta y_S + \left[\frac{z_S - z_U}{|R_{INS}|}\right]\cdot \delta z_S \\ &\quad - \delta R_{trop_j} - \delta R_{ion_j} - \delta R_{Uclk} - v\end{aligned} \tag{59}$$

Differential GPS dynamics and measurement filter models will be discussed in Sections 3.7.2 and 3.7.3. Note that multipath error is not included in the DGPS measurement model. Multipath noise is generated when reflected GPS signals are processed in the GPS receiver. Normally, this noise is very small and can be assumed within the measurement noise. However, when differential corrections are applied, the multipath noise can become one of the most dominant error sources. Since the U-2 receiver is at a considerable altitude, 65000-*ft*, it is assumed the multipath noise would primarily affect the differential reference receiver. In this research multipath is assumed to be covered within the receiver measurement noise, *v*.

3.5.3. Carrier Phase Differential GPS

The carrier phase GPS model presented here follows the development of Bohenek using floating ambiguity resolution [20]. Unlike single and differential GPS, the carrier phase GPS receiver does not process the GPS signal into a pseudorange. A carrier phase measurement is the result of subtracting the generated carrier signal of the receiver from the carrier signal transmitted by a specific GPS satellite [20]. The subtraction of these

signals produces a phase range, also known as the carrier phase observable. As described in [20], the carrier phase observable equation is:

$$\Phi = -f \cdot (dT - dt) - \tfrac{f}{c} \cdot (R_t - d_{ion} + d_{trop}) \tag{60}$$

where

f = frequency of carrier signal
dT = transmission time offset from true GPS time
dt = user clock offset from true GPS time
R_t = true range from receiver to satellite
d_{ion} = range equivalent of ionospheric delay
d_{trop} = range equivalent of tropospheric delay
c = speed of light

The carrier phase measurement is the measurement of the phase shift between the satellite generated carrier signal and the receiver generated carrier signal. The phase shift represents a fraction of the total carrier frequency wavelength, so the total phase range measurement between receiver and satellite is

$$\Phi_{total}(t) = \Phi_{frac}(t) + \Phi_{int}(t_0, t) + N(t_o) \tag{61}$$

where $\Phi_{frac}(t)$ is the fraction of total wavelength, $\Phi_{int}(t_0, t)$ is the integer number of phase cycles from the initial reception time to the current time, and $N(t_o)$, is the integer phase ambiguity term. $N(t_o)$ is the difference between the true integer count at the initial time and the current integer count at t_o measured or calculated by the receiver [20]. Figure 11 describes the relationship between each facet of the carrier phase measurement. As shown in Figure 11, the total phase range is equal to the integer ambiguity, integer portion of phase range, and fractional portion of phase range.

Assuming that the Φ term from Equation (60) is the measured phase observation, it can be represented as the sum of the fraction and integer phase observations (Φ_{frac} and

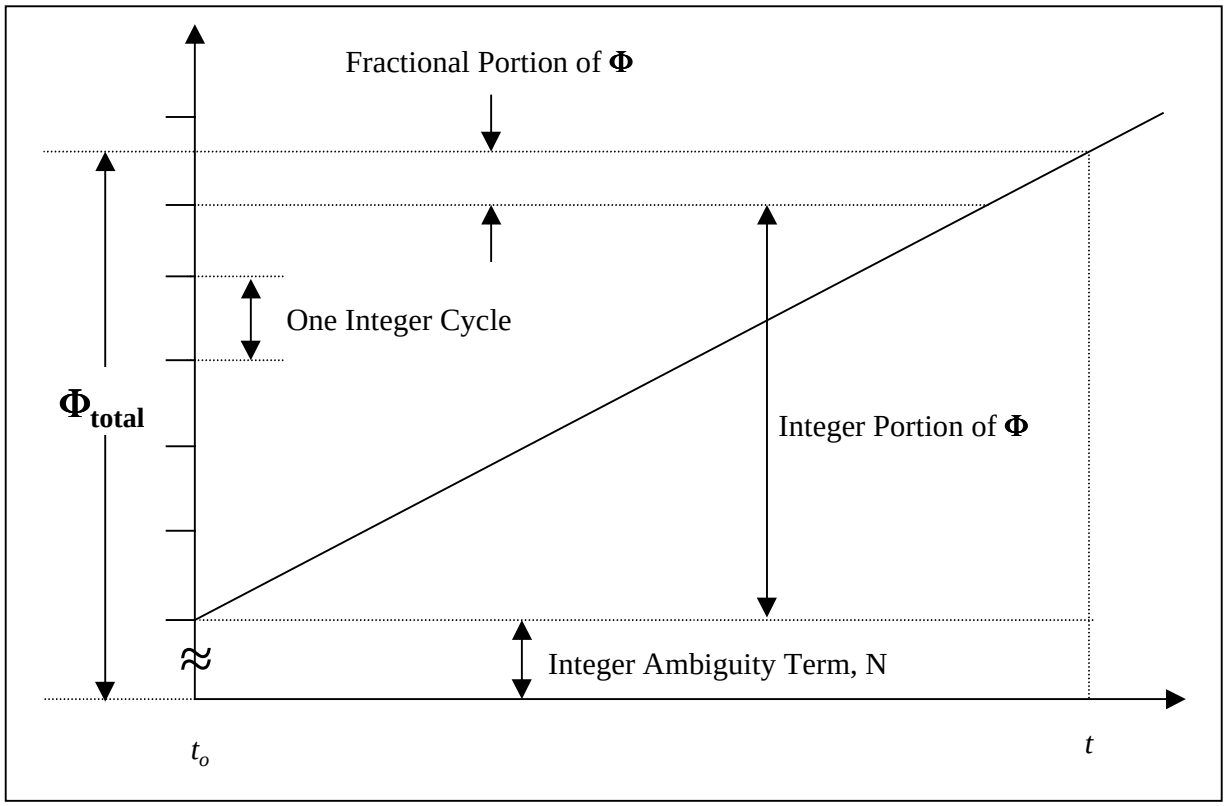

Figure 11. Carrier Phase GPS Scenario [20]

Φ_{int}). Therefore, the total phase range can be written as the sum of the measured phase observation and the integer ambiguity term, *N(t)*. If the total phase range is subtracted from Equation (60), the measured phase range for the carrier phase observable is:

$$\Phi_{measured}(t) = -f \cdot (dT - dt) - \tfrac{f}{c} \cdot (R_t - d_{ion} + d_{trop}) - N(t) \tag{62}$$

which is the measured phase range in carrier cycles [20]. To convert to feet (more desirable for a "range" definition), Equation (62) is multiplied by the carrier wavelength, λ, providing:

$$\Phi(t) = R_t + c(dT - dt) + d_{ion} - d_{trop} + \lambda N(t) \tag{63}$$

When the signal between the carrier phase receiver and the satellite is lost it is called a cycle slip. During this loss, the receiver cannot count the integer phase cycles. As a result the receiver may lock onto the wrong integer phase cycle causing the receiver to

lose signal lock. Since this research is only interested in determining the effect of GPS on SAR targeting, cycle slips will not be simulated or investigated. However, future researchers should determine the effect of cycle slips on targeting accuracy.

3.5.3.1. Carrier Phase Differential GPS Error Model Equations

Carrier phase GPS (CPGPS) receivers are generally differential receivers as well. This means that the airborne CPGPS receiver has access to differential corrections that can eliminate several error sources (as previously defined). The error model equations for the CPGPS model are similar to the differential GPS model with the addition of the integer ambiguity error. These new states, one for each of the four satellites, are added to the existing differential states (clock error, satellite position error, etc.) in the following manner:

$$\begin{bmatrix} \delta\dot{R}_{N_1} \\ \delta\dot{R}_{N_2} \\ \delta\dot{R}_{N_3} \\ \delta\dot{R}_{N_4} \end{bmatrix} = \begin{bmatrix} 0 & 0 & 0 & 0 \\ 0 & 0 & 0 & 0 \\ 0 & 0 & 0 & 0 \\ 0 & 0 & 0 & 0 \end{bmatrix} \begin{bmatrix} \delta R_{N_1} \\ \delta R_{N_2} \\ \delta R_{N_3} \\ \delta R_{N_4} \end{bmatrix} + \begin{bmatrix} w_1 \\ w_2 \\ w_3 \\ w_4 \end{bmatrix} \tag{64}$$

with initial state covariance

$$\mathbf{P}_{\delta R_N}(t_0) = \begin{bmatrix} 13\,ft^2 & 0 & 0 & 0 \\ 0 & 13\,ft^2 & 0 & 0 \\ 0 & 0 & 13\,ft^2 & 0 \\ 0 & 0 & 0 & 13\,ft^2 \end{bmatrix} \tag{65}$$

The ambiguity states are modeled as random biases as long as there are no cycle slips. In addition, the 13-ft^2 value for the initial state covariance is used under the assumption that initially, the CPGPS measurement is only as accurate as a typical differential GPS receiver and has access to code measurements. Appendix B, Table 21 contains a list of

the 4-states added to the differential GPS model to create the CPGPS model as well as all white noise values from Equation (64).

3.5.3.2. Carrier Phase Differential GPS Measurement Model

The measurement model for the CPGPS measurements is different than that of the differential GPS model. Since the CPGPS receiver must account for the integer ambiguity term, *N(t)*, an additional error in the range measurement is produced, δR_N . In order for the ambiguity term to become observable in the CPGPS measurement equations, the "double differencing" technique is applied. The double differencing performed in this work is between the airborne receiver and two separate satellites. This method subtracts a between-receiver single difference measurement with another between-receiver single difference measurement using the same receiver and two different satellites to produce the following equation:

$$\nabla\Delta R^{ij} = R_t^{ij} - \nabla\Delta R_{ion}^{ij} + \nabla\Delta R_{trop}^{ij} + \nabla\Delta R_N^{ij} + \nabla\Delta v^{ij} \tag{66}$$

where *i* and *j* represent the two different satellites from which measurements are taken.

Applying the double difference technique to the carrier phase range measurement equation still utilizes the difference measurement technique described with Equation (13). The carrier phase range measurement becomes:

$$R_{CPGPS} = R_t + \delta R_{Uclk} - \delta R_{ion} + \delta R_{trop} + \delta R_N + v \tag{67}$$

where the δR_N term represents the range equivalent of the cycle ambiguity term [28]. Equation (67) represents one of the single difference measurements previously described. The "between-satellites" single difference transforms Equation (67) into:

$$\nabla\Delta R_{CPGPS}^{ij} = R_t^{ij} - \nabla\Delta R_{ion}^{ij} + \nabla\Delta R_{trop}^{ij} + \nabla\Delta R_N^{ij} + \nabla\Delta v^{ij} \tag{68}$$

The measurement noise term, v^{ij}, is now doubled (2 x $E[v^2]$) under the assumption that the satellite measurements are independent of each other [28]. With four satellites, the *i*/*j* combinations are: 1 and 4, 2 and 4, and 3 and 4 using satellite 4 as the base satellite. The INS computed "between-satellites" range is:

$$\nabla \Delta R_{INS}^{ij} = \nabla R_t^{ij} - A\delta X_U - B\delta Y_U - C\delta Z_U + A\nabla \delta X_S^{ij} + B\nabla \delta Y_S^{ij} + C\nabla \delta Z_S^{ij} \tag{69}$$

where:

$$A = \left[\frac{X_S^i - X_U}{|R_{INS}|} - \frac{X_S^j - X_U}{|R_{INS}|} \right]$$

$$B = \left[\frac{Y_S^i - Y_U}{|R_{INS}|} - \frac{Y_S^j - Y_U}{|R_{INS}|} \right]$$

$$C = \left[\frac{Z_S^i - Z_U}{|R_{INS}|} - \frac{Z_S^j - Z_U}{|R_{INS}|} \right]$$

To form the *truth model* difference measurement for CPGPS range measurements, the INS calculated range, Equation (69), is subtracted from Equation (67) to produce:

$$\begin{aligned} \delta z_{CPGPS_{DD}} &= \nabla R_{INS}^{ij} - \nabla R_{CPGPS}^{ij} \\ &= -A \cdot \delta x_U - B \cdot \delta y_U - C \cdot \delta z_U \\ &\quad + A \cdot \delta x_S^{ij} + B \cdot \delta y_S^{ij} + C \cdot \delta z_S^{ij} \\ &\quad - \nabla \delta R_{ion}^{ij} - \nabla \delta R_{trop}^{ij} - \nabla R_N^{ij} - \nabla v^{ij} \end{aligned} \tag{70}$$

This method eliminates the user clock bias terms which dominate the SGPS and DGPS models. This will result in a 2-state decrease in the CPGPS truth and filter models.

3.6. Synthetic Aperture Radar Model

The Synthetic Aperture Radar (SAR) is one of the most common imaging sensors in the USAF. The primary function of a military SAR sensor is to generate high resolution radar images of ground terrain and ground targets [11]. The two basic measurements a SAR provides are range and range rate to a target. SAR range is defined as:

$$r = \frac{cT}{2} \tag{71}$$

where T is the transmit time of the transmitted pulse (from transmit to receipt) and c is the speed of light. Range rate is defined as:

$$\dot{r} = \frac{cF_d}{2F} \tag{72}$$

where F_d is the Doppler frequency shift and F is the frequency of the SAR. Using these two basic radar equations, the SAR error models can be developed for use in the integrated Kalman filter.

Generally, a SAR contains a wide beam antenna which illuminates a large area on the ground. The SAR transmits a radar pulse and samples the magnitude and phase of the return signal. Since radar waves propagate at nearly a constant speed in the Earth's atmosphere, the earliest samples correspond to the points on the ground nearest the aircraft. Likewise, the return from more distant points are represented by later samples. The data samples are stored in vectors referred to as *range bins*. These range bins are then processed (using a number of different techniques) into ground images using the magnitude and phase characteristics of each received pulse. Layne provides a description of SAR processing techniques in [11]. The reader is referred to [15] for a more detailed analytical description of SAR characteristics and processing.

The term synthetic aperture is used because the aircraft utilizes the motion of the aircraft to synthesize the effect of a large aperture antenna from a physically small aperture antenna. Since aperture size is directly correlated with SAR resolution, the larger the aperture, the higher the SAR resolution. Therefore, a SAR capable of creating a large synthetic aperture can achieve significant resolution increases while maintaining a physical radar aperture that is much smaller. Abbot describes the relationship between resolution and aircraft speed in [15]. The resolution distance, ρ_a, capable from a SAR is

directly related to the slant range interval, ΔR, the radar signal speed, c, and the velocity of the aircraft, v, as shown:

$$\frac{2\Delta R}{\rho_a} = \frac{v}{c} \tag{73}$$

For ground mapping, a small resolution distance provides high imagery resolution resulting in better ground targeting.

As with the INS and GPS sensors, SAR measurements contain several errors. While Abbott describes SAR errors in detail in his book, there is a dearth of actual simulation models regarding SAR sensors [15]. Layne provides a first cut analytical SAR model in his research, which is repeated in this research with minor adjustments [11, 32]. The most prominent error in SAR measurements is due to aircraft velocity errors. Since SAR uses the velocity of the aircraft to create the synthetic aperture antenna, incorrect interpretation of the aircraft velocity vector can cause problems recording the doppler shift of the range measurement over time. Therefore, range rate measurements from a SAR must be a function of the aircraft velocity errors.

3.6.1. SAR Error Model

As with the INS, GPS, and altimeter models, a SAR error model is developed to determine the errors present in the SAR range and range rate measurements. These SAR error states are included in the extended Kalman filter along with the INS and GPS error states previously defined. The first three states to be included in the Kalman filter are the target position error states: δx_t, δy_t, δz_t. These states define the amount of SAR targeting error in each SAR range and range rate measurement. Using all the information in the Kalman filter, the bottom line performance of the integrated system is determined

through analysis of the target position error states. The relationship between the SAR measurements and these error states is discussed in the next section.

The errors inherent in the SAR itself can cause problems with the range and range rate measurements. First, there are two range measurement errors modeled in this research: range clock error, δr_{CL}, and radar wave propagation speed error, δC [11]. The range clock error is defined as the error in the SAR clock. The SAR clock is responsible for keeping track of the transmit and return time of a radar signal. Any errors associated with drifting clock rate or bias effects can cause a delay in the transmit or return time, thus creating a small error in the range measurement. Radar wave propagation speed is needed to map the measured radar wave transmit time to a range measurement. Any error in the radar wave propagation speed can have a "scale factor" type effect on the range and range rate measurement. These two errors are modeled as random biases with the following characteristics [11]:

$$\begin{bmatrix} \delta \dot{r}_{CL} \\ \delta \dot{C} \end{bmatrix} = \begin{bmatrix} 0 & 0 \\ 0 & 0 \end{bmatrix} \begin{bmatrix} \delta r_{CL} \\ \delta C \end{bmatrix} \tag{74}$$

with initial covariance values of

$$P_{SAR_1}(t_0) = \begin{bmatrix} 1.01\,ft & 0 \\ 0 & 10\,PPM \end{bmatrix} \tag{75}$$

The SAR range rate measurement has similar characteristics as the range measurement. First, since the radar measures range rate through the Doppler frequency of return pulses, any frequency shifts in the pulses will cause bias errors. These frequency shift errors induced through the SAR system are defined as a Doppler shift error, $\delta \dot{r}_D$. The radar wave propagation speed error, δC, can also effect the range rate measurement. The last error source is the frequency error, δF. As shown in Equation

(72), the SAR range rate is a direct function of the radar frequency. Therefore, errors in the frequency of the radar will directly impact the SAR range rate measurement. The range rate errors are modeled as random biases with the following characteristics [11]:

$$\begin{bmatrix} \delta\dot{x}_D \\ \delta\dot{C} \\ \delta\dot{F} \end{bmatrix} = \begin{bmatrix} 0 & 0 & 0 \\ 0 & 0 & 0 \\ 0 & 0 & 0 \end{bmatrix} \begin{bmatrix} \delta x_D \\ \delta C \\ \delta F \end{bmatrix} \tag{76}$$

with initial covariance values of

$$P_{SAR_2}(t_0) = \begin{bmatrix} .001\frac{ft}{sec} & 0 & 0 \\ 0 & 10PPM & 0 \\ 0 & 0 & 20PPM \end{bmatrix} \tag{77}$$

The total SAR *truth model* error state differential equation used in this research is shown in Equation (78) and includes all SAR errors as well as the SAR targeting errors:

$$\begin{bmatrix} \delta\dot{x}_{CL} \\ \delta\dot{r}_D \\ \delta\dot{C} \\ \delta\dot{F} \\ \delta\dot{x}_t \\ \delta\dot{y}_t \\ \delta\dot{z}_t \end{bmatrix} = \begin{bmatrix} 0 & 0 & 0 & 0 & 0 & 0 & 0 \\ 0 & 0 & 0 & 0 & 0 & 0 & 0 \\ 0 & 0 & 0 & 0 & 0 & 0 & 0 \\ 0 & 0 & 0 & 0 & 0 & 0 & 0 \\ 0 & 0 & 0 & 0 & 0 & 0 & 0 \\ 0 & 0 & 0 & 0 & 0 & 0 & 0 \\ 0 & 0 & 0 & 0 & 0 & 0 & 0 \end{bmatrix} \begin{bmatrix} \delta x_{CL} \\ \delta r_D \\ \delta C \\ \delta F \\ \delta x_t \\ \delta y_t \\ \delta z_t \end{bmatrix} + \begin{bmatrix} 0 \\ 0 \\ w_1 \\ w_2 \\ 0 \\ 0 \\ 0 \end{bmatrix} \tag{78}$$

A nominal initial covariance of 100-*ft* per channel was provided to each of the SAR targeting error states. A complete listing of the SAR truth model, with white noise values, can be found in Appendix B, Table 22.

3.6.2. SAR Measurement Model

The SAR measurement model is also developed along the same lines as the INS and GPS models previously discussed. The SAR range and range rate measurements are integrated into the Kalman filter using the difference measurement technique of Equation

(13). An INS calculated range and range rate provides the second measurement type to be subtracted from the SAR measured range and range rate. The SAR range measurement is defined as the true range to the target plus range errors and measurement noise:

$$r_{SAR} = r_{tar} + \delta r_{CL} + r\delta C + v_r \tag{79}$$

where r_{SAR} defined as the range from SAR to target (r is defined as range from aircraft to target as opposed to R which was range from aircraft to GPS satellite). The SAR range rate measurement is defined as the true range rate from the aircraft to the target plus range rate errors and measurement noise:

$$\dot{r}_{SAR} = \dot{r}_{tar} + \delta r_D + \dot{r}\delta C + \dot{r}\delta F + v_{\dot{r}} \tag{80}$$

where $\dot{r}_{SAR}$ is the SAR range rate measurement, and $v_{\dot{r}}$ is the range rate measurement noise. Layne provides an excellent description of each facet of measurement noise for both range and range rate [11]. His work is replicated here.

Assuming the target position has been pre-determined (as discussed in Section 3.2), the INS indicated range to the target is defined as:

$$r_{INS_{tar}} = \sqrt{(x_U - x_{tar})^2 + (y_U - y_{tar})^2 + (z_U - z_{tar})^2} \tag{81}$$

Since this equation is nonlinear, a Taylor series expansion is performed to generate a first order linear equation in terms of the aircraft and target position error states:

$$\begin{aligned} r_{INS_t} = r_{true_{tar}} &- \left[\frac{x_{tar} - x_U}{|R_{INS}|}\right] \cdot \delta x_U - \left[\frac{y_{tar} - y_U}{|R_{INS}|}\right] \cdot \delta y_U - \left[\frac{z_{tar} - z_U}{|R_{INS}|}\right] \cdot \delta z_U \\ &+ \left[\frac{x_{tar} - x_U}{|R_{INS}|}\right] \cdot \delta x_t + \left[\frac{y_{tar} - y_U}{|R_{INS}|}\right] \cdot \delta y_t + \left[\frac{z_{tar} - z_U}{|R_{INS}|}\right] \cdot \delta z_t \end{aligned} \tag{82}$$

The SAR range difference measurement is formed by subtracting Equation (82) from Equation (79):

$$
\begin{aligned}
\delta z_{SAR_r} &= r_{INS} - r_{SAR} \\
&= -\left(\frac{x_U - x_{tar}}{|\mathbf{X}_U - \mathbf{X}_{tar}|}\right)\delta x_U - \left(\frac{y_U - y_{tar}}{|\mathbf{X}_U - \mathbf{X}_{tar}|}\right)\delta y_U - \left(\frac{z_U - z_{tar}}{|\mathbf{X}_U - \mathbf{X}_{tar}|}\right)\delta z_U \\
&\quad + \left(\frac{x_U - x_{tar}}{|\mathbf{X}_U - \mathbf{X}_{tar}|}\right)\delta x_{tar} + \left(\frac{y_U - y_{tar}}{|\mathbf{X}_U - \mathbf{X}_{tar}|}\right)\delta y_{tar} + \left(\frac{z_U - z_{tar}}{|\mathbf{X}_U - \mathbf{X}_{tar}|}\right)\delta z_{tar} \\
&\quad - \delta r_{CL} - r\delta C - v_r
\end{aligned}
\tag{83}
$$

Equation (83) represents the *truth model* description of the range measurement used in the integrated Kalman filter.

The range rate difference measurement is much more complex than the range difference measurement. Equation (81) describes the INS indicated range from the aircraft to the target. In order to provide an INS indicated range rate, a time derivative of Equation (81) is taken:

$$
\dot{r}_{INS_{tar}} = T_{INS_{tar}} \,/\, r_{INS_{tar}} \tag{84}
$$

where

$$
T_{INS_{tar}} = [(x_U - x_{tar})(\dot{x}_U) + (y_U - y_{tar})(\dot{y}_U) + (z_U - z_{tar})(\dot{z}_U)] \tag{85}
$$

A Taylor series expansion of Equation (84), truncated to first order, produces the INS indicated range rate approximation in terms of the error state variables previously defined. The Taylor series expansion of (84) produces:

$$
\begin{aligned}
\dot{r}_{INS_t} &= \dot{r}_{tar} + \left.\frac{\partial \dot{r}_{INS_{tar}}(\mathbf{X}_{tar}, \mathbf{X}_U, \dot{\mathbf{X}}_U)}{\partial \mathbf{X}_t}\right|_{(\mathbf{X}_{tar}, \mathbf{X}_U, \dot{\mathbf{X}}_U)_{nom}} \cdot \delta \mathbf{X}_{tar} \\
&\quad + \left.\frac{\partial \dot{r}_{INS_{tar}}(\mathbf{X}_{tar}, \mathbf{X}_U, \dot{\mathbf{X}}_U)}{\partial \mathbf{X}_U}\right|_{(\mathbf{X}_{tar}, \mathbf{X}_U, \dot{\mathbf{X}}_U)_{nom}} \cdot \delta \mathbf{X}_U \\
&\quad + \left.\frac{\partial \dot{r}_{INS_{tar}}(\mathbf{X}_{tar}, \mathbf{X}_U, \dot{\mathbf{X}}_U)}{\partial \dot{\mathbf{X}}_U}\right|_{(\mathbf{X}_{tar}, \mathbf{X}_U, \dot{\mathbf{X}}_U)_{nom}} \cdot \delta \dot{\mathbf{X}}_U
\end{aligned}
\tag{86}
$$

where the expected $\delta\dot{\mathbf{X}}_{tar}$ term equals zero since the target is not moving (assumption). Substituting Equation (84) into Equation (86), and evaluating all partial derivatives produces the INS calculated range rate from aircraft to target:

$$\begin{aligned}
\dot{r}_{INS_{tar}} = \dot{r}_{tar} &+ [(r_{INS_{tar}}^{-1})(\dot{x}_U) - (r_{INS_{tar}}^{-3/2})(T_{INS_{tar}})(x_U - x_{tar})]\delta x_U \\
&+ [(r_{INS_{tar}}^{-1})(\dot{y}_U) - (r_{INS_{tar}}^{-3/2})(T_{INS_{tar}})(y_U - y_{tar})]\delta y_U \\
&+ [(r_{INS_{tar}}^{-1})(\dot{z}_U) - (r_{INS_{tar}}^{-3/2})(T_{INS_{tar}})(z_U - z_{tar})]\delta z_U \\
&+ [(r_{INS_{tar}}^{-1})(x_U - x_{tar})]\delta\ddot{x}_U \\
&+ [(r_{INS_{tar}}^{-1})(x_U - x_{tar})]\delta\ddot{y}_U \\
&+ [(r_{INS_{tar}}^{-1})(x_U - x_{tar})]\delta\ddot{z}_U \\
&- [(r_{INS_{tar}}^{-1})(\dot{x}_U) - (r_{INS_{tar}}^{-3/2})(T_{INS_{tar}})(x_U - x_{tar})]\delta x_{tar} \\
&- [(r_{INS_{tar}}^{-1})(\dot{y}_U) - (r_{INS_{tar}}^{-3/2})(T_{INS_{tar}})(y_U - y_{tar})]\delta y_{tar} \\
&- [(r_{INS_{tar}}^{-1})(\dot{z}_U) - (r_{INS_{tar}}^{-3/2})(T_{INS_{tar}})(z_U - z_{tar})]\delta z_{tar}
\end{aligned} \tag{87}$$

Using the difference measurement technique, Equation (87) is subtracted from Equation (80) producing the following *truth model* SAR range rate difference measurement used in the integrated Kalman filter:

$$\begin{aligned}
\delta z_{SAR_{\dot{r}}} &= \dot{r}_{INS_{tar}} - \dot{r}_{SAR} \\
&= \dot{r}_{tar} + [(r_{INS_{tar}}^{-1})(\dot{x}_U) - (r_{INS_{tar}}^{-3/2})(T_{INS_{tar}})(x_U - x_{tar})]\delta x_U \\
&\quad + [(r_{INS_{tar}}^{-1})(\dot{y}_U) - (r_{INS_{tar}}^{-3/2})(T_{INS_{tar}})(y_U - y_{tar})]\delta y_U \\
&\quad + [(r_{INS_{tar}}^{-1})(\dot{z}_U) - (r_{INS_{tar}}^{-3/2})(T_{INS_{tar}})(z_U - z_{tar})]\delta z_U \\
&\quad + [(r_{INS_{tar}}^{-1})(x_U - x_{tar})]\delta\ddot{x}_U \\
&\quad + [(r_{INS_{tar}}^{-1})(x_U - x_{tar})]\delta\ddot{y}_U \\
&\quad + [(r_{INS_{tar}}^{-1})(x_U - x_{tar})]\delta\ddot{z}_U \\
&\quad - [(r_{INS_{tar}}^{-1})(\dot{x}_U) - (r_{INS_{tar}}^{-3/2})(T_{INS_{tar}})(x_U - x_{tar})]\delta x_{tar} \\
&\quad - [(r_{INS_{tar}}^{-1})(\dot{y}_U) - (r_{INS_{tar}}^{-3/2})(T_{INS_{tar}})(y_U - y_{tar})]\delta y_{tar} \\
&\quad - [(r_{INS_{tar}}^{-1})(\dot{z}_U) - (r_{INS_{tar}}^{-3/2})(T_{INS_{tar}})(z_U - z_{tar})]\delta z_{tar} \\
&\quad - \delta r_D - \dot{r}\delta C - \dot{r}\delta F - v_{\dot{r}}
\end{aligned} \tag{88}$$

Noise variance values for the SAR range and range rate measurements are found in Appendix B, Table 32. Note the inclusion of velocity errors in Equation (88), this correlates to the previous discussion that aircraft velocity errors contribute to much of the targeting error in the range rate measurement. These values are provided by Layne, and represent a SAR radar sensor's truth and filter model parameters with the parameters shown in Table 1 [11, 32].

Table 1. SAR Performance Characteristics

SAR Characteristic	Filter Model	Truth Model
Range Resolution	15.0	5.0
Azimuth Resolution	15.0	5.0
Pulse Frequency	10.0E9	10.0E9
Pulse Propagation Speed	984.0E6	984.0E6
Range Time Delay	0.002	0.001
Range Rate Time Delay	0.002	0.001

Layne provides a complete relationship between these 6 parameters and the amount of measurement noise in the SAR range and range rate measurements in reference [11] and [32]. Using these values, the SAR measurement noises shown in Table 32 were calculated. The filter model SAR characteristics are arbitrarily higher to provide conservative estimates of all SAR error states.

3.7. Integrated System Models

Sections 3.3 through 3.6 defined the truth models for each specific sensor package used in this research. The next section will define the method in which these models will be augmented into a single Kalman filter form suitable for simulation in MSOFE. The reduction of each sensor's truth model into an integrated filter model will also be discussed in the following paragraphs.

3.7.1. Integrated Truth Model

Equation (89) describes the augmentation of each sensor truth model into a single Kalman filter dynamics equation:

$$\begin{bmatrix} \delta\dot{\mathbf{x}}_{INS} \\ \delta\dot{\mathbf{x}}_{GPS} \\ \delta\dot{\mathbf{x}}_{SAR} \end{bmatrix} = \begin{bmatrix} \mathbf{F}_{INS}(t) & 0 & 0 \\ 0 & \mathbf{F}_{GPS}(t) & 0 \\ 0 & 0 & \mathbf{F}_{SAR}(t) \end{bmatrix} \begin{bmatrix} \delta\mathbf{x}_{INS} \\ \delta\mathbf{x}_{GPS} \\ \delta\mathbf{x}_{SAR} \end{bmatrix} + \begin{bmatrix} \mathbf{w}_{INS} \\ \mathbf{w}_{GPS} \\ \mathbf{w}_{SAR} \end{bmatrix} \tag{89}$$

where $\delta\boldsymbol{x}_{INS}$ and $\boldsymbol{F}_{INS}$ are defined in Equation (40), $\delta\boldsymbol{x}_{GPS}$ and $\boldsymbol{F}_{GPS}$ are defined in Equations (44), (46), (55), and (64) (depending upon GPS type), and $\delta\boldsymbol{x}_{SAR}$ and $\boldsymbol{F}_{SAR}$ are defined in Equation (78). Table 2 describes the total amount of truth model states used in this research, depending upon GPS type. Case 1 refers to stand-alone GPS, Case 2 refers to differential GPS, and Case 3 refers to carrier phase differential GPS.

Table 2. Integrated Truth Model States

	Case 1	**Case 2**	**Case 3**
INS	39	39	39
GPS	30	22	24
SAR	6	6	6
Total States:	75	67	69

Notice that the SAR model does not include the seven states referenced in Section 3.6. During the actual simulation described in Chapter 4, the addition of the frequency error state, δF, caused large biases in each of the remaining six states. Therefore, as a final simulation result, the frequency error state was removed and compensated for by creating a white noise component in the radar wave propagation speed error, δC. Section 4.4 will discuss the details regarding tuning compensation for the bias effects caused by the frequency error.

Appendix B contains a complete list of each sensor's truth model. Equation (89) is used as the truth model for the integrated Kalman filter dynamics model in the MSOFE

simulation software. The filter model, whose development follows, will be compared and tuned against this truth model to provide adequate performance in the presence of reduced state complexity.

3.7.2. Integrated Filter Model

The integrated filter model is represented in the same manner as the truth model shown in Equation (89). However, since the actual implementation of a Kalman filter truth model onboard an aircraft would take a tremendous amount of computational capability a filter model is used to represent the truth model using less states. The next few paragraphs will define the truth model state reduction for each sensor. The final result is a reduced order filter model that is more suited for online application of a Kalman filter onboard an aircraft. A breakdown of the filter dynamics model across each sensor is available in Appendix B. Table 3 describes the number of states used in the integrated filter model for each GPS type.

Table 3. Integrated Filter Model States

	Case 1	**Case 2**	**Case 3**
INS	11	11	11
GPS	2	2	4
SAR	5	5	5
Total States:	18	18	20

The original INS truth model contains 93 error states. In Section 3.3 the 93 states were reduced to 41. The filter model used in this research follows that of [1-4, 8, 9, 20-24] by using the first 11 states. These 11-states comprise aircraft position error, velocity error, misalignment errors, and barometric altimeter errors. Any further reduction of states from the 11-state filter model creates instabilities in the Kalman filter [8].

The stand-alone GPS truth model contains 30 error states. However, the most dominant states in the truth model are the user clock bias and drift states. These two states contribute an order of magnitude more error to the GPS pseudorange equation than the other error sources combined. Therefore, as mentioned in [8], the stand-alone GPS filter model can be reduced to just the user clock bias and drift states. The differential GPS filter model also contains only these two states. As explained in Section 3.5.3, the CPGPS model contains a carrier-phase ambiguity state (per satellite) that is not necessary in the SGPS and DGPS models. Previous research has shown that the a CPGPS filter model must include these states to remain stable across the entire flight profile [20, 28, 30]. Therefore, the CPGPS filter contains an additional four states not included in the SGPS and DGPS models. However, with the double differencing technique applied to the CPGPS model, the user clock bias and clock bias drift states are removed.

According to Maybeck [4], the filter may be unable to retain observability of the multiple random bias states in the SAR error model. Therefore, the 6-state truth model described in Section 3.7.1 is condensed into a 5-state filter model, one state for range bias, one state for range rate bias, and three states for SAR target position errors. This technique will preserve the observability of each state while the state reduction can be tuned through the techniques described in Section 2.2.5.2. Even with the state reduction mentioned, there are still additional random bias states remaining in the filter model. Further reduction of these states is necessary when developing a flight worthy Kalman filter for implementation and flight test.

3.7.3. Integrated System/Filter Measurement Model

The measurement models used in this research extend to each sensor measurement input into the integrated Kalman filter. There are four types of measurement available to the filter: barometric altimeter, satellite pseudoranges, SAR range, and SAR range rate measurements. The baro and satellite measurements are available at 1Hz rates. The SAR measurements are available twice during a specific portion of the flight profile. This simulates the ability of a SAR to make a target range/range rate measurement, and then be retasked for a second set of measurements during the reconnaissance mission. Two measurements are typical for a reconnaissance mission; however for a fighter targeting mission, several hundred measurements at a very high rate may be desirable. One change occurs in between the GPS simulations, that of the double difference in the CPGPS measurement model. This model produces only 3 measurements (see Section 3.5.3) as opposed to the four pseudorange measurements in the SGPS and DGPS cases.

3.8. Simulation Software

Several software packages are used in this research. Each package is vital to the complete Kalman filter simulation. MSOFE provides the simulation code for evaluating a Kalman filter design against a truth model [6]. MPLOT produces complete data sets and Monte Carlo statistics of user-defined variables as generated by MSOFE [6]. PROFGEN compiles the flight profiles used in MSOFE to control the simulation [6]. Together, these three software programs comprise the "*AVLAB Toolbox*" which defines the flight profile, runs the Kalman filter simulation, and generates the complete data output [6]. MATLAB is then used to analyze, plot, and display all results [31].

3.8.1. MSOFE

As previously mentioned, MSOFE is a multimode simulation tool for designing systems that employ Kalman filtering techniques [6]. MSOFE has been used in several research projects at AFIT [1-3, 8, 11, 19-21, 23-25, 27-30]. There are two core software modules used in MSOFE: core code (CSOFE) and user code (USOFE). The CSOFE code contains 63 routines including: Kalman filter simulation, Runge-Kutta integration, measurement processing and updating, data collection, etc. The USOFE code contains a core of 14 routines which can be modified to suit the user. The main routines include: truth and filter dynamics structure, truth and filter measurement structure, data input/output formation, and system noise addition. The USOFE/CSOFE structure provides MSOFE with the ability to simulate different types of Kalman filter models while maintaining a core set of routines that are unchanged. In addition to its flexibility, MSOFE is coded in double-precision and maintains numerical precision by implementing the U-D factorization technique [5, 6].

Two main functions of MSOFE, beyond Kalman filter simulation, are covariance and Monte Carlo simulation. Monte Carlo simulation allows the user to generate multiple time histories of all truth and filter model states, with random sampling between runs. Monte Carlo simulations provide meaningful statistics of each state across the total amount of Monte Carlo runs. Covariance simulation provides time histories of the covariances of the truth and filter model states. When applied, the covariance simulation runs once (compared to multiple Monte Carlo runs) but only operates on linear systems. In addition, the Monte Carlo and covariance simulations provide statistics on the filter estimation errors.

MSOFE requires detailed input and include files which govern problem-specific variables needed for proper simulation. One such include file is the "*sizes*" file. This file controls the size of the filter and truth models, number of flight profile variables, and the amount of measurements to be processed. The input file controls the amount of Monte Carlo runs, the initial covariances of the truth and filter models, all adjustable noise and gain parameters, measurement properties, MSOFE control switches, and any other user defined variables. Proper use of the input file can save the MSOFE user time and effort by dropping the need to compile and link the USOFE/CSOFE code. For example, filter tuning variables, changed frequently, are located in the input file so when they are varied the USOFE code does not require recompilation. However, any changes in the USOFE code or include files requires compilation and linking.

3.8.2. MPLOT

MPLOT is another program in the "*AVLAB Toolbox*" compatible with MSOFE [6]. The user, through the USOFE code and MPLOT input file, determines which variables (filter and truth states, covariances, etc.) to analyze. After MSOFE has run, two files are created, "*CTOM*" and "*DTOM*". MPLOT processes these two files into user defined data files. MPLOT allows the user to generate single Monte Carlo run data or state variable statistics across multiple Monte Carlo runs. MPLOT can also generate flight profile information such as aircraft position, velocity, and attitude across the entire flight profile. MPLOT generated data files are ASCII files which can be used with several plotting packages like Microsoft Excel and MATLAB.

3.8.3. PROFGEN

The final software package integrated with the "*AVLAB Toolbox*" is PROFGEN [6]. PROFGEN provides position, velocity, acceleration, attitude, and attitude rates for a simulated aircraft moving over the earth. Based on user-generated parameters, the PROFGEN flight profile is broken up into several different segments describing the following maneuvers [3, 6]:

a) vertical turns (pitch up or down)
b) horizontal turns (yaw left or right)
c) sinusoidal jink heading changes (oscillates left and right)
d) straight and level flights (great circle or rhumb line path)

These maneuvers are applied to a simulated point mass aircraft and processed by PROFGEN into an output file called "*fly_out*". MSOFE uses this file as the basis for all aircraft position, velocity, attitude, etc. truth data. Truth model and filter model error characteristics are generated by MSOFE with respect to the aircraft parameters provided by the "*fly_out*" file. Section 4.2 contains a description of the U-2 reconnaissance mission flight generated through PROFGEN for this research.

PROFGEN uses standard reference systems and earth models for its calculations [3, 6]. Position is provided in geographic latitude, longitude, and altitude (Section 2.4.4). Velocity is referenced in the local-navigation frame (Section 2.4.2). Accelerations are calculated as the velocity rate plus Coriolis effects and gravity. Attitude, roll, pitch, and yaw, is represented in the body frame (Section 2.4.4).

3.8.4. GPSADD

GPSADD is a small Fortran-90 program used to generate GPS satellite ECEF positions from actual ephemeris data provided by the National Geodetic Office. Gray was the first AFIT student to use true satellite ephemeris information in MSOFE simulations [3]. The ephemeris data provides satellite position information from a random day, 21 May 1994, and represents the best four satellites available with regard to GDOP and the "*Tanker3*" flight profile created by Gray. All attempts were made in this research to map the U-2 flight profile to the aircraft position generated in the "*Tanker3*" profile to facilitate use of the existing GPS true ephemeris data used by Gray. However, the satellite selection process used by Gray may lead to slightly different optimal satellite choices with regards to the U-2 flight profile.

GPSADD appends the satellite ephemeris information to the PROFGEN "*fly_out*" file. GPSADD also transforms the ephemeris data into the ECEF coordinate system and changes the units from meters to feet. The satellite position is provided to MSOFE through the "*TRJSYS*" USOFE routine and is used extensively to provide the true range between the aircraft and the satellite for all GPS measurements.

3.9. Summary

This chapter discussed the specific models used to simulate the integrated INS/GPS/SAR navigation and targeting system. INS and truth and filter models are based on previous AFIT research and have been validated extensively [1-3, 8, 11, 19-21, 23-25, 27-30]. Three different types of GPS models, SGPS, DGPS, and CPGPS, were presented and described in detail. All three are the result of previous AFIT research [1-

3, 8, 11, 19-21, 23-25, 27-30]. The SAR model was adopted from Layne and modified slightly to perform adequately during simulations [11, 32]. The modeling software was also presented including: Kalman filter simulation, Monte Carlo statistic calculation, flight profile generation, and real world GPS ephemeris data manipulation. Chapter 4 will present the results of the INS/GPS/SAR integration study.

4. Simulation Results

4.1. Overview

This chapter presents the results and analysis of the INS/GPS/SAR integration system simulated in MSOFE. The first section covers the newly generated U-2 Flight Profile created in PROFGEN which models a typical U-2 reconnaissance mission. The second section describes the three cases simulated in this research. The fourth section provides an analysis of the integrated INS/GPS/SAR system performance with respect to aircraft location and SAR targeting performance. Lastly, the results from each case are summarized into compact, easy to understand tables for easy comparison between cases. The results presented herein represent the best possible tuning within the time limits of this research. Although some plots may show filter computed results that are both conservative and non-conservative, the majority of the filter model states are tuned adequately. Recall, the purpose of this research is to analyze the potential rewards a tightly integrated INS/GPS/SAR model could create, not to design a flight-worthy Kalman filter for immediate flight test.

4.2. U-2 Flight Profile

Previous AFIT research with regards to INS/GPS integration concentrated mainly on validation of truth and filter models and precision aircraft approaches [3, 8, 25]. In both cases, the type of flight profile, except for the landing portion, was not critical to the actual research topic. Therefore, the "*Tanker3*" flight profile mentioned in Section 3.8.3 was sufficient to run numerous research simulations [1-3, 19, 25]. However, the focus of this research was to simulate a typical U-2 reconnaissance mission. A new flight profile was

necessary to accomplish this goal leading to the "*U-2Flight*" flight profile. Figure 12 describes the latitude, longitude, and altitude of the "*U-2Flight*" flight profile. As shown in this figure, the aircraft flies in a "racetrack" pattern, at an altitude of 65000-*ft*, which is typical of U-2 reconnaissance missions. Also shown in the figure is the target location with respect to the aircraft flight path. The target is located at –84.5° longitude, 40.2° latitude on the surface of the earth. Section 3.7.3 states that two SAR target measurements are processed by the Kalman filter. Figure 12 also shows the two measurement locations along with a graphical description of the SAR range measurement. Appendix F contains a complete collection of plots covering the "*U-2Flight*" position, velocity, attitude, and attitude rate charts across the entire flight profile.

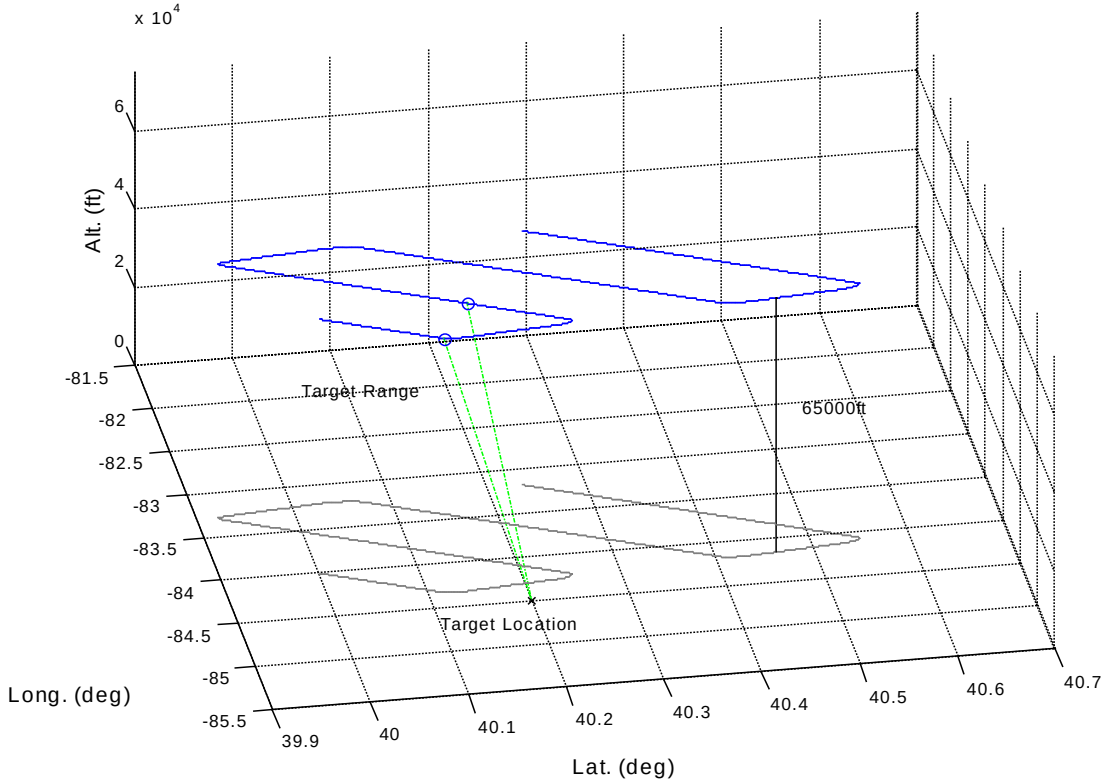

Figure 12. U-2 Flight Profile and Targeting Scenario

The U-2 flight profile is broken up into 10 sections of which 3 sections are repeated two times to generate the racetrack flight path lasting 3700 seconds. The sections of the flight are as follows:

a) 500 second straight and level flight, 65000ft altitude, initial velocity of 200 knots
b) 200 second 90 degree roll left with a gradual acceleration
c) 400 second 90 degree roll left with a gradual acceleration
d) 500 second straight and level flight, gradual deceleration
e) repeat of b), 200 second turn in opposite direction
f) repeat of c), 400 seconds turn in opposite direction
g) repeat of d), 500 seconds
h) repeat of b), 200 seconds
i) repeat of c), 400 seconds
j) repeat of d), 500 seconds

While this flight profile is not a complete U-2 flight from take-off to landing, it suffices for initial targeting performance analysis, since the purpose of this research is to determine the accuracy of SAR targeting with respect to different types of GPS receivers. Therefore, only the first 1200 seconds of the flight profile are discussed in the analysis sections to follow. The first 1200 seconds of the flight profile cover 20 minutes of Kalman filter performance and includes both SAR measurements.

4.3. Case Definition

The following sections define the differences between each case investigated in this research. The cases are defined in accordance with the type of GPS simulated in each integrated INS/GPS/SAR system. The three GPS's simulated are the stand-alone GPS, differential GPS, and carrier-phase GPS. In each case, the INS and SAR models

remained unchanged in order to perform a detailed comparison between the various integrated GPS receiver models. Appendix B contains Table 17, Table 18, and Table 22 which represent the INS and SAR truth model states used in each case. The barometric-altimeter provides altitude measurements to the integrated Kalman filter, while the SAR provides both range and range rate measurements. This is standard across each of the cases. The results presented in this chapter represent the output of a 50 Monte Carlo run MSOFE simulation.

4.3.1. Case 1, Stand-Alone GPS

The first INS/GPS/SAR integrated system simulated a stand-alone, four-channel SGPS receiver. The SGPS model entails a 30-state truth model and 2-state filter model as described in Section 3.5.1. Previous research with the SGPS model has shown aircraft position error of approximately 19ft RMS; this research was expected to provide similar accuracy [3, 8, 27, 29]. This model was integrated with the INS and SAR models using the method described in Section 3.7. Appendix B contains Table 19 and Table 23 which describe the 30-state SGPS model and the 18-state filter model, respectively, used in the integrated INS/GPS/SAR model for Case 1.

4.3.2. Case 2, Differential GPS

The next INS/GPS/SAR integrated system simulated a differential GPS receiver. The DGPS model entails a 22-state truth model and 2-state filter model as described in Section 3.5.2. This model is similar to the SGPS model with the reduction of 2-states per satellite vehicle representing the differential correction. Previous research with the

DGPS model has shown aircraft position error of approximately 5ft RMS; this research was expected to provide similar accuracy [1, 2, 25]. This model was also integrated with the INS and SAR models using the methods described in Section 3.7. Appendix B contains Table 20 and Table 23 which describe the 22-state DGPS model and the 18-state filter model, respectively, used in the integrated INS/GPS/SAR model for Case 2.

4.3.3. Case 3, Carrier-Phase GPS

The last INS/GPS/SAR integrated system simulated a carrier-phase differential GPS implementation. The CPGPS model entails a 26-state truth model and 6-state filter model as described in Section 3.5.3. This model parallels the DGPS model and includes four carrier-phase ambiguity errors, one for each satellite in the simulation. Previous research with the CPGPS model has shown aircraft position error of approximately 6-*ft* RMS; this research was expected to provide similar accuracy [20, 28, 30]. This model was also integrated with the INS and SAR models using the methods described in Section 3.7. Appendix B contains Table 21 and Table 23 which describe the 4-state CPGPS ambiguity error and the 22-state filter model, respectively, used in the integrated INS/GPS/SAR model for Case 3.

4.4. Simulation Results

MSOFE simulation results are presented on a case-by-case basis. Starting with the SGPS, the aircraft location errors and target position accuracy of the integrated INS/GPS/SAR system are analyzed. The desired end result of this research is to determine the impacts and effects different GPS implementations can have on SAR

reconnaissance targeting. Therefore, the correlation between aircraft location accuracy and target position accuracy are analyzed closely. The results from each case are compared to determine the best results theoretically obtainable through this research.

Appendix C through Appendix E provide a complete graphical representation of each filter model state per case. Each figure in the appendices contains five traces using the legend shown in Figure 13.

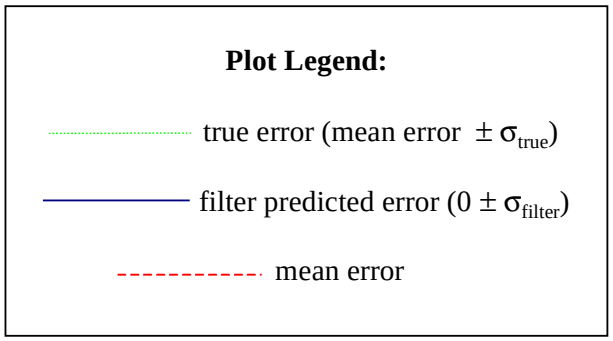

Figure 13. Plot Legend

The mean error trace is defined by the following equation [3, 4]:

$$\hat{M}_e(t_i) = \frac{1}{N}\sum_{j=1}^{N} e_j(t_i) = \frac{1}{N}\sum_{j=1}^{N} \left(\hat{x}_{Filter\,j}(t_i) - \hat{x}_{True\,j}(t_i)\right) \tag{90}$$

where $\hat{x}_{Filter/True_j}(t_i)$ represents the filter computed and truth model error-state estimates, at time t_i, for sample run j. N is the total number of Monte Carlo runs (50) for the simulation. The pair of true error ± sigma traces are the sum of the previously defined mean error and the true standard deviation. The sigma values, used in these traces, averaged across every Monte Carlo run are defined by [3, 4]:

$$\sigma_{true}(t_i) = \sqrt{P_e(t_i)} = \sqrt{\frac{1}{N-1}\sum_{j=1}^{N} e_j^2(t_i) - \frac{N}{N-1}\hat{M}_e^2(t_i)} \tag{91}$$

where $P_e(t_i)$ is the true error sample variance at time t_i. The final pair of traces, filter predicted error, is the filter computed standard deviations displaced about zero because the filter believes that it is producing zero mean errors [3, 4].

4.4.1. Case 1

The "*U-2Flight*" flight profile was used to provide truth data for simulation of the integrated INS/GPS/SAR system with the SGPS. With respect to previous research using the SGPS model, the integrated system operated exactly as expected with only minor deviations. The target accuracy performance in this case will be used as a benchmark to determine how much better the DGPS and CPGPS models are at producing higher accuracy target geolocation.

4.4.1.1. Aircraft Position/Velocity/Attitude Accuracy

Overall SGPS results for aircraft errors are provided in Table 4. Figure 14 contains a plot of the aircraft latitude, longitude and altitude error estimates. The average position errors were: 8.00-*ft* for latitude, 6.17-*ft* for longitude, and 14.39-*ft* for altitude. The RMS value of aircraft position error was 17.59-*ft*, compared to the 19-*ft* average RMS error found in previous SGPS research [3, 8, 27, 29].

Table 4. SGPS Aircraft Errors

	Latitude	**Longitude**	**Altitude**
Ave. Position (*ft*)	8.00	6.17	14.39
	North	**East**	**Down**
Ave. Velocity (*ft/s*)	0.18	0.25	0.53
	North	**East**	**Down**
Ave. Attitude (*rad*)	2.27E-5	5.74E-4	1.62E-5

The removal of the CIRIS transponder model from the INS/GPS integration models used by several other research projects led to a slightly better RMS position error in this research [3, 8, 27, 29]. CIRIS is a reference system used by the USAF to test GPS system performance [3, 8, 27, 29]. The transponders provided position estimates that were not as accurate as the SAR model used here, creating a slightly less accurate total aircraft position solution.

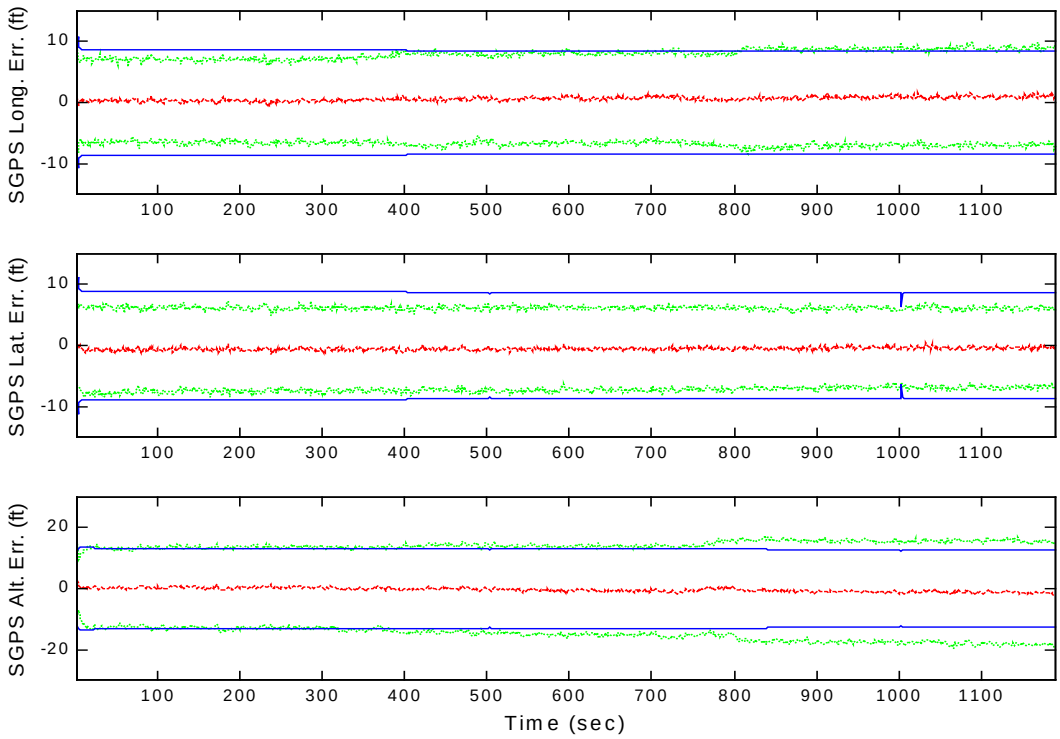

Figure 14. SGPS Aircraft Position Error Estimates

There was some initial concern regarding the impact of SAR model measurements on aircraft position and velocity errors. Equations (83) and (88) from Section 3.6.2 show that the range measurement is a function of aircraft position errors and the range rate measurement is a function of both aircraft position and velocity errors. Figure 14 shows that any concern was unwarranted. In fact, the second SAR measurements, at 1000

seconds, actually decreased the filter computed covariance in the latitude and altitude error estimates. However, the dominate error source with respect to those errors is the accuracy and type of GPS model, causing the filter computed covariances to propagate back to their previous levels within three time samples. On the velocity side, the SAR range rate measurement significantly affected the north and down velocity error estimates, Appendix C, Figure 25. The north velocity error estimate was decreased by 21% after the SAR range rate measurement at 1000 seconds. The east and down velocity estimates were also affected, but not as drastically as the north velocity. In addition, there was a minor improvement in the filter computed covariance of the attitude angles, Appendix C, Figure 26.

There was one minor anomaly with the SGPS integrated system. Figure 15 shows the SGPS user clock bias error. At approximately 800 seconds, there is a sharp increase in the amount of true covariance in the user clock bias. This effect also correlates to a 15% increase in the aircraft altitude error after 800 seconds (Figure 14). The mean true error of the user clock bias is also drifting in the negative direction after 375 seconds. This phenomenon is not seen in previous SGPS research at AFIT, nor in the DGPS or CPGPS results to follow [3, 8, 27, 29]. Typically, an increase in user clock bias error magnitude occurs when the receiver satellite constellation is changed [12]; however, there was not a constellation change during the first 2000 seconds of the flight profile. Furthermore, since the filter covariance does not reflect the same anomaly as the true error, the problem must be an anomaly in the SGPS truth model. Several steps were taken to fix this problem including running the filter without the SAR model, tuning the GPS filter measurement and process noise, and truth model state reduction. Each of these methods

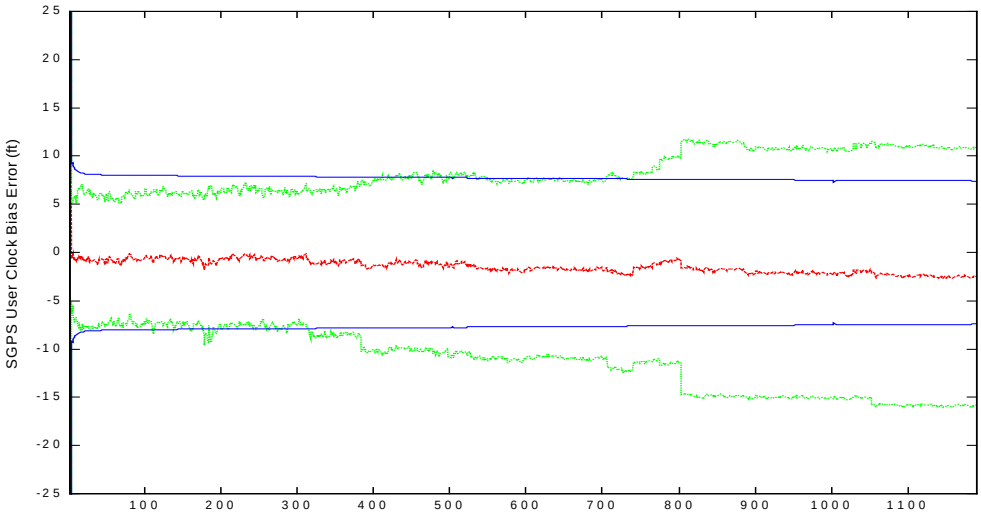

Figure 15. SGPS User Clock Bias Error Estimate

failed to correct both the true error drift and the increase in true covariance. This anomaly is under continuing investigation.

4.4.1.2. Target Position Accuracy

Target accuracy results for the SGPS case can be found in Table 5. Figure 16 contains a plot of the SGPS integrated system target position accuracy. Using an initial position covariance of 100-*ft* per channel, the final target position accuracy after two measurements dropped from 17.43-*ft* RMS to 15.14-*ft* RMS. Figure 16 clearly shows how the SAR range and range rate measurements decrease the amount of error in each target position channel. The 2.30-*ft* drop after the second measurement relates to

Table 5. SGPS Targeting Errors

	X-Position	Y-Position	Z-Position
Initial Error (*ft*)	9.74	11.25	9.09
Final Error (*ft*)	8.30	10.82	6.57
Percent Decrease	14.78%	3.80%	27.71%

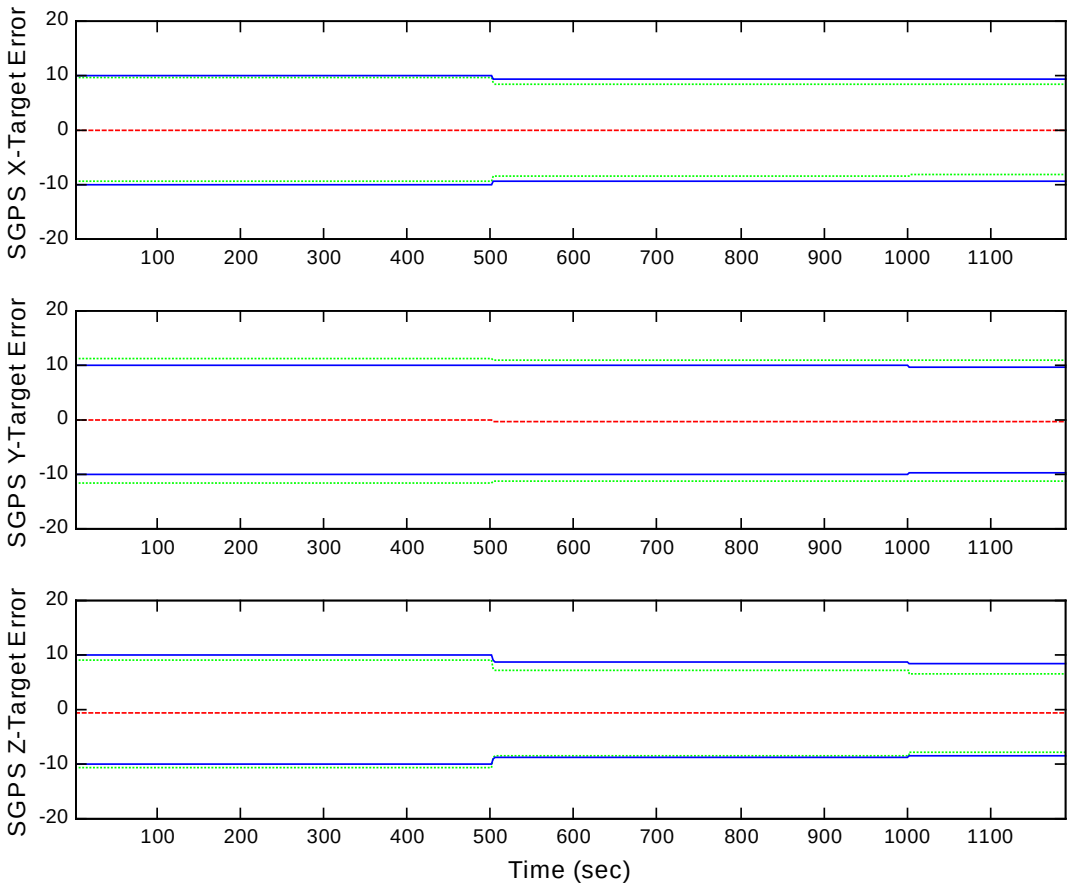

Figure 16. SGPS Target Position Accuracy

an increase in targeting accuracy of 13.22%. The Z-position channel was affected the most with a targeting accuracy increase of 27.71%. The other two channels were affected with accuracy increases of 14.78% for the X-position and only 3.80% for the Y-position.

Without question a higher resolution SAR sensor should provide better target position accuracy. As these simulation results indicate, the addition of SAR measurements into an integrated navigation filter decreases the errors in aircraft position and velocity and target geolocation. The addition of the measurements into the integrated INS/GPS Kalman filter provided a 13.21% decrease in target geolocation error. However, without a another simulation using a different GPS model, it is impossible to determine if this

decrease is due to SAR accuracy or aircraft location accuracy. That is why the next two cases will use the same SAR model as the SGPS case. This way, any new increase in target geolocation accuracy can be attributed to the more accurate GPS receiver simulation which is the only change across cases.

4.4.2. Case 2

The "*U-2Flight*" flight profile was again used to provide truth data for simulation of the integrated INS/GPS/SAR system, this time using a DGPS receiver simulation. With respect to previous research using the DGPS model, the integrated system operated slightly better than expected. SAR targeting performance in this case was very good with better results than those shown in Case 1. In addition, the DGPS user clock bias state estimation performs extremely well without the anomaly seen in the SGPS user clock bias state.

4.4.2.1. Aircraft Position/Velocity/Attitude Accuracy

Overall DGPS results for aircraft errors are provided in Table 6. Figure 17 contains a plot of the latitude, longitude, and altitude errors using the DGPS integrated system. The INS and SAR models remained the same from Case 1. Comparing Figure 17 to Figure 16 (note change in y-axis scale) shows that the DGPS receiver has tightened up the aircraft location errors. In this case, the average position errors were: 1.91-*ft* for latitude, 1.87-*ft* for longitude, and 4.24-*ft* for altitude. The total RMS aircraft position error was 5.01-*ft* which duplicates results of previous research [25].

Table 6. DGPS Aircraft Errors

	Latitude	Longitude	Altitude
Ave. Position (*ft*)	1.91	1.87	4.24
	North	**East**	**Down**
Ave. Velocity (*ft/s*)	0.13	0.12	0.13
	North	**East**	**Down**
Ave. Attitude (*rad*)	1.98E-5	3.86E-4	1.58E-5

The SAR measurements at 500 and 1000 seconds do not affect the position and velocity states in this simulation as in Case 1. The aircraft latitude and altitude errors indicate less than a 1% decrease in filter computed covariance over three seconds. Velocity errors, Appendix D, Figure 32 are barely affected by the SAR range rate measurements at the 1000 second point.

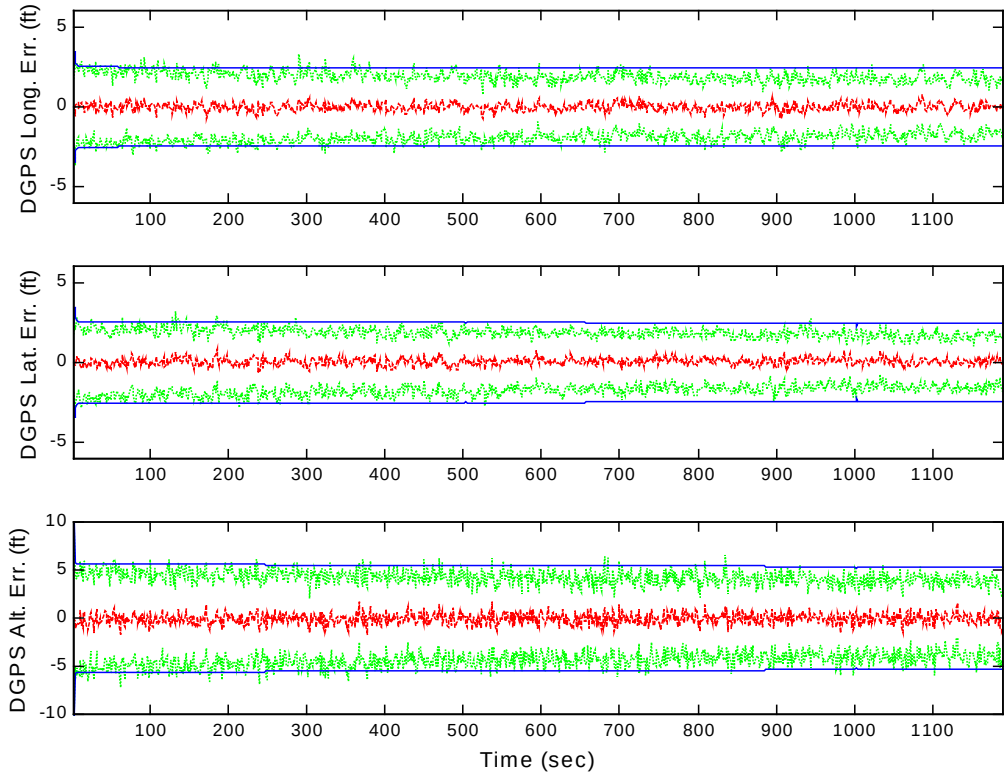

Figure 17. DGPS Aircraft Position Error Estimates

4.4.2.2. Target Position Accuracy

Target accuracy results for the DGPS case can be found in Table 7. Figure 18 contains a plot of the DGPS integrated system target position accuracy. Using the same SAR model as Case 1, the DGPS target position accuracy decreases from a pre-measurement RMS value of 16.30-*ft* to a post-measurement 12.92-*ft* level. The 3.38-*ft* decrease in error results in a 20.78% increase in RMS target geolocation accuracy. The X- and Z-position channels were affected the most with a targeting accuracy increase of 20.57% and 36.5%, respectively. The Y-position channel accuracy was increased by 10.76%.

Table 7. DGPS Targeting Errors

	X-Position	**Y-Position**	**Z-Position**
Initial Error (*ft*)	9.44	10.00	8.75
Final Error (*ft*)	7.50	8.92	5.56
Percent Decrease	20.57%	10.76%	36.50%

The DGPS integrated system provides very accurate aircraft position and velocity estimates. The SAR measurement difference equations, Equations (83) and (88), show a direct relationship between the measurements and aircraft location errors. If the aircraft location errors are known very accurately, the SAR measurements will produce a greater affect on the target position error states. This effect is shown in Figure 18 by the fact that the target geolocation accuracy is much better than that shown in the SGPS case, Figure 16. Since the SAR model and its performance remained the same from Case 1 to Case 2, the resulting increase in targeting accuracy is attributable to the smaller aircraft position errors.

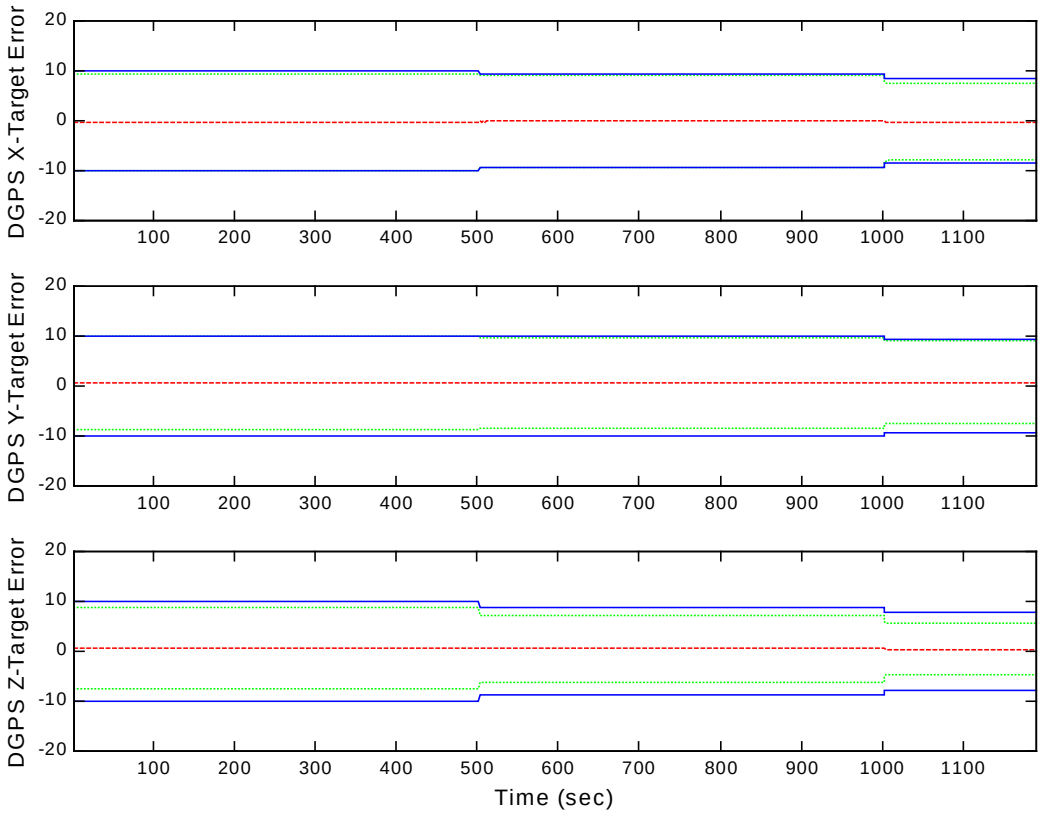

Figure 18. DGPS Target Position Accuracy

4.4.3. Case 3

The "*U-2Flight*" flight profile was last used to provide truth data for simulation of the integrated INS/GPS/SAR system, this time using the CPGPS receiver simulation. With respect to previous research using the CPGPS model, the integrated system also operated better than expected, like the DGPS model. SAR targeting performance in this case was very good with better results than those shown in Case 1 and Case 2. Much like the DGPS, the CPGPS user clock bias state performed as expected. The addition of the four integer ambiguity states performed as expected and represent the error caused by the unknown integer ambiguities in the CPGPS double difference measurements.

4.4.3.1. Aircraft Position/Velocity/Attitude Accuracy

Overall CPGPS results for aircraft errors are provided in Table 8. Figure 19 contains a plot of the latitude, longitude, and altitude errors using the CPGPS integrated system. The INS and SAR models have remained the same from Cases 1 and 2. Comparing Figure 19 with Figure 17 and Figure 14 shows that the CPGPS receiver has tightened up the aircraft location errors beyond those of the SGPS and DGPS model. In this case, the average position errors were: 2.04-*ft* for latitude, 1.55-*ft* for longitude, and 2.02-*ft* for altitude. The total RMS aircraft position error was 3.26-*ft* which performs slightly better than previous research [20, 28, 30]. Since ground based differential CPGPS receivers can provide highly accurate position solutions, it was expected that the airborne CPGPS model in this research would perform much better than the SGPS model and slightly better than the DGPS model.

Table 8. CPGPS Aircraft Errors

	Latitude	**Longitude**	**Altitude**
Ave. Position (*ft*)	2.04	1.55	2.02
	North	**East**	**Down**
Ave. Velocity (*ft/s*)	0.17	0.18	0.19
	North	**East**	**Down**
Ave. Attitude (*rad*)	1.34E-5	2.41E-4	1.16E-5

The SAR measurements at 500 and 1000 seconds have a minimal impact on the position states in this simulation as in Case 1. The aircraft latitude and altitude errors, much like those in Case 2, show only the slightest effects, less than 1% decrease in filter computed covariance over three seconds. Velocity errors shown in Appendix E, Figure 38 are only slightly affected by the SAR range rate measurements, but not nearly as much

as the 17% accuracy increase seen in the SGPS model. The CPGPS velocity plots closely match the performance of the DGPS velocity plots.

The CPGPS model differs from the DGPS model with the addition of 4-integer ambiguity states in the filter and truth models. Appendix E, Figure 42 shows that the ambiguity state modeling is performed very well and that the tuning values provided by Bohenek and Hansen are applicable to this research [20, 28]. There is a slight bias in each ambiguity state that could potentially disappear with additional tuning attention. Even so, the addition of an integrated SAR model into the CPGPS/INS model did not affect the estimation or performance of the ambiguity states at all.

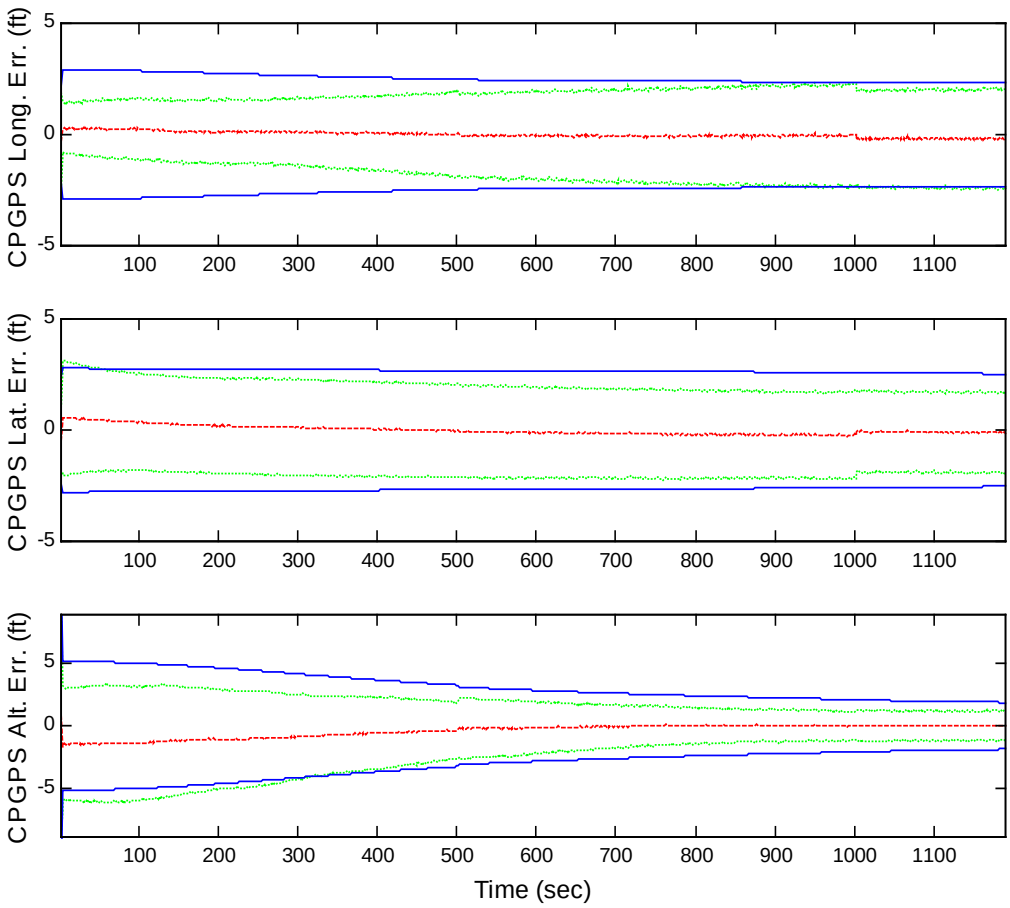

Figure 19. CPGPS Aircraft Position Error Estimates

4.4.3.2. Target Position Accuracy

Target accuracy results for the CPGPS case can be found in Table 9. Figure 20 contains a plot of the CPGPS integrated system target position accuracy. Using the same SAR model as Cases 1 and 2, the CPGPS target position accuracy decreases from a pre-measurement RMS value of 18.81-*ft* to a post-measurement 11.29-*ft* level. The 7.52-*ft* decrease in error results in a 39.96% increase in RMS target geolocation accuracy. The X- and Z-position channels were affected the most with a targeting accuracy increase of 61.74% and 60.27%, respectively. The Y-position channel accuracy was increased by only 21.69%.

Table 9. CPGPS Targeting Errors

	X-Position	**Y-Position**	**Z-Position**
Initial Error (*ft*)	5.37	12.58	12.92
Final Error (*ft*)	2.05	9.85	5.13
Percent Decrease	61.74%	21.69%	60.27%

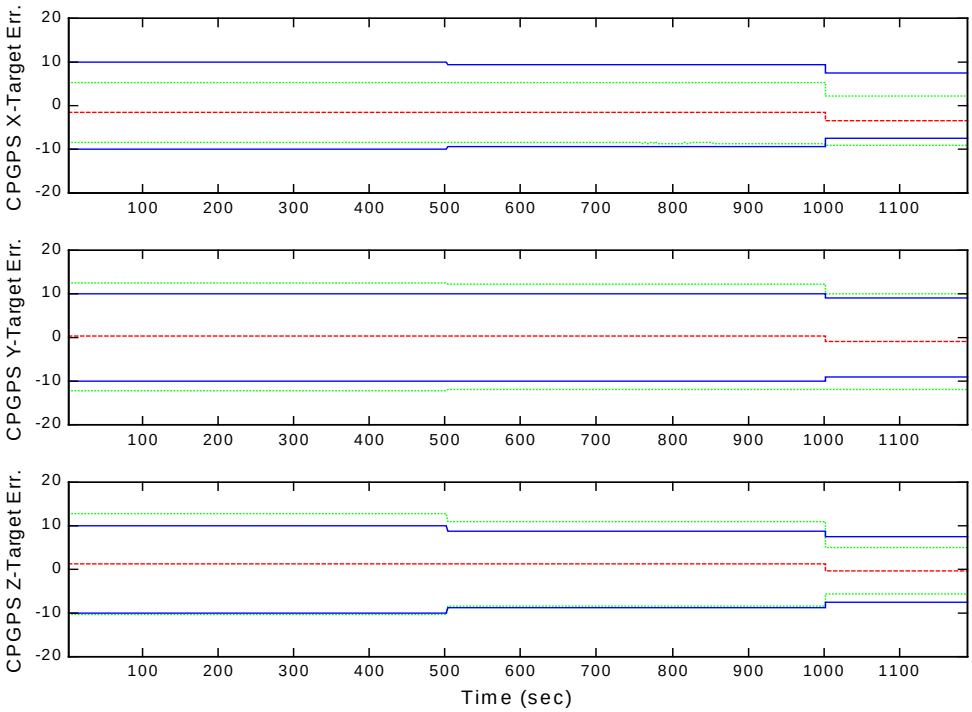

Figure 20. CPGPS Target Position Accuracy

4.4.4. Cross-Case Comparison

An important aspect of this research was to compare the performance of each integrated INS/GPS/SAR case. As a result, the following tables detail the results achieved through this research. Comparison results are broken up into the following categories: percent improvement in target error after two SAR measurements, total aircraft position and velocity errors, percent improvement in target and aircraft location accuracy using the SGPS system as a baseline.

As previously mentioned, the CPGPS provided the best aircraft and target position accuracy. Table 10 shows the results of the aircraft and target position error simulation. The SGPS integrated system provided a 13.20% improvement in target geolocation errors after processing two SAR measurements. The DGPS produced a 20.78% improvement in target geolocation accuracy while the CPGPS provided a 39.96% accuracy improvement. Both the DGPS and CPGPS provided excellent aircraft positions, with RMS errors of 5-*ft* or less. Using Table 10 as a guide, the DGPS provided the most improvement in target location accuracy while also providing a huge increase in aircraft position accuracy compared to the SGPS case. The CPGPS however had the smallest total final target error and aircraft error and therefore performed the best overall.

Table 10. Error Analysis per GPS Type

Errors (*ft*)	**SGPS**	**DGPS**	**CPGPS**
Latitude Error	8.00	1.91	2.03
Longitude Error	6.17	1.87	1.55
Altitude Error	14.39	4.24	2.02
Aircraft Position Error (RMS)	17.59	5.01	3.26
Original Target Error (RMS)	17.44	16.30	18.81
Final Target Error (RMS)	15.14	12.92	11.29

Table 11 displays the aircraft velocity errors for each integrated system. Each system operated very well, with only the SGPS down velocity error exceeding 0.3-*ft/s*. The DGPS showed the best RMS velocity accuracy in two channels. However the CPGPS, with a 0.31-*ft/s* RMS value is greater than the DGPS; virtually indistinguishable in a table but potentially noticeable in a typical 8 hour U-2 reconnaissance mission. Therefore, using the U-2 as a basis for this research, the CPGPS may be the preferred GPS receiver. The addition of velocity aiding through pseudorange rate measurements in the GPS receiver model should produce even better results than those in this research [5].

Table 11. Velocity Error Analysis per GPS Type

Errors (*ft/s*)	SGPS	DGPS	CPGPS
North Velocity Error	0.18	0.13	0.17
East Velocity Error	0.25	0.12	0.18
Down Velocity Error	0.53	0.27	0.19
Aircraft Velocity Error (RMS)	0.61	0.32	0.31

Table 12 contains a comparison between each integrated system. The DGPS provided a 14.66% improvement over the SGPS with respect to post-SAR measurement target geolocation improvement. The CPGPS system provided a 25.43% improvement over the SGPS and 13.26% improvement over the DGPS.

Table 12. Target Geolocation Improvement by GPS Type

Method	Target Error RMS (*ft*)	Improvement over SGPS	Improvement over DGPS
SGPS	15.14	--	--
DGPS	12.92	14.66%	--
CPGPS	11.29	25.43%	13.26%

Table 13 shows the same results with respect to aircraft location. However, in this table, the SGPS aircraft location performance is used as a baseline. The DGPS is 71.52%

more accurate than the SGPS; the CPGPS is 81.47% more accurate than the SGPS. These results show the CPGPS as 9.95% more accurate than the DGPS with respect to the SGPS. Table 12 and Table 13 show that the CPGPS performs the best in both targeting geolocation and aircraft position estimation.

Table 13. Aircraft Location Improvement (SGPS Baseline)

Method	Aircraft Error RMS (*ft*)	Improvement over SGPS	Improvement over DGPS
SGPS	17.59	--	--
DGPS	5.01	71.52%	--
CPGPS	3.26	81.47%	9.95%

4.5. Summary

This chapter presented the theoretical performance results of the GPS/INS/SAR integrated system simulation. The results were broken up into cases representing the three GPS receiver implementations: stand-alone, differential, and carrier-phase differential. Each case was modeled using the same INS and SAR models, with the GPS receiver model as the only change across cases. Therefore, SAR targeting improvements seen from case to case were a direct result of the more accurate GPS receiver. Appendix C through Appendix E contain the collection of figures indicating the performance of each filter model state estimate in the three cases. This chapter also defined the new "*U-2Flight*" flight profile created for these simulations. Appendix F contains a number of plots defining the entire flight profile. Figure 21 shows the bottom-line results of this research. The CPGPS simulation provided the most accurate aircraft and target geolocation estimates. The DGPS was not far behind and actually performed almost exactly like the CPGPS with respect to aircraft velocity errors. Both CPGPS and DGPS

models performed better than the SGPS. These results were expected when compared with previous research using similar models [1-3, 8, 11, 19-21, 23-25, 27-30, 32].

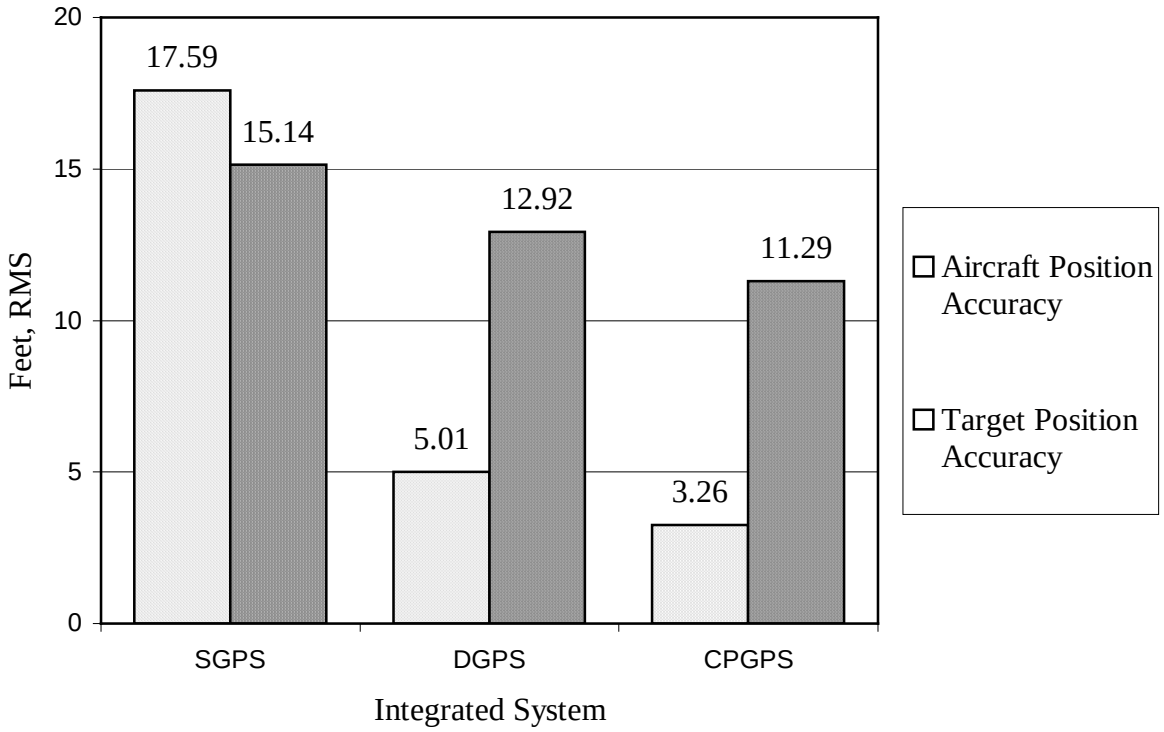

Figure 21. Case-by-Case Integrated System Summary

5. Conclusions

5.1. Overview

This thesis presents the theory, modeling methodology, and results of an integrated INS/GPS/SAR Kalman filter research study. Previous research in this area reflected the performance of an integrated INS/GPS with respect to aircraft position error estimation. Other research included a first cut analysis of the integration of a SAR and other sensors into an integrated INS/GPS [11]. This work represents one of the first known integrations of only SAR range and range rate measurements into an INS/GPS integrated system to provide better accuracy in estimating ground target geolocation errors.

Three different INS/GPS/SAR integrated system models were developed utilizing different GPS models: stand-alone, differential, and carrier-phase differential. The INS was stabilized with a Barometric and Radar altimeter; the SAR provided range and range rates to a known target on a simulated reconnaissance mission. This thesis also generated a new flight profile to represent the unique U-2 reconnaissance collection method. Each of the three integrated systems were implemented using Kalman filtering techniques. Once the models were fully developed, simulations were performed using MSOFE.

5.2. Conclusions

Each of the GPS receivers modeled in this research show increases in the targeting accuracy of the integrated SAR model. The main focus of this research was to determine the effect that aircraft position accuracy has on SAR targeting accuracy. By simulating three different systems and keeping the same SAR model between them, the targeting

improvements can be attributed to the aircraft location accuracy. While the accuracy of the SAR measurements provides the greatest means for targeting improvement, the fusion of highly accurate GPS measurements provides even greater improvement beyond mere modification of the SAR alone. In SAR reconnaissance aircraft, the SAR measurements could be integrated into the navigation Kalman filter to receive this additional benefit.

Previous research by Layne studying integrated SAR and navigation sensors produced very accurate SAR targeting results [11]. However, in Layne's case, there were two additional measurements available, azimuth and elevation angles from aircraft to target. These measurements are not available on a U-2 aircraft and thus were not modeled. Even so, targeting performance in this research was increased significantly using only SAR range and range rate measurements. More importantly, the increase occurred without the benefit of increased SAR resolution.

The GPS receiver models performed as expected throughout the research. The SGPS performed slightly better than expected with aircraft position accuracy near 17ft RMS. The DGPS and CPGPS models performed very well, with position accuracies of 5ft and 3ft, respectively. While CPGPS has the capability of providing fixed integer ambiguity resolution accuracy down to the centimeter level, the simulated CPGPS results were not in the centimeter range. However, this research produced better CPGPS accuracy than that seen in previous research [20, 28, 30].

As previously mentioned, there are multiple random bias states in the filter model (target location, range error, range rate error, etc.). This is a technical drawback to the integrated filter model. While this thesis focused on the true error representation of target errors, any future implementation of the SAR model created in this research must be

analyzed for further reduction of the random bias states. While the results presented herein were stable using all of the random bias states, this does not preclude the fact that problems may still exist within this model. It is important to note that eliminating the unobservable states from the filter model should not affect the overall performance of the system but should provide a more robust model of the integrated system.

The flight profile used in this research was adequate to determine theoretical performance of the integrated INS/GPS/SAR system. The system did not show performance degradation specifically due to the type of flight profile. The positioning of the simulated target within the performance envelope of the SAR model was very important. Several simulation attempts failed because the target was outside of the range capabilities of the SAR model.

Bottom line results in this thesis focused on the targeting benefits of integrating SAR measurements into the INS/GPS navigation Kalman filter. This research has shown that there are performance benefits to be had with proper tight integration of the SAR sensor. Across each GPS receiver model, targeting results were improved, CPGPS by almost 25%, solely through SAR Kalman filter integration. Operating in a stand-alone fashion (i.e. no integration with the INS/GPS) the SAR would not be able to achieve these benefits.

5.3. Recommendations

While the GPS and INS models in this thesis have been used extensively, the SAR model used in this research has only been used on two occasions. This thesis concentrated mainly on the theoretical performance of a tightly integrated navigation

Kalman filter. As such, the SAR model developed by Layne met the task [11,32]. Future research in this area can benefit greatly by advancing the analytical model of the SAR. The 5-state model is lacking many of the errors described by Harger's text [13]. A student well versed in stochastic modeling and synthetic aperture radar could provide a wealth of future SAR integration studies. There are many civilian and military organizations that could benefit greatly from such a model.

The following recommendations are provided to extend this research:

1. Determine the effectiveness of the INS/GPS/SAR model in a real world jamming environment. Many students at AFIT have provided detailed multiple model adaptive estimation techniques to overcome EM jamming [1, 2, 4, 5, 10, 19]. These studies could easily be applied to the SAR targeting scenario.
2. Fuse additional sensors into the INS/GPS/SAR Kalman filter. Layne provides a detailed monopulse radar model in his research [11]. While this study proved that the monopulse radar measurements were not needed for target improvement, this model could provide even better targeting accuracy. Also, the U-2 and other reconnaissance aircraft have many different sensors, including electro-optical and infrared, which could show similar performance increases when integrated into the navigation Kalman filter.
3. Further refine the "*U-2Flight*" flight profile to simulate the actual flight characteristics of the U-2 and/or other reconnaissance aircraft. Unmanned Aerial Vehicles are of particular interest to civilian and military researchers. The "*U-2Flight*" profile was created first and foremost to simulate the flight path of a U-2's

racetrack collection technique. This leaves room for improvement in simulating the U-2 flight characteristics such as maximum speed, attitude rates, etc.

4. The results provided in Appendix C through Appendix E show adequate tuning for almost every state in the Kalman filter model. However, there is room for improvement. Any Kalman filter designed for actual flight test must be tuned for optimal performance.
5. The improvement in targeting accuracy after only two measurements is promising. While this research models the performance of a U-2 on a reconnaissance mission, it could easily be adapted to a fighter/attack scenario. The F-15E, for example, contains a SAR that the pilot can use for targeting ground targets before transitioning to high resolution forward looking infrared (FLIR). Future research could increase the number of SAR measurements processed by the Kalman filter to simulate an F-15E ground attack scenario. In addition, the sensor handoff between SAR and FLIR would also provide a worthwhile simulation study in itself. Integrating the two sensors into the navigation filter could provide better results end-to-end in an F-15E ground attack.
6. New GPS data could provide more realistic data for use in Kalman filter simulations. The existence of high-fidelity GPS simulators and real world GPS data has the potential of limiting the odd effects sometimes witnessed (see Section 4.4.1.1) in the GPS user clock bias estimation.
7. Future carrier-phase differential receiver modeling should analyze the effect of the cycle slip phenomenon. Previous research has been done on this topic, it need only be applied to the INS/GPS/SAR simulation [20, 28, 30]. In particular, a multipath

error model would be very beneficial to properly describe the effects of differentially corrected pseudoranges. Other differencing techniques may also provide added realism to the CPGPS models [35].

8. Loose integration techniques should be simulated. In general, it is much harder to retrofit an aircraft with a brand new, tightly integrated INS/GPS navigation system. Addition of GPS to the U-2 and other aircraft could be implemented in a “loose” fashion. Therefore, simulation of that technique could provide important results for comparison purposes.

Appendix A. Acronym List

AFIT	Air Force Institute of Technology
AFRL	Air Force Research Laboratory
AIMS	Airborne Information and Mapping System
CPGPS	Carrier Phase Global Positioning System
CTOM	Continuous-to-MPLOT
DTOM	Discrete-to-MPLOT
DCM	Direction Cosine Matrix
ECEF	Earth-Centered, Earth-Fixed
EKF	Extended Kalman Filter
EM	Electro-magnetic
FDI	Fault Detection and Isolation
FLIR	Forward-Looking Infrared
SAR	Synthetic Aperture Radar
GPS	Global Positioning System
INS	Inertial Navigation System
MSOFE	Multi-mode Simulation of Optimal Filter Equations
MMAE	Multiple Model Adaptive Estimator
M^3AE	Modified Multiple Model Adaptive Estimator
NRS	Navigation Reference System
PLS	Precision Landing System
PR	Pseudorange
RMS	Root-Mean-Square
SA	Selective Availability
SV	Satellite Vehicle

Appendix B. Model State Definitions and System Matrices

This appendix contains the tabular listing of all truth and filter model error states, the dynamics and noise submatrices from Section 3.3, and tuning parameters achieved during simulation.

B.1. Truth Model Error States

Table 14 through Table 16 contain a complete listing of the 93-state INS truth model. These states comprise a true representation of the errors in a Litton LN-93 strapdown INS [24]. From these 93-states, Negast reduced the order from 93-states to 39-states, including the 2 barometric altimeter states described in Section 3.4. Table 17 and Table 18 contain a complete list of the reduced order 41-state model used to represent the INS in this research.

Table 19 describes the 30-state stand-alone GPS model described in Section 3.5.1, two states for user equipment error and 28 states for each GPS satellite (7 each). Table 20 describes the 22-state differential GPS model described in Section 3.5.2, two states for user equipment error and five states for each GPS satellite (total of 20). Table 21 describes the 4-state carrier phase GPS model described in Section 3.5.3, four states for carrier phase ambiguity errors.

Table 22 describes the 4-state SAR model described in Section 3.6. There are 2 states for range error and 3 states for range rate error (the radar wave propagation speed error affects both range and range rate) in this model.

B.2. Simulation Filter States

The four filter models used in this simulation are listed in this section. Table 23 contains the list of the 18 filter model states used during the stand-alone and differential GPS simulations. Table 24 contains the list of the 20 filter model states used during the carrier phase differential GPS simulation. Note that previous versions of these tables in other theses reference all filter model states back to the 93-state model instead of Negast's reduced order model [1-3, 25].

B.3. Model Dynamics and Noise Matrices [2, 8]

The LN-93 [24] error-state dynamics matrix, **F**, is a 93-by-93 array with many zeros. The non-zero portions of this array, as parsed out in Equation (40) of Section 3.3, are shown in Table 25 through Table 29. Note that only the reduced **F**-matrix is provided here from Negast [8]. For a complete listing of the 93-state dynamics matrix the reader is referred to [1-3, 8, 20-24]. The dynamics model for the three GPS models are contained in Chapter 3.

The Litton LN-93 93-state model also includes a 93-by-93 process noise matrix, **Q**. As shown in Equation (40) again, the $\mathbf{w_1}$ and $\mathbf{w_2}$ are broken into $\mathbf{Q_{11}}$ and $\mathbf{Q_{22}}$ process noise submatrices. Table 30 and Table 31 describe the two **Q**-submatrices, respectively. Process noise matrices for the three GPS models are contained in Chapter 3.

B.4. Tuning Values

This section contains a listing of the tuning values used to tune the reduced order filter models to the truth models. Tuning requirements are defined in Section 2.2.5.2.

Table 33 contains the process noise tuning values used in all three integrated GPS filter models. Each term is a multiplier of the ***Q*** values presented in Table 30 and Table 31, as well as the GPS and SAR descriptions from Chapter 3. Table 32 contains the truth and filter measurement noises for each measurement type: baro-altimeter, SGPS, DGPS, CPGPS, SAR range, and SAR range rate.

Table 14. 93-State INS Truth Model, States 1-31

State Number	State Symbol	State Definition
1	$\delta\theta_x$	X-component of vector angle from true to computer frame
2	$\delta\theta_y$	Y-component of vector angle from true to computer frame
3	$\delta\theta_z$	Z-component of vector angle from true to computer frame
4	ϕ_x	X-component of vector angle from true to platform frame
5	ϕ_y	Y-component of vector angle from true to platform frame
6	ϕ_z	Z-component of vector angle from true to platform frame
7	δV_x	X-component of error in computed velocity
8	δV_y	Y-component of error in computed velocity
9	δV_z	Z-component of error in computed velocity
10	δh	Error in vehicle altitude above reference ellipsoid
11	δh_L	Error in lagged inertial altitude
12	δS_3	Error in vertical channel aiding state
13	δS_4	Error in vertical channel aiding state
14	b_{x_c}	X-component of gyro correlated drift rate
15	b_{y_c}	Y-component of gyro correlated drift rate
16	b_{z_c}	Z-component of gyro correlated drift rate
17	∇_{x_c}	X-component of accelerometer and velocity quantizer correlated noise
18	∇_{y_c}	Y-component of accelerometer and velocity quantizer correlated noise
19	∇_{z_c}	Z-component of accelerometer and velocity quantizer correlated noise
20	δg_x	X-component of gravity vector errors
21	δg_y	Y-component of gravity vector errors
22	δg_z	Z-component of gravity vector errors
23	δh_B	Total baro-altimeter correlated error
24	b_{x_t}	X-component of gyro trend
25	b_{y_t}	Y-component of gyro trend
26	b_{z_t}	Z-component of gyro trend
27	∇_{x_t}	X-component of accelerometer trend
28	∇_{y_t}	Y-component of accelerometer trend
29	∇_{z_t}	Z-component of accelerometer trend
30	b_x	X-component of gyro drift rate repeatability
31	b_y	Y-component of gyro drift rate repeatability

Table 15. 93-State INS Truth Model, States 32-63

State Number	State Symbol	State Definition
32	b_z	Z-component of gyro drift rate repeatability
33	S_{qx}	X-component of gyro scale factor error
34	S_{qy}	Y-component of gyro scale factor error
35	S_{qz}	Z-component of gyro scale factor error
36	χ_1	X gyro misalignment about Y-axis
37	χ_2	Y gyro misalignment about X-axis
38	χ_3	Z gyro misalignment about X-axis
39	ν_1	X gyro misalignment about Z-axis
40	ν_2	Y gyro misalignment about Z-axis
41	ν_3	Z gyro misalignment about Y-axis
42	D_{xxx}	X gyro scale factor nonlinearity
43	D_{yyy}	Y gyro scale factor nonlinearity
44	D_{zzz}	Z gyro scale factor nonlinearity
45	S_{Qb_x}	X gyro scale factor asymmetry error
46	S_{Qb_y}	Y gyro scale factor asymmetry error
47	S_{Qb_z}	Z gyro scale factor asymmetry error
48	∇_{b_x}	X-component of accelerometer bias repeatability
49	∇_{b_y}	Y-component of accelerometer bias repeatability
50	∇_{b_z}	Z-component of accelerometer bias repeatability
51	S_{Ax}	X-component of accelerometer and velocity quantizer scale factor
52	S_{Ay}	Y-component of accelerometer and velocity quantizer scale factor
53	S_{Az}	Z-component of accelerometer and velocity quantizer scale factor
54	S_{QAx}	X-component of accelerometer and velocity quantizer scale factor asymmetry
55	S_{QAy}	Y-component of accelerometer and velocity quantizer scale factor asymmetry
56	S_{QAz}	Z-component of accelerometer and velocity quantizer scale factor asymmetry
57	f_{xx}	Coefficient of error proportional to square of measured acceleration
58	f_{yy}	Coefficient of error proportional to square of measured acceleration
59	f_{zz}	Coefficient of error proportional to square of measured acceleration
60	f_{xy}	Coefficient of error proportional to square of measured acceleration
61	f_{xz}	Coefficient of error proportional to square of measured acceleration
62	f_{yx}	Coefficient of error proportional to square of measured acceleration
63	f_{yz}	Coefficient of error proportional to square of measured acceleration

Table 16. 93-State INS Truth Model, States 64-93

State Number	State Symbol	State Definition
64	f_{zz}	Coefficient of error proportional to square of measured acceleration
65	f_{zy}	Coefficient of error proportional to square of measured acceleration
66	μ_1	X accelerometer misalignment about Z-axis
67	μ_2	Y accelerometer misalignment about Z-axis
68	μ_3	Z accelerometer misalignment about Y-axis
69	σ_3	Z accelerometer misalignment about Y-axis
70	∇_{x_q}	X-component of accelerometer bias thermal transient
71	∇_{y_q}	Y-component of accelerometer bias thermal transient
72	∇_{z_q}	Z-component of accelerometer bias thermal transient
73	b_{x_q}	X-component of initial gyro drift rate bias thermal transient
74	b_{y_q}	Y-component of initial gyro drift rate bias thermal transient
75	b_{z_q}	Z-component of initial gyro drift rate bias thermal transient
76	F_{xyz}	X gyro compliance term
77	F_{xyy}	X gyro compliance term
78	F_{xyx}	X gyro compliance term
79	F_{xzy}	X gyro compliance term
80	F_{xzz}	X gyro compliance term
81	F_{xz}	X gyro compliance term
82	F_{yzx}	Y gyro compliance term
83	F_{yzz}	Y gyro compliance term
84	F_{yzy}	Y gyro compliance term
85	F_{yxz}	Y gyro compliance term
86	F_{yxx}	Y gyro compliance term
87	F_{yxy}	Y gyro compliance term
88	F_{zxy}	Z gyro compliance term
89	F_{zxx}	Z gyro compliance term
90	F_{zxz}	Z gyro compliance term
91	F_{zyx}	Z gyro compliance term
92	F_{zyy}	Z gyro compliance term
93	F_{zyz}	Z gyro compliance term

Table 17. 39-State Reduced Order INS Truth Model, States 1-20

State Number	State Symbol	State Definition
1	$\delta\theta_x$	X-component of vector angle from true to computer frame
2	$\delta\theta_y$	Y-component of vector angle from true to computer frame
3	$\delta\theta_z$	Z-component of vector angle from true to computer frame
4	ϕ_x	X-component of vector angle from true to platform frame
5	ϕ_y	Y-component of vector angle from true to platform frame
6	ϕ_z	Z-component of vector angle from true to platform frame
7	δV_x	X-component of error in computed velocity
8	δV_y	Y-component of error in computed velocity
9	δV_z	Z-component of error in computed velocity
10	δh	Error in vehicle altitude above reference ellipsoid
11	δh_B	Total baro-altimeter correlated error
12	δh_L	Error in lagged inertial altitude
13	δS_3	Error in vertical channel aiding state
14	δS_4	Error in vertical channel aiding state
15	∇_{x_c}	X-component of accelerometer and velocity quantizer correlated noise
16	∇_{y_c}	Y-component of accelerometer and velocity quantizer correlated noise
17	∇_{z_c}	Z-component of accelerometer and velocity quantizer correlated noise
18	δg_x	X-component of gravity vector errors
19	δg_y	Y-component of gravity vector errors
20	δg_z	Z-component of gravity vector errors

Table 18. 39-State Reduced Order INS Truth Model, States 21-39

State Number	State Symbol	State Definition
21	b_x	X-component of gyro drift rate repeatability
22	b_y	Y-component of gyro drift rate repeatability
23	b_z	Z-component of gyro drift rate repeatability
24	S_{gx}	X-component of gyro scale factor error
25	S_{gy}	Y-component of gyro scale factor error
26	S_{gz}	Z-component of gyro scale factor error
27	∇_{b_x}	X-component of accelerometer bias repeatability
28	∇_{b_y}	Y-component of accelerometer bias repeatability
29	∇_{b_z}	Z-component of accelerometer bias repeatability
30	S_{Ax}	X-component of accelerometer and velocity quantizer scale factor
31	S_{Ay}	Y-component of accelerometer and velocity quantizer scale factor
32	S_{Az}	Z-component of accelerometer and velocity quantizer scale factor
33	S_{QAx}	X-component of accelerometer and velocity quantizer scale factor asymmetry
34	S_{QAy}	Y-component of accelerometer and velocity quantizer scale factor asymmetry
35	S_{QAz}	Z-component of accelerometer and velocity quantizer scale factor asymmetry
36	μ_1	X accelerometer misalignment about Z-axis
37	μ_2	Y accelerometer misalignment about Z-axis
38	μ_3	Z accelerometer misalignment about Y-axis
39	σ_3	Z accelerometer misalignment about X-axis

Table 19. 30-State Stand-Alone GPS Truth Model

State Number	State Symbol	State Definition
1	δR_{Uclk}	User clock bias
2	δD_{Uclk}	User clock drift
3	δR_{cl_1}	SV 1 code loop error
4	δR_{trop_1}	SV 1 tropospheric error
5	δR_{ion_1}	SV 1 ionospheric error
6	δR_{Sclk_1}	SV 1 clock error
7	δx_{sv_1}	SV 1 x-component of position error
8	δy_{sv_1}	SV 1 y-component of position error
9	δz_{sv_1}	SV 1 z-component of position error
10	δR_{cl_2}	SV 2 code loop error
11	δR_{trop_2}	SV 2 tropospheric error
12	δR_{ion_2}	SV 2 ionospheric error
13	δR_{Sclk_2}	SV 2 clock error
14	δx_{sv_2}	SV 2 x-component of position error
15	δy_{sv_2}	SV 2 y-component of position error
16	δz_{sv_2}	SV 2 z-component of position error
17	δR_{cl_3}	SV 3 code loop error
18	δR_{trop_3}	SV 3 tropospheric error
19	δR_{ion_3}	SV 3 ionospheric error
20	δR_{Sclk_3}	SV 3 clock error
21	δx_{sv_3}	SV 3 x-component of position error
22	δy_{sv_3}	SV 3 y-component of position error
23	δz_{sv_3}	SV 3 z-component of position error
24	δR_{cl_4}	SV 4 code loop error
25	$\delta R_{trop_{u4}}$	SV 4 tropospheric error
26	δR_{ion_4}	SV 4 ionospheric error
27	δR_{Sclk_4}	SV 4 clock error
28	δx_{sv_4}	SV 4 x-component of position error
29	δy_{sv_4}	SV 4 y-component of position error
30	δz_{sv_4}	SV 4 z-component of position error

Table 20. 22-State Differential GPS Truth Model

State Number	State Symbol	State Definition
1	δR_{Uclk_u}	User clock bias
2	δD_{Uclk_u}	User clock drift
3	δR_{trop_1}	SV 1 tropospheric error
4	δR_{ion_1}	SV 1 ionospheric error
5	δx_{sv_1}	SV 1 x-component of position error
6	δy_{sv_1}	SV 1 y-component of position error
7	δz_{sv_1}	SV 1 z-component of position error
8	δR_{trop_2}	SV 2 tropospheric error
9	δR_{ion_2}	SV 2 ionospheric error
10	δx_{sv_2}	SV 2 x-component of position error
11	δy_{sv_2}	SV 2 y-component of position error
12	δz_{sv_2}	SV 2 z-component of position error
13	δR_{trop_3}	SV 3 tropospheric error
14	δR_{ion_3}	SV 3 ionospheric error
15	δx_{sv_3}	SV 3 x-component of position error
16	δy_{sv_3}	SV 3 y-component of position error
17	δz_{sv_3}	SV 3 z-component of position error
18	$\delta R_{trop_{u4}}$	SV 4 tropospheric error
19	δR_{ion_4}	SV 4 ionospheric error
20	δx_{sv_4}	SV 4 x-component of position error
21	δy_{sv_4}	SV 4 y-component of position error
22	δz_{sv_4}	SV 4 z-component of position error

Table 21. 4-State Carrier Phase GPS Truth Model

State Number	State Symbol	State Definition
1	δR_{N1}	SV 1 range equivalent cycle ambiguity term
2	δR_{N2}	SV 2 range equivalent cycle ambiguity term
3	δR_{N3}	SV 3 range equivalent cycle ambiguity term
4	δR_{N4}	SV 4 range equivalent cycle ambiguity term

Table 22. 6-State SAR Truth Model

State Number	State Symbol	State Definition
1	δr_{CL}	SAR clock error
2	$\delta \dot{r}_D$	Doppler shift error
3	δC	Radar wave propagation speed error
4	δx_t	X-component of target error
5	δy_t	Y-component of target error
6	δz_t	Z-component of target error

Table 23. Filter Model, Single/Differential GPS

State Number	State Symbol	State Definition
1	$\delta\theta_x$	X-component of vector angle from true to computer frame
2	$\delta\theta_y$	Y-component of vector angle from true to computer frame
3	$\delta\theta_z$	Z-component of vector angle from true to computer frame
4	ϕ_x	X-component of vector angle from true to platform frame
5	ϕ_y	Y-component of vector angle from true to platform frame
6	ϕ_z	Z-component of vector angle from true to platform frame
7	δV_x	X-component of error in computed velocity
8	δV_y	Y-component of error in computed velocity
9	δV_z	Z-component of error in computed velocity
10	δh	Error in vehicle altitude above reference ellipsoid
11	δh_B	Total baro-altimeter correlated error
12	δR_{Uclk_u}	User clock bias
13	δD_{Uclk_u}	User clock drift
14	δr_{SAR}	SAR range bias
15	$\delta \dot{r}_{SAR}$	SAR range rate bias
16	δx_t	X-component of target error
17	δy_t	Y-component of target error
18	δz_t	Z-component of target error

Table 24. Filter Model, Carrier Phase GPS

State Number	State Symbol	State Definition
1	$\delta\theta_x$	X-component of vector angle from true to computer frame
2	$\delta\theta_y$	Y-component of vector angle from true to computer frame
3	$\delta\theta_z$	Z-component of vector angle from true to computer frame
4	ϕ_x	X-component of vector angle from true to platform frame
5	ϕ_y	Y-component of vector angle from true to platform frame
6	ϕ_z	Z-component of vector angle from true to platform frame
7	δV_x	X-component of error in computed velocity
8	δV_y	Y-component of error in computed velocity
9	δV_z	Z-component of error in computed velocity
10	δh	Error in vehicle altitude above reference ellipsoid
11	δh_B	Total baro-altimeter correlated error
12	δR_{N1}	SV 1 range equivalent cycle ambiguity term
13	δR_{N2}	SV 2 range equivalent cycle ambiguity term
14	δR_{N3}	SV 3 range equivalent cycle ambiguity term
15	δR_{N4}	SV 4 range equivalent cycle ambiguity term
16	δr_{SAR}	SAR range bias
17	$\delta \dot{r}_{SAR}$	SAR range rate bias
18	δx_t	X-component of target error
19	δy_t	Y-component of target error
20	δz_t	Z-component of target error

Table 25. Elements of the Dynamics Submatrix F_{11}

Element	Term	Element	Term
(1,3)	$-\rho_y$	(1,8)	$-C_{RY}$
(2,3)	ρ_x	(2,7)	C_{RX}
(3,1)	ρ_y	(3,2)	$-\rho_x$
(4,2)	$-\Omega_z$	(4,3)	Ω_y
(4,5)	ω_{in_z}	(4,6)	$-\omega_{in_y}$
(4,8)	$-C_{RY}$	(5,1)	Ω_z
(5,3)	$-\Omega_x$	(5,4)	$-\omega_{in_z}$
(5,6)	ω_{in_x}	(5,7)	C_{RX}
(6,1)	$-\Omega_y$	(6,2)	Ω_x
(6,4)	ω_{in_y}	(6,5)	$-\omega_{in_x}$
(7,1)	$-2V_y\Omega_y - 2V_z\Omega_z$	(7,2)	$2V_y\Omega_x$
(7,3)	$2V_z\Omega_x$	(7,5)	$-A_z$
(7,6)	A_y	(7,7)	$-V_zC_{RX}$
(7,8)	$2\Omega_z$	(7,9)	$-\rho_y - 2\Omega_y$
(8,1)	$2V_x\Omega_y$	(8,2)	$-2V_x\Omega_x - 2V_z\Omega_z$
(8,3)	$2V_z\Omega_y$	(8,4)	A_z
(8,6)	$-A_x$	(8,7)	$-2\Omega_z$
(8,8)	$-V_zC_{RY}$	(8,9)	$\rho_x + 2\Omega_x$
(9,1)	$2V_x\Omega_z$	(9,2)	$2V_y\Omega_z$
(9,3)	$-2V_y\Omega_y - 2V_x\Omega_x$	(9,4)	$-A_y$
(9,5)	A_x	(9,7)	$\rho_y + 2\Omega_y + V_xC_{RX}$
(9,8)	$-\rho_x - 2\Omega_x + V_yC_{RY}$	(9,10)	$2g_o / a$
(9,14)	$-k_2$	(9,12)	-1
(9,16)	k_2	(10,9)	1
(10,14)	$-k_1$	(10,16)	$k_1 - 1$
(14,10)	1	(14,14)	-1
(15,14)	k_3	(15,16)	$-k_3$
(16,10)	k_4	(16,14)	$-k_4$
(16,16)	$k_4 - 1$		

$\rho_{x,y}$ = Components of angular rate, navigation frame to ECEF frame

$\Omega_{x,y,z}$ = Components of angular rate, ECEF to inertial frame

$\omega_{in_{x,y,z}}$ = Components of angular rate, navigation frame to inertial frame

$V_{x,y,z}$ = Components of vehicle velocity vector in ECEF coordinates

$A_{x,y,z}$ = Components of specific force in sensor frame

$k_{1,2,3,4}$ = Vertical channel gains a = Equatorial radius of the earth (6378388m)

$C_{RX,RY}$ = Components of earth spheroid inverse radii of curvature

g_o = Equatorial gravity (32.08744ft/sec^2)

Table 26. Elements of the Dynamics Submatrix $\mathbf{F_{12}}$

Element	Term	Element	Term	Element	Term
(7,17)	C_{11}	(7,18)	C_{12}	(7,19)	C_{13}
(7,20)	1	(8,17)	C_{21}	(8,18)	C_{22}
(8,19)	C_{23}	(8,21)	1	(9,17)	C_{31}
(9,18)	C_{32}	(9,19)	C_{33}	(9,22)	1
(9,11)	k_2	(10,11)	k_1	(15,11)	$-k_3$
(16,11)	$k_4/600$				

Note: For the above element definitions, $t_0 = 0$

C = Coordinate transformation matrix from body frame to navigation frame, $\mathbf{C}_b^n$

Table 27. Elements of the Dynamics Submatrix $\mathbf{F_{13}}$

Element	Term	Element	Term	Element	Term
(4,23)	C_{11}	(4,24)	C_{12}	(4,25)	C_{13}
(4,26)	$C_{11}\omega_{in_x}$	(4,27)	$C_{12}\omega_{in_y}$	(4,28)	$C_{13}\omega_{in_z}$
(5,23)	C_{21}	(5,24)	C_{22}	(5,25)	C_{23}
(5,26)	$C_{21}\omega_{in_x}$	(5,27)	$C_{22}\omega_{in_y}$	(5,28)	$C_{23}\omega_{in_z}$
(6,23)	C_{31}	(6,24)	C_{32}	(6,25)	C_{33}
(6,26)	$C_{31}\omega_{in_x}$	(6,27)	$C_{32}\omega_{in_y}$	(6,28)	$C_{33}\omega_{in_z}$

Table 28. Elements of the Dynamics Submatrix F_{14}

Element	Term	Element	Term	Element	Term
(7,29)	C_{11}	(7,30)	C_{12}	(7,31)	C_{13}
(7,32)	$C_{11}A_x^B$	(7,33)	$C_{12}A_y^B$	(7,34)	$C_{13}A_z^{B'}$
(7,35)	$C_{11}\lvert A_x^B\rvert$	(7,36)	$C_{12}\lvert A_y^B\rvert$	(7,37)	$C_{13}\lvert A_z^{B'}\rvert$
(7,38)	$C_{11}A_y^B$	(7,39)	$-C_{12}A_x^B$	(7,40)	$C_{13}A_y^B$
(7,41)	$C_{13}A_x^B$	(8,29)	C_{21}	(8,30)	C_{22}
(8,31)	C_{23}	(8,32)	$C_{21}A_x^B$	(8,33)	$C_{22}A_y^B$
(8,34)	$C_{23}A_z^{B'}$	(8,35)	$C_{21}\lvert A_x^B\rvert$	(8,36)	$C_{22}\lvert A_y^B\rvert$
(8,37)	$C_{23}\lvert A_z^{B'}\rvert$	(8,38)	$C_{21}A_y^B$	(8,39)	$-C_{22}A_x^B$
(8,40)	$C_{23}A_y^B$	(8,41)	$C_{23}A_x^B$	(9,29)	C_{31}
(9,30)	C_{32}	(9,31)	C_{33}	(9,32)	$C_{31}A_x^B$
(9,33)	$C_{32}A_y^B$	(9,34)	$C_{33}A_z^{B'}$	(9,35)	$C_{31}\lvert A_x^B\rvert$
(9,36)	$C_{32}\lvert A_y^B\rvert$	(9,37)	$C_{33}\lvert A_z^{B'}\rvert$	(9,38)	$C_{31}A_y^B$
(9,39)	$-C_{32}A_x^B$	(9,40)	$C_{33}A_y^B$	(9,41)	$C_{33}A_x^B$

$A_{x,y,z}^B$ = Components of acceleration in the body frame

$A_z^{B'}$ = Specific force component (includes gravity)

Table 29. Elements of the Dynamics Submatrix F_{22}

Element	Term	Element	Term	Element	Term
(17,17)	$-\beta_{\nabla_{x_c}}$	(18,18)	$-\beta_{\nabla_{y_c}}$	(19,19)	$-\beta_{\nabla_{z_c}}$
(20,20)	$-\beta_{\delta g_x}$	(21,21)	$-\beta_{\delta g_y}$	(22,22)	$-\beta_{\delta g_z}$
(11,11)	$-\beta_{\delta h_c}$				

$\beta_{b_{x_c,y_c,z_c}}$ = Gyro inverse correlation time constants (5 min)

$\beta_{\nabla_{x_c,y_c,z_c}}$ = Accelerometer inverse correlation time constants (5 min)

$\beta_{\delta g_{x,y,z}}$ = Gravity vector error inverse correlation time constants (V/20NM)

$\beta_{\delta h_c}$ = Barometer inverse correlation time (10 min)

Table 30. Non-Zero Elements of Process Noise Submatrix Q_{11}

Element	Term	Element	Term
(4,4)	$\sigma^2_{\eta_{b_x}}$	(5,5)	$\sigma^2_{\eta_{b_y}}$
(6,6)	$\sigma^2_{\eta_{b_z}}$	(7,7)	$\sigma^2_{\eta_{A_x}}$
(8,8)	$\sigma^2_{\eta_{A_y}}$	(9,9)	$\sigma^2_{\eta_{A_z}}$

$\sigma^2_{\eta_{b_{x,y,z}}}$ = PSD value of gyro drift rate white noise (6.25e-10$\frac{deg^2}{sec^3}$)

$\sigma^2_{\eta_{A_{x,y,z}}}$ = PSD value of accelerometer white noise (1.037e-7$\frac{ft^2}{sec^3}$)

Table 31. Non-Zero Elements of Process Noise Submatrix Q_{22}

Element	Term	Element	Term
(17,17)	$2\beta_{\nabla_{x_c}}\sigma^2_{\nabla_{x_c}}$	(18,18)	$2\beta_{\nabla_{y_c}}\sigma^2_{\nabla_{y_c}}$
(19,19)	$2\beta_{\nabla_{z_c}}\sigma^2_{\nabla_{z_c}}$	(20,20)	$2\beta_{\delta g_x}\sigma^2_{\delta g_x}$
(21,21)	$2\beta_{\delta g_y}\sigma^2_{\delta g_y}$	(22,22)	$2\beta_{\delta g_z}\sigma^2_{\delta g_z}$
(11,11)	$2\beta_{\delta h_c}\sigma^2_{\delta h_c}$		

$\sigma^2_{b_{x_c,y_c,z_c}}$ = Variances of gyro drift correlated noise (3.086e-13 $\frac{deg^2}{sec^2}$)

$\sigma^2_{\nabla_{x_c,y_c,z_c}}$ = Variances of accelerometer correlated noise (4.147e-9 $\frac{ft^2}{sec^4}$)

$\sigma^2_{\delta g_{x,y,z}}$ = Variances of gravity vector error component correlated noise (1.93e-6 deg^2)

$\sigma^2_{\delta h_c}$ = Variance of barometer correlated noise (10000 ft^2)

Table 32. Measurement Noise Strengths, Truth and Filter

Measurement	Truth Model Value	Filter Model Value	Units
Baro-Altimeter	2500.0	3500.0	ft^2
SGPS	9.0	170.0	ft^2
DGPS	9.0	15.0	ft^2
CPGPS	2.6E-4	3.0E-4	ft^2
SAR Range	1.0	2.0	ft^2
SAR Range Rate	0.09	0.12	ft^2/sec^2

Table 33. Tuning Values for Filter States, All GPS Models

State	SGPS	DGPS	CPGPS	Units
$\delta\theta_x$	8.0E-14	5.0E-15	5.0E-15	$(arc\text{-}sec)^2/sec$
$\delta\theta_y$	7.0E-13	4.0E-14	9.0E-14	$(arc\text{-}sec)^2/sec$
$\delta\theta_z$	0.0	0.0	0.0	$(arc\text{-}sec)^2/sec$
ϕ_x	10.0	5.0	5.0	$(arc\text{-}sec)^2/sec$
ϕ_y	2.0	5.0	5.0	$(arc\text{-}sec)^2/sec$
ϕ_z	25.0	85.0	85.0	$(arc\text{-}sec)^2/sec$
δV_x	75.0	50.0	50.0	ft^2/sec^3
δV_y	100.0	50.0	50.0	ft^2/sec^3
δV_z	25000.0	50.0	50.0	ft^2/sec^3
δh	110.0	110.0	110.0	ft^2/sec
δh_B	90.0	90.0	90.0	ft^2/sec
δR_{Uclk_u}	75.0	100.0	100.0	ft^2/sec
δD_{Uclk_u}	5.0E-13	5.0E-13	5.0E-13	ft^2/sec^3
δR_{N1}	N/A	N/A	2.0E-8	ft^2/sec
δR_{N2}	N/A	N/A	2.0E-8	ft^2/sec
δR_{N3}	N/A	N/A	8.0E-5	ft^2/sec
δR_{N4}	N/A	N/A	2.0E-8	ft^2/sec
δr_{SAR}	0.0	0.0	0.0	ft^2/sec
$\delta \dot{r}_{SAR}$	0.0	0.0	0.0	ft^2/sec^3
δx_t	0.0	0.0	0.0	ft^2/sec
δy_t	0.0	0.0	0.0	ft^2/sec
δz_t	0.0	0.0	0.0	ft^2/sec

Appendix C. Stand-Alone GPS Results

The following figures describe the data generated from the SGPS simulation. Each state in the filter model is plotted. The following legend describes the traces in each figure of Appendix C:

Plot Legend:

true error (mean error $\pm \sigma_{true}$)

filter predicted error ($0 \pm \sigma_{filter}$)

mean error

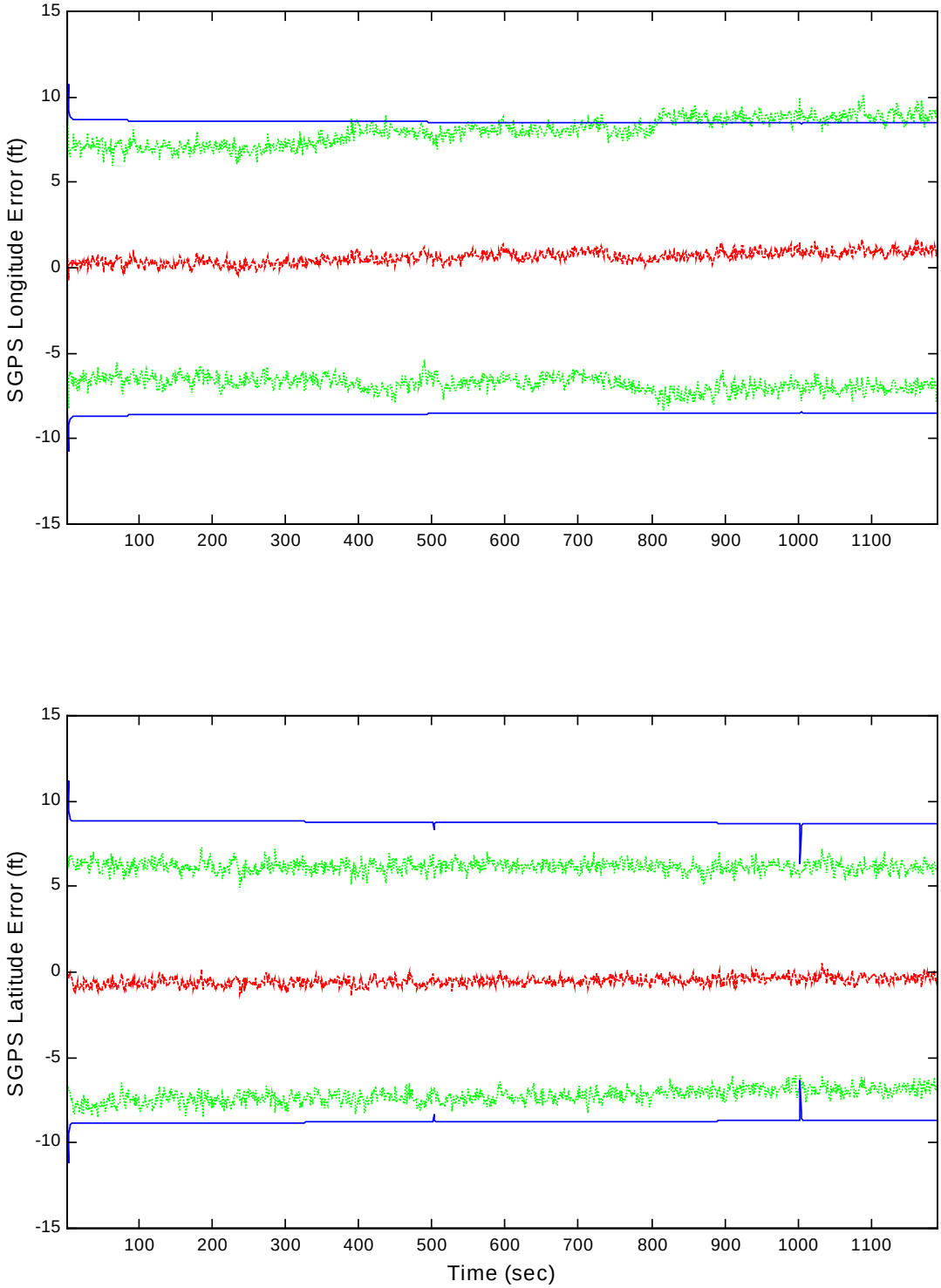

Figure 22. SGPS Latitude and Longitude Errors

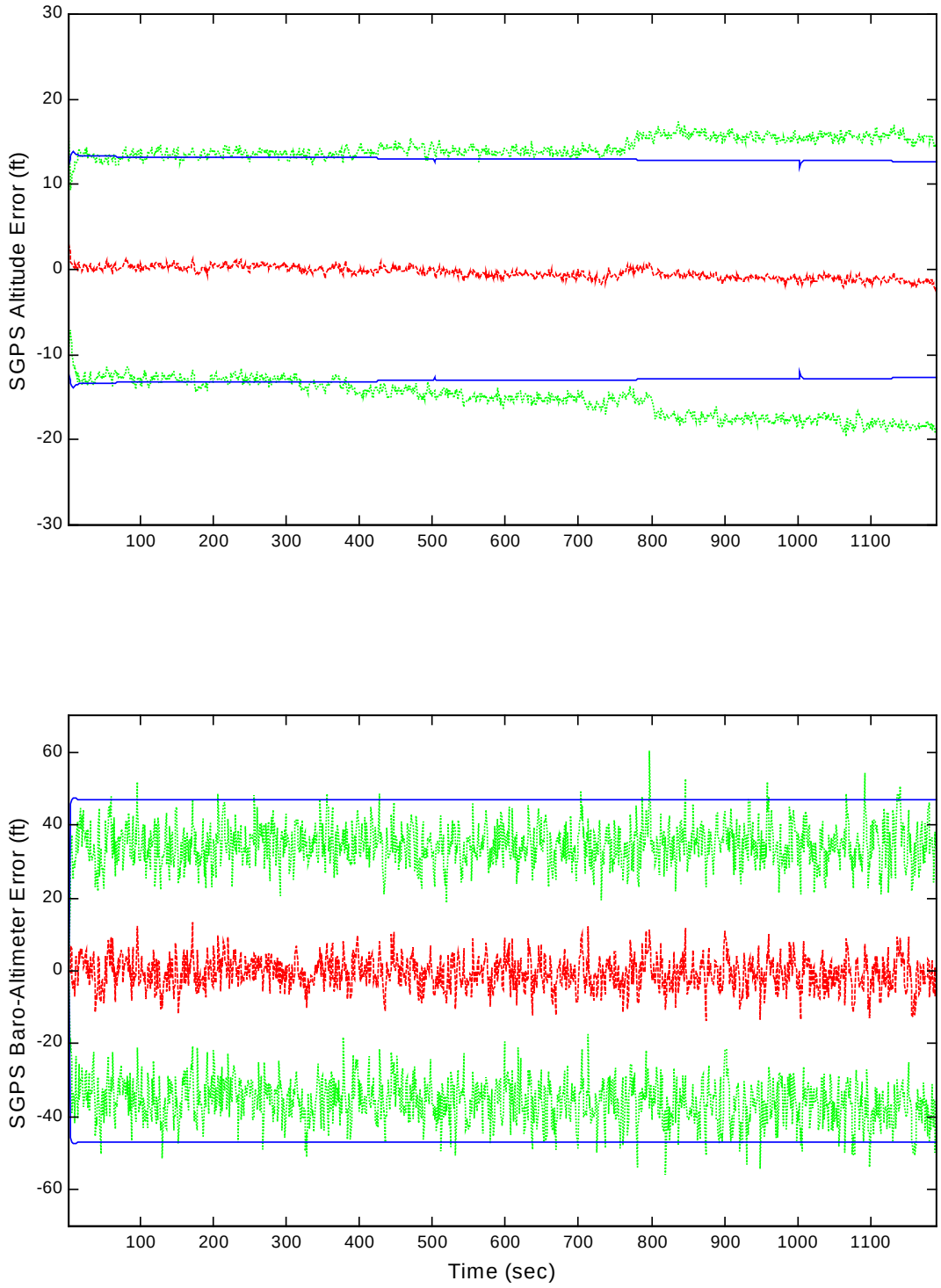

Figure 23. SGPS Altitude and Barometric Altimeter Bias Errors

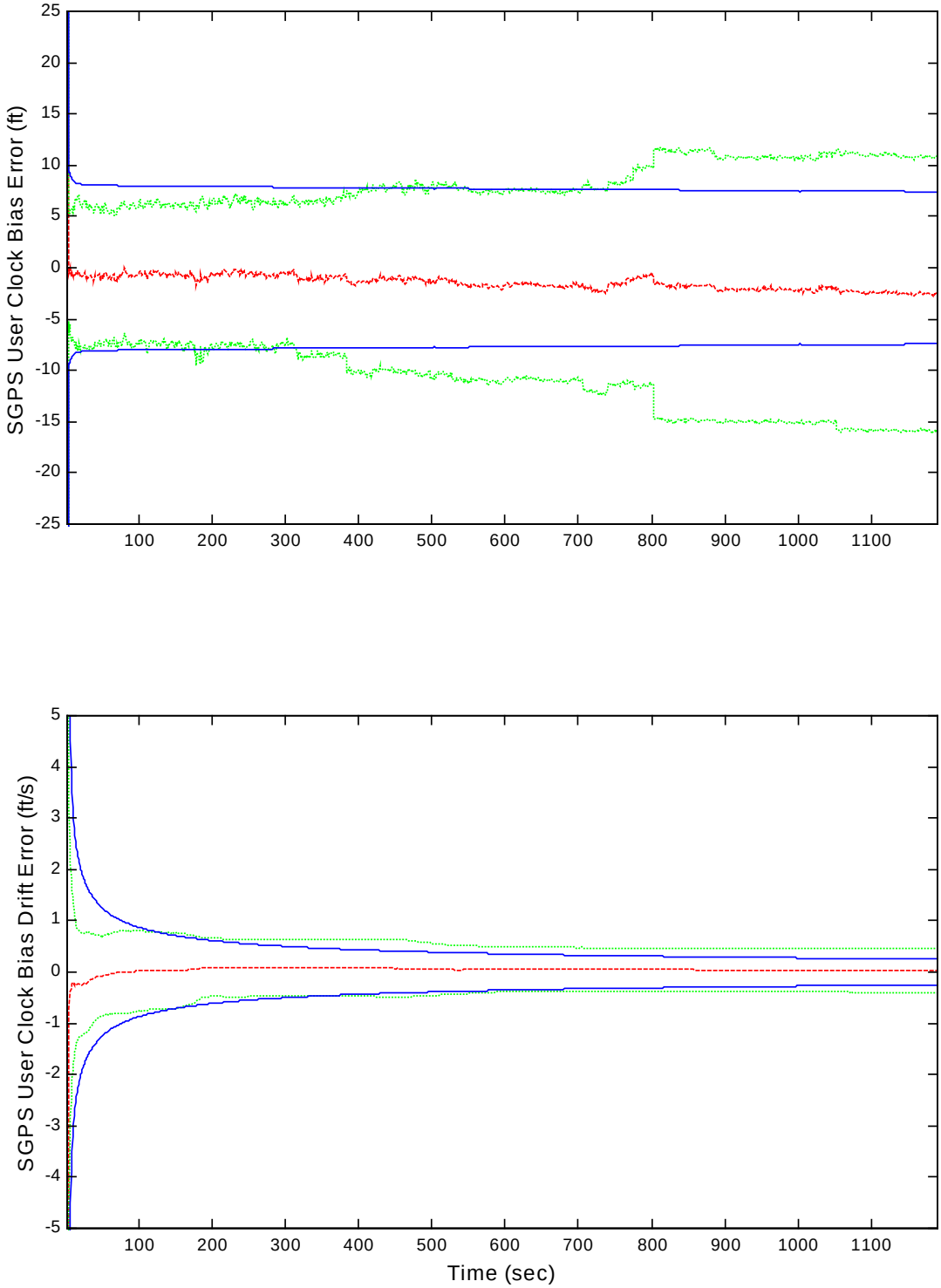

Figure 24. SGPS User Clock Bias and Clock Bias Drift Errors

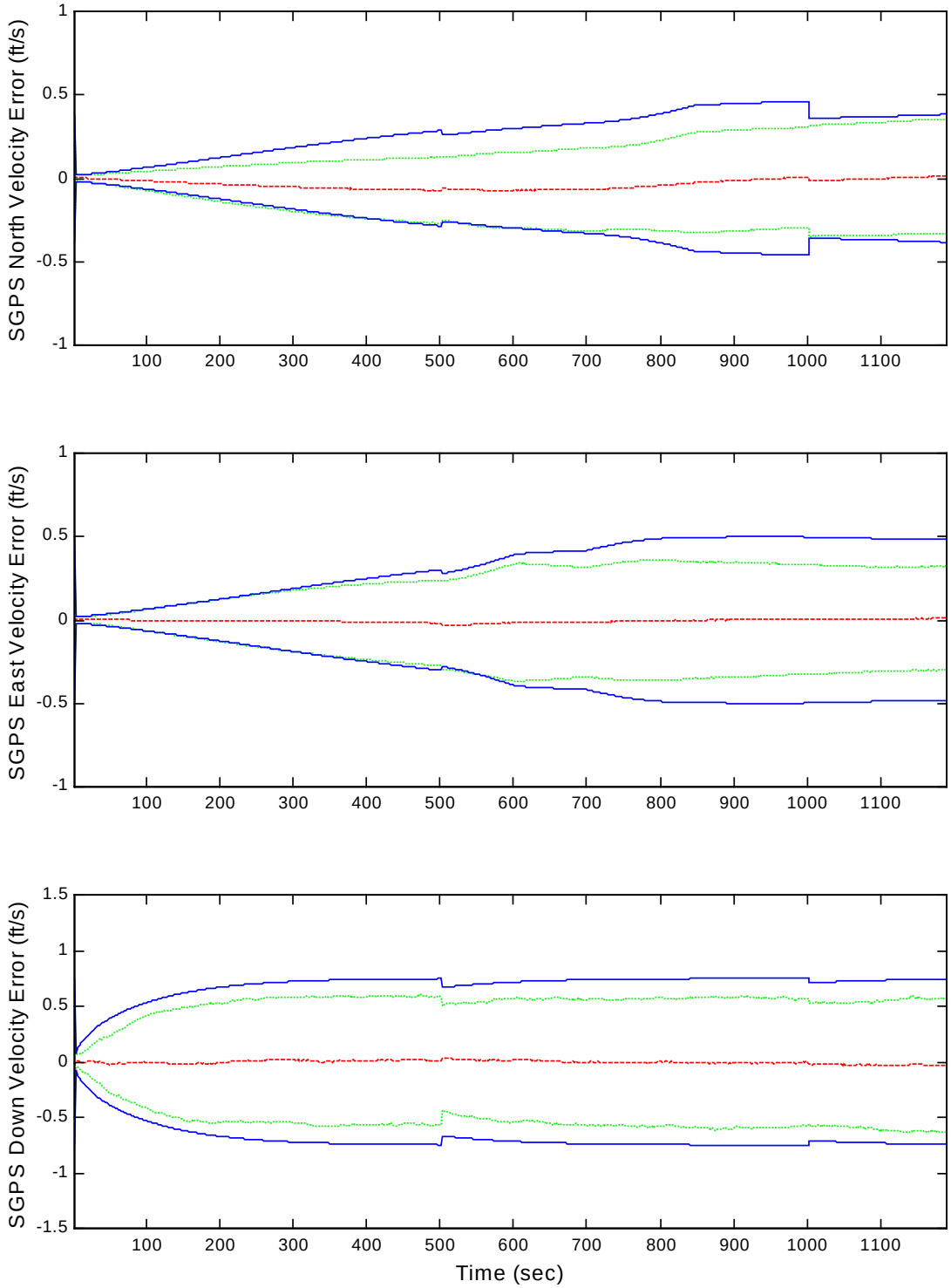

Figure 25. SGPS North, East, and Down Velocity Errors

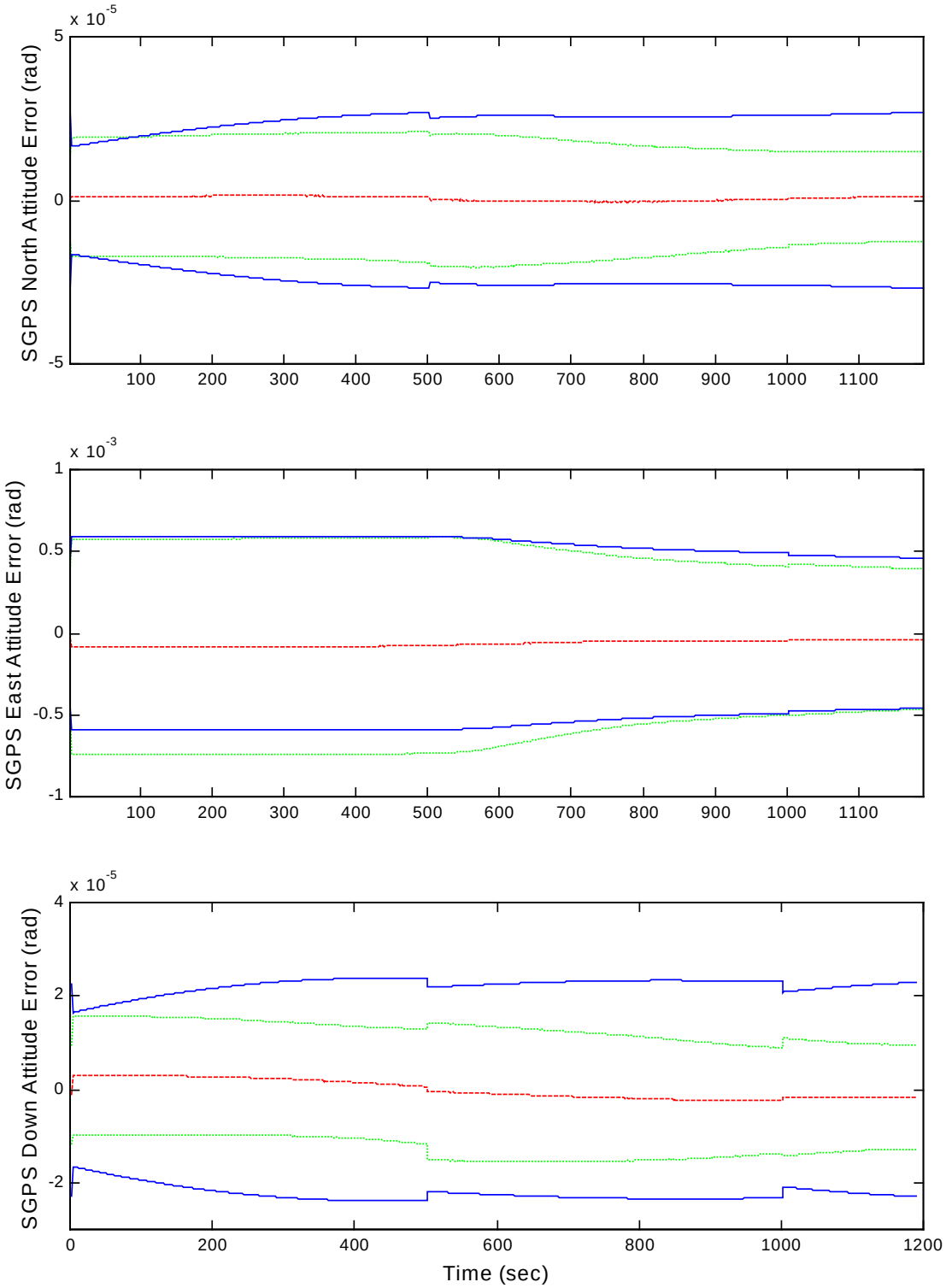

Figure 26. SGPS North, East, and Down Attitude Errors

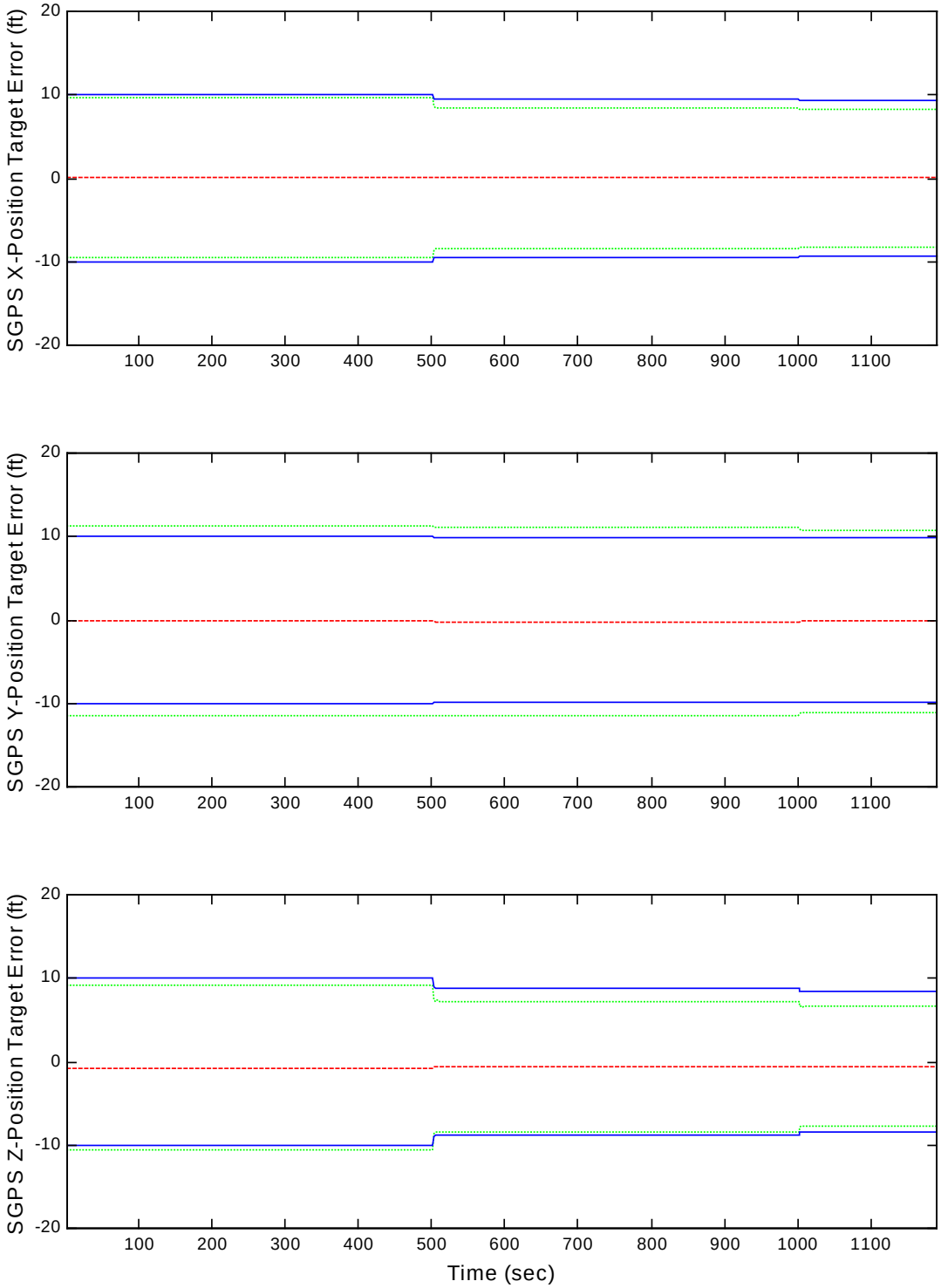

Figure 27. SGPS SAR X, Y, and Z-Target Position Errors

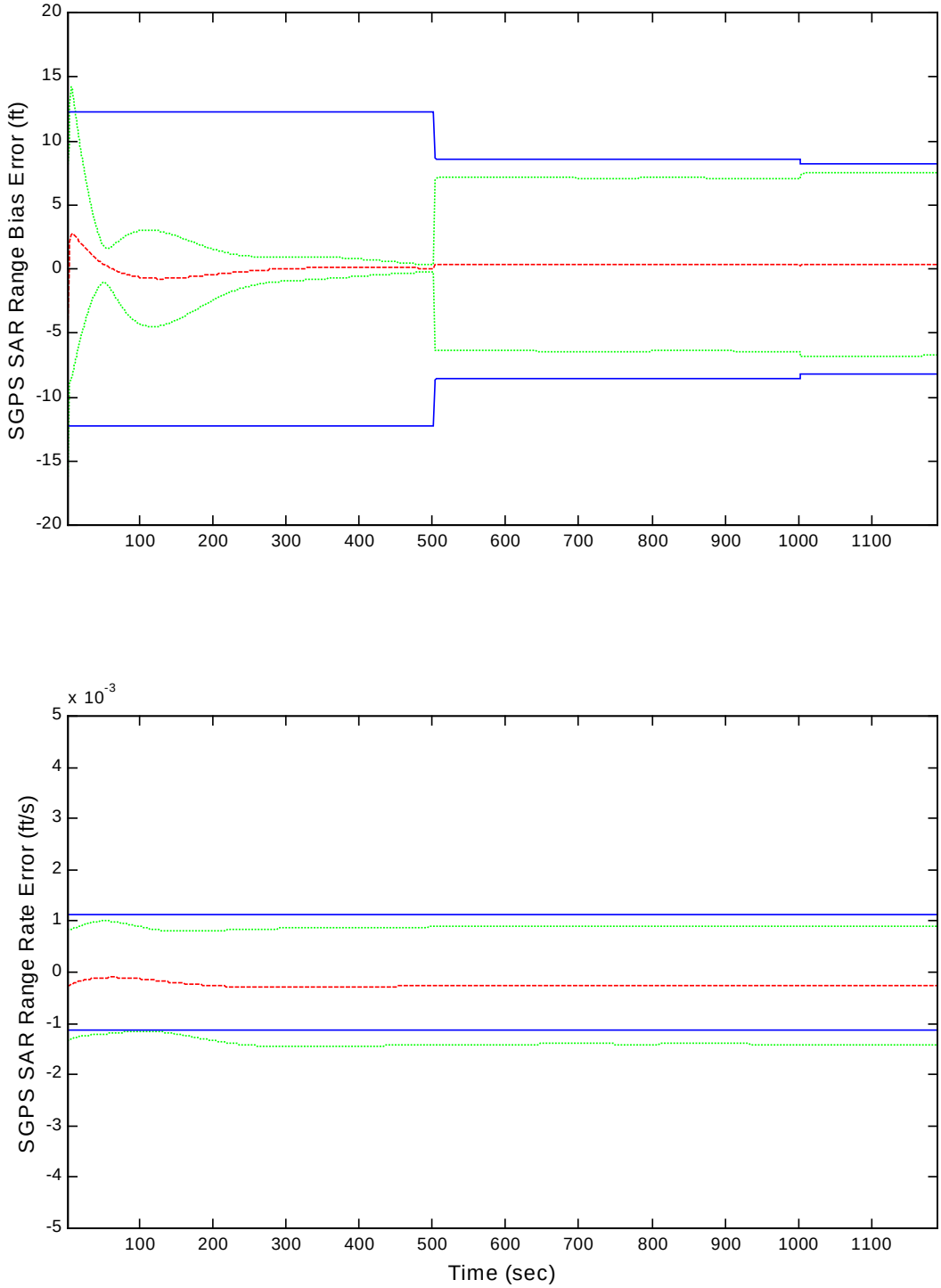

Figure 28. SGPS SAR Range and Range Rate Bias Errors

Appendix D. Differential GPS Results

The following figures describe the data generated from the DGPS simulation. Each state in the filter model is plotted. The following legend describes the traces in each figure of Appendix D:

Plot Legend:

true error (mean error $\pm \sigma_{true}$)

filter predicted error ($0 \pm \sigma_{filter}$)

mean error

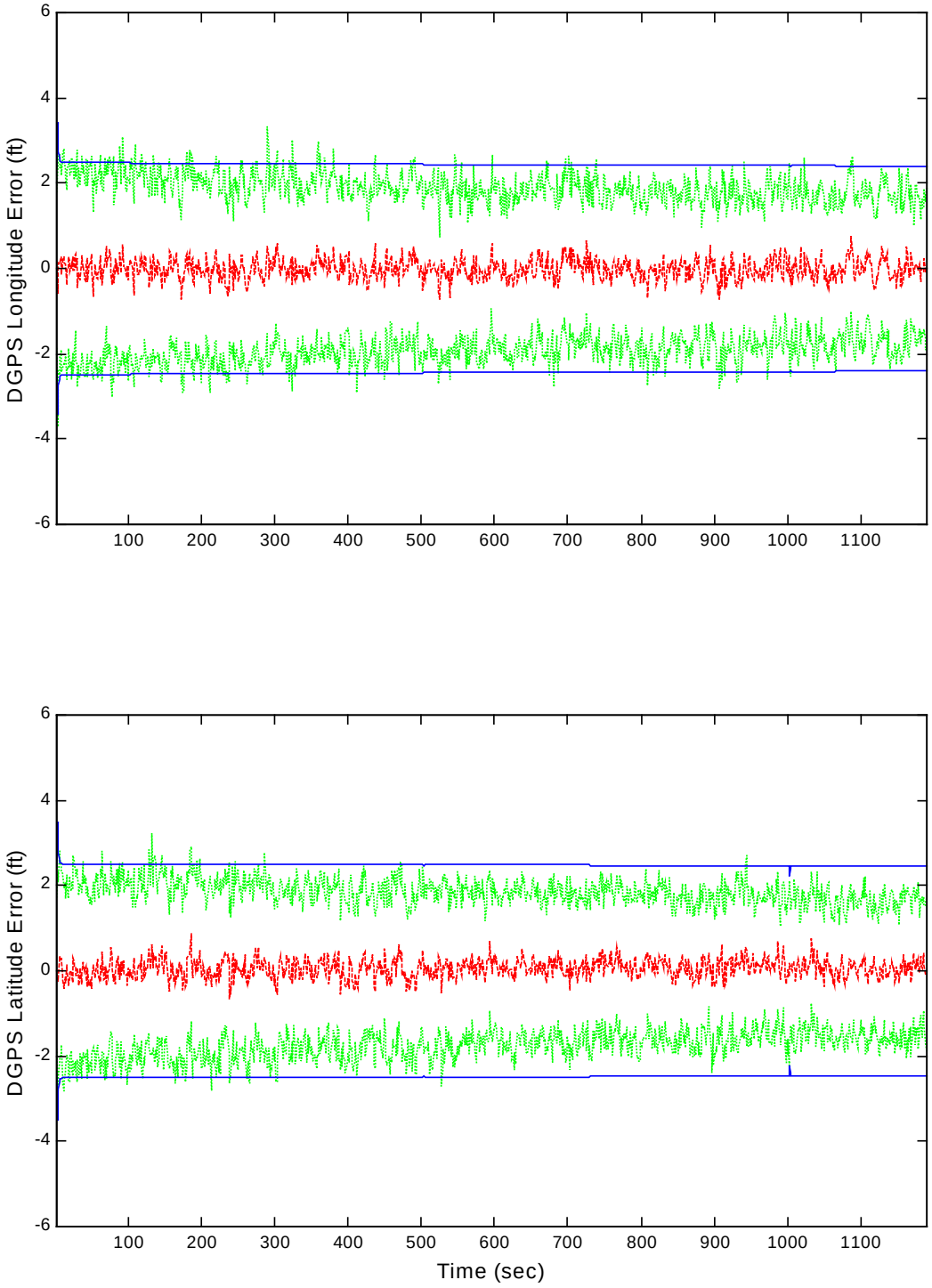

Figure 29. DGPS Latitude and Longitude Errors

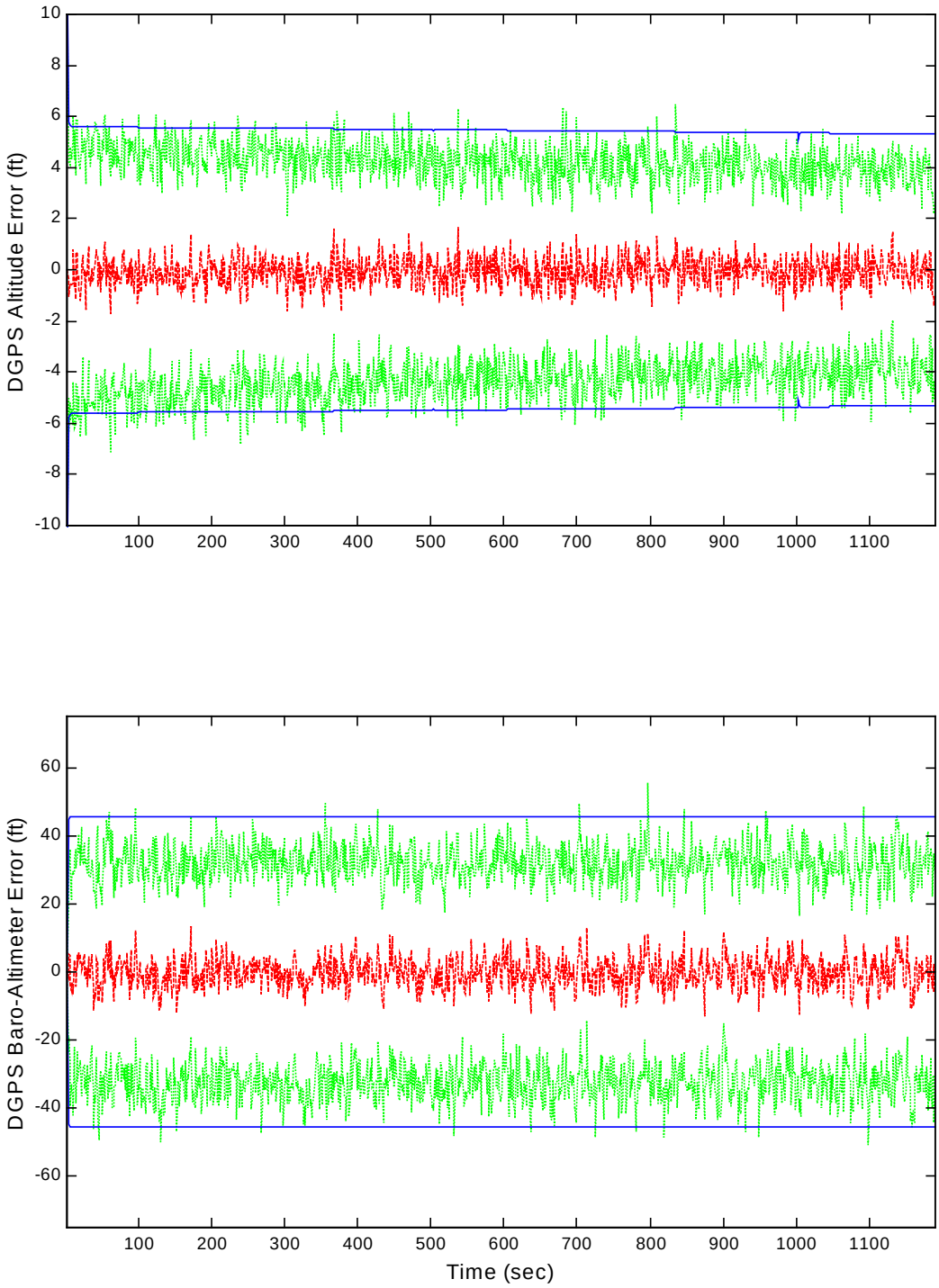

Figure 30. DGPS Altitude and Barometric Altimeter Bias Errors

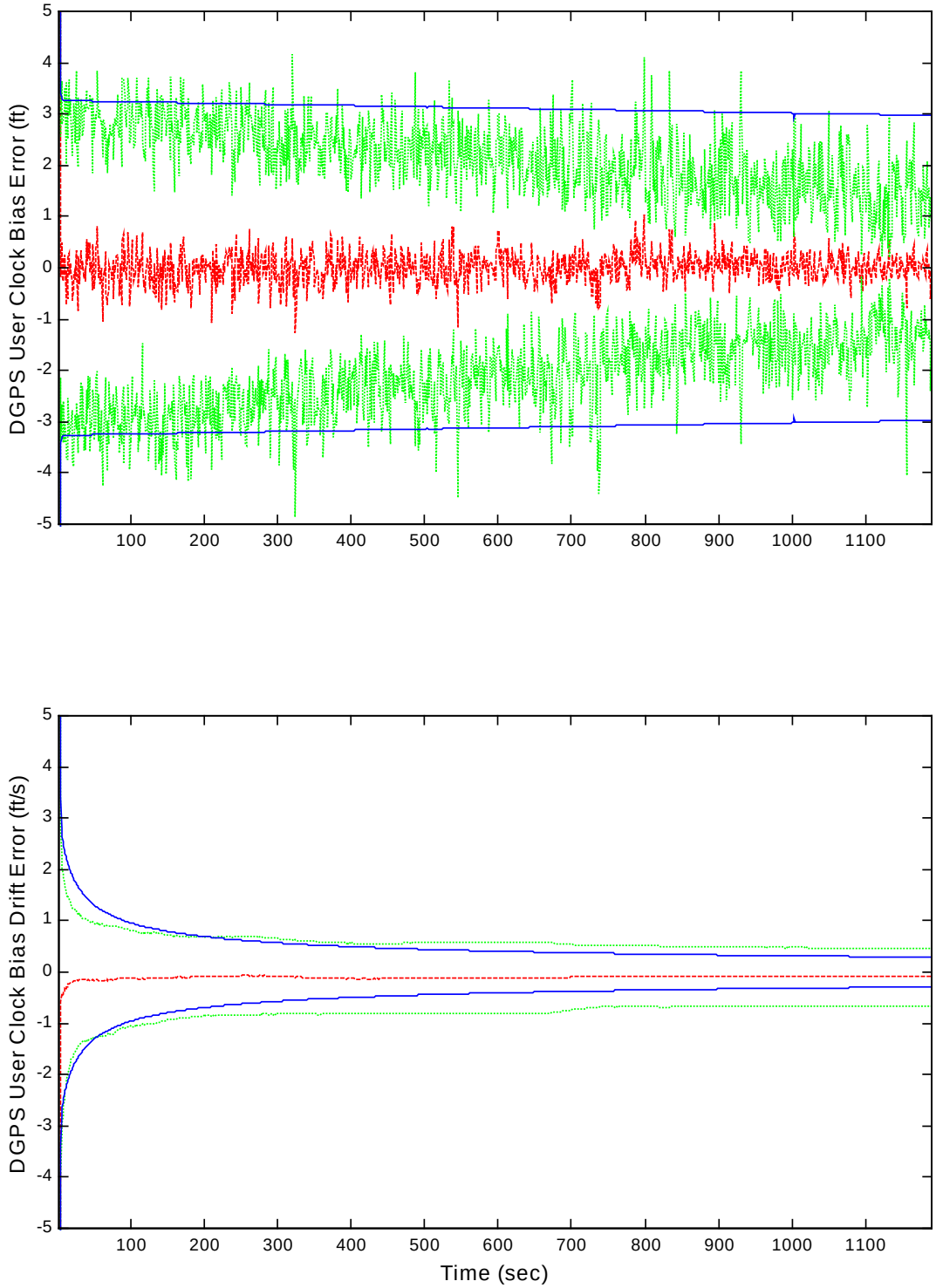

Figure 31. DGPS User Clock Bias and Clock Bias Drift Errors

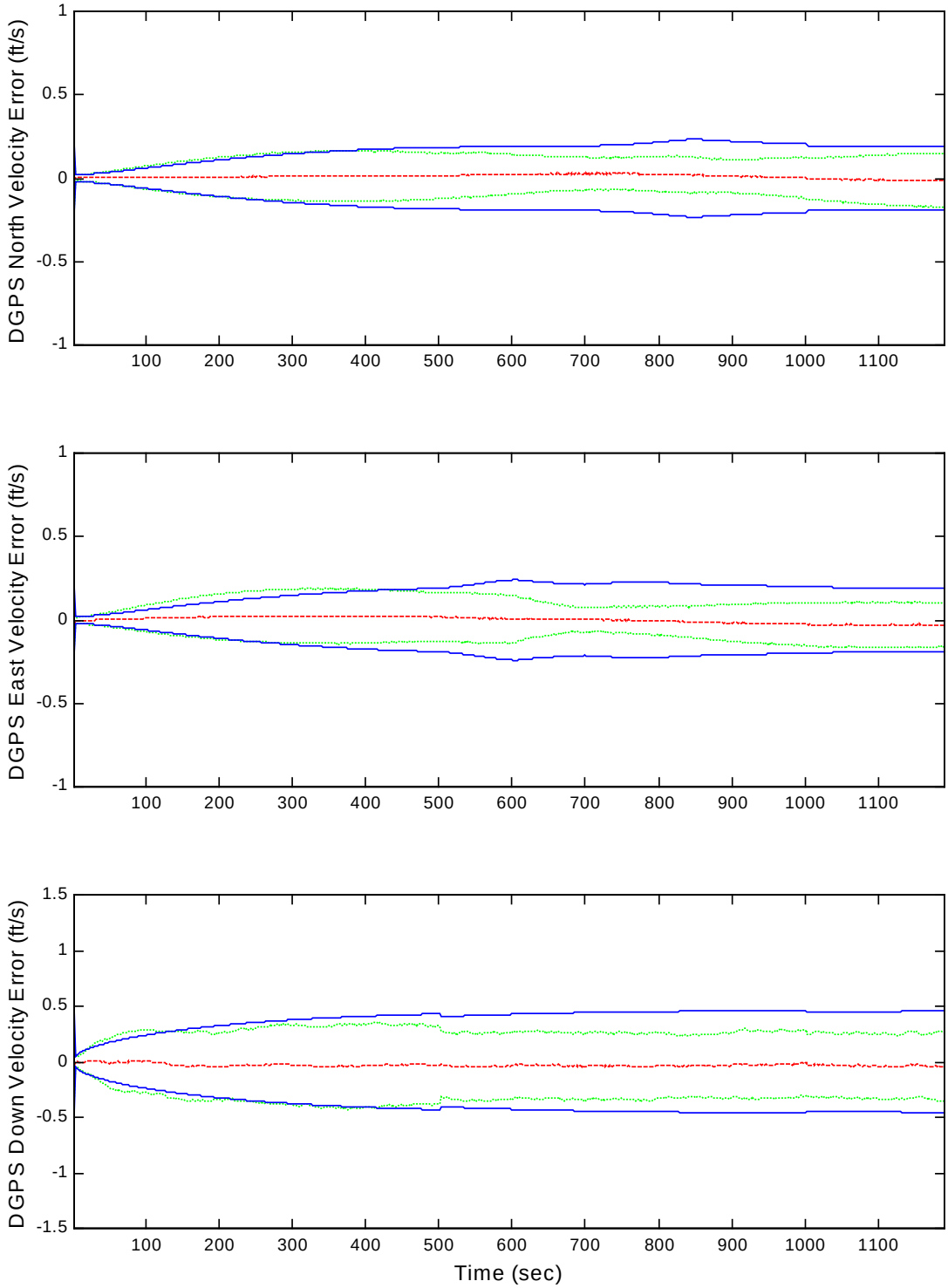

Figure 32. DGPS North, East, and Down Velocity Errors

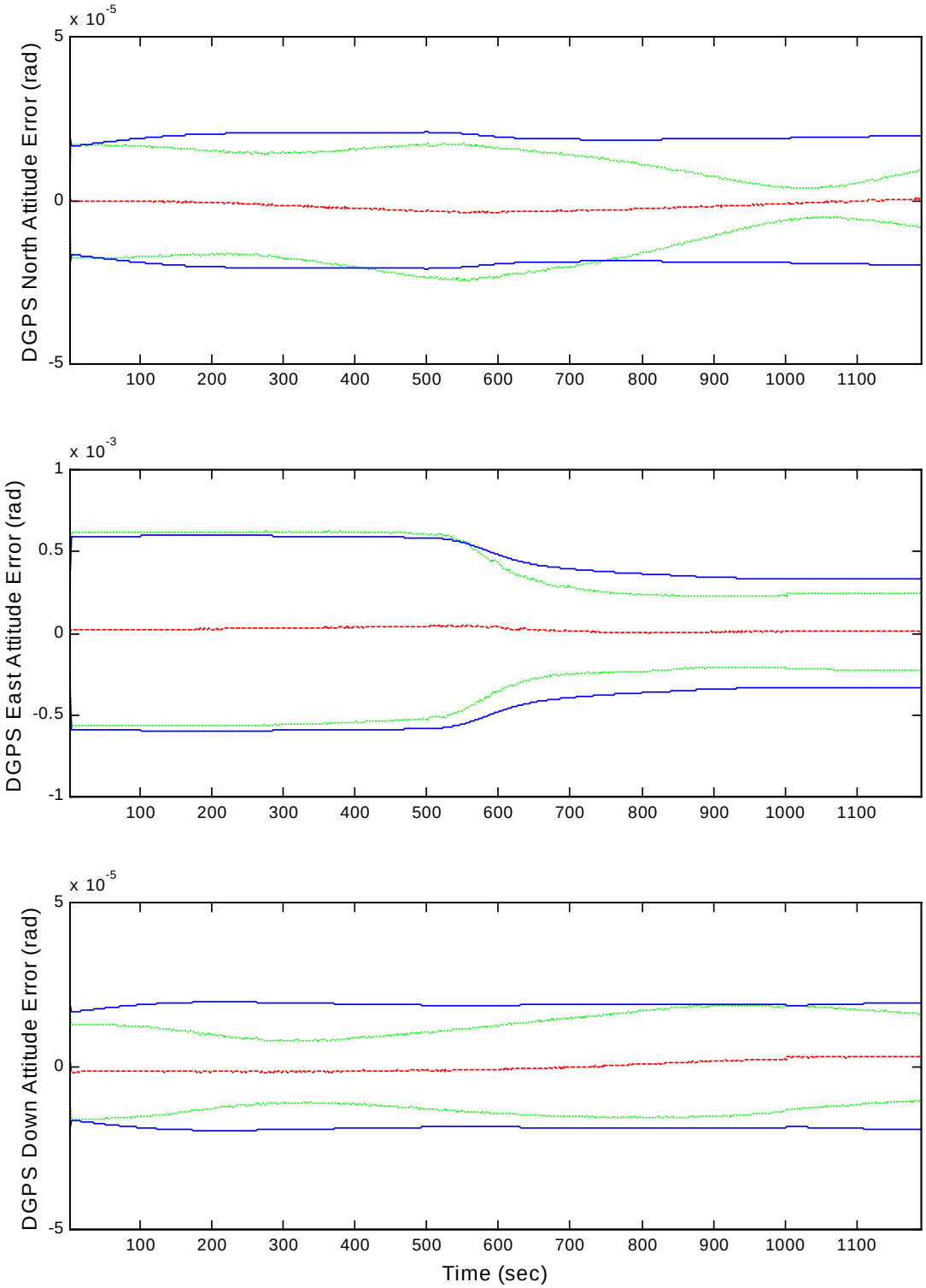

Figure 33. DGPS North, East, and Down Attitude Errors

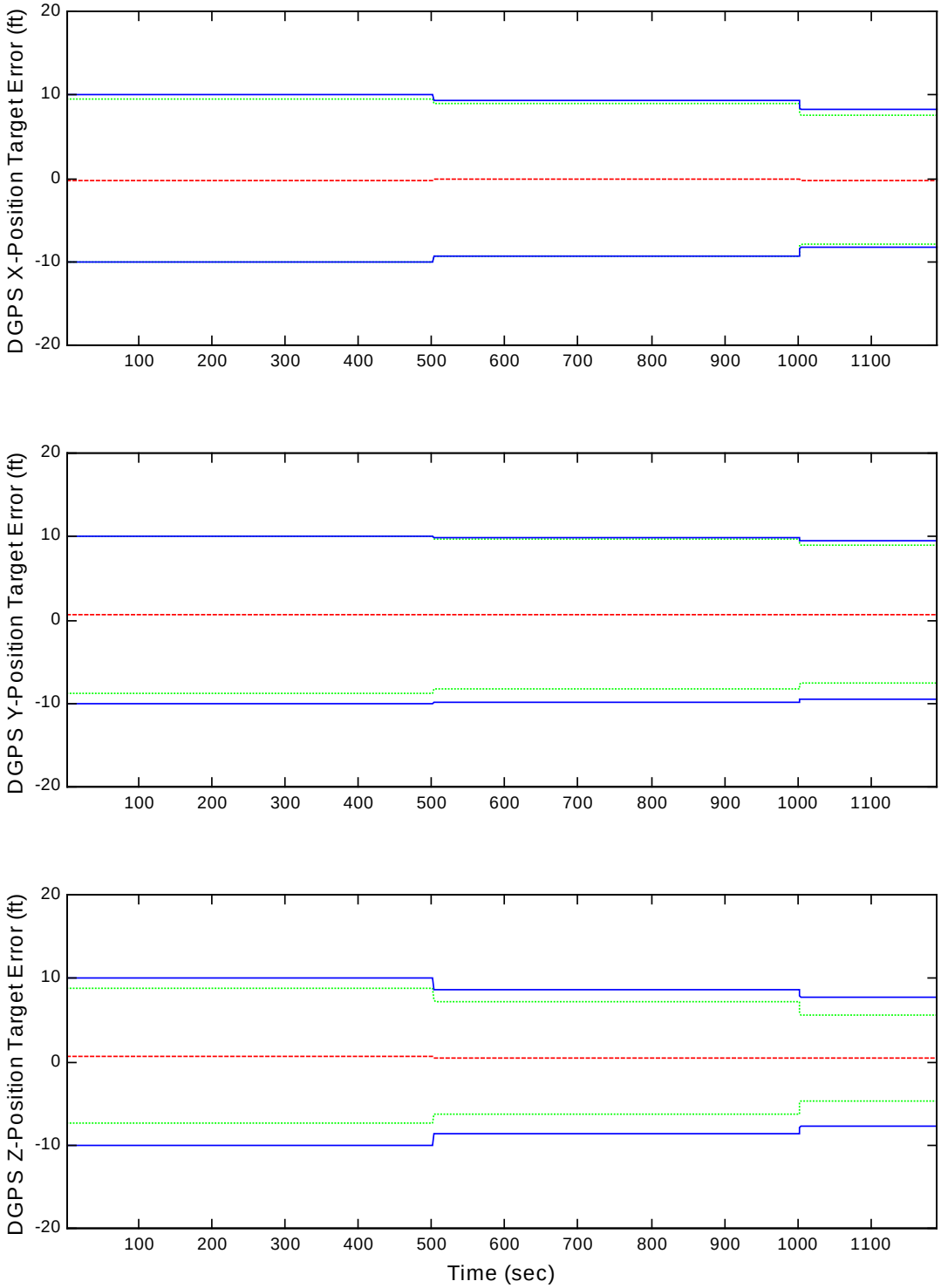

Figure 34. DGPS SAR X, Y, and Z-Target Position Errors

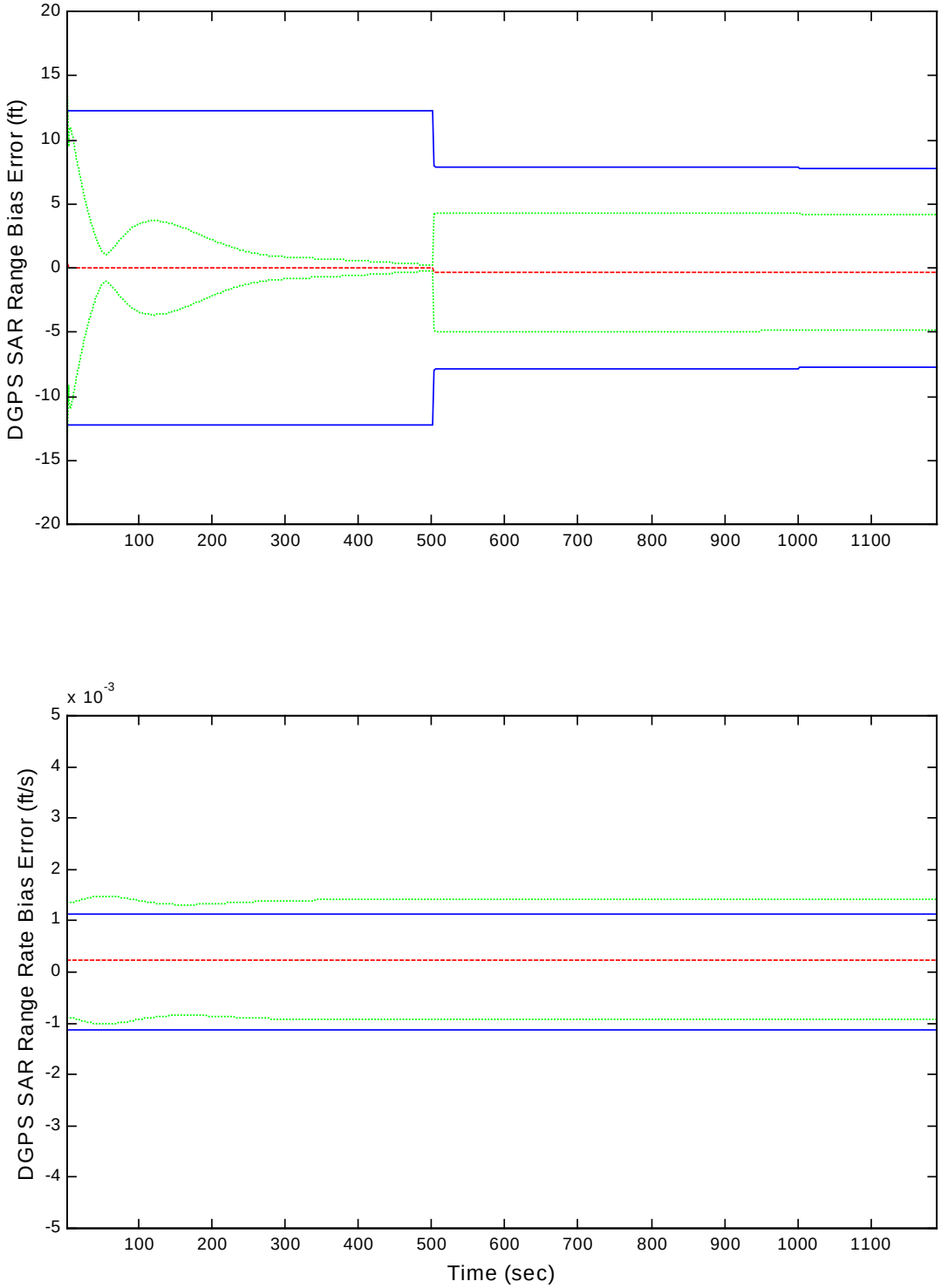

Figure 35. DGPS SAR Range and Range Rate Bias Errors

Appendix E. Carrier Phase GPS Results

The following figures describe the data generated from the CPGPS simulation. Each state in the filter model is plotted. The following legend describes the traces in each figure of Appendix E:

Plot Legend:

true error (mean error $\pm \sigma_{true}$)

filter predicted error ($0 \pm \sigma_{filter}$)

mean error

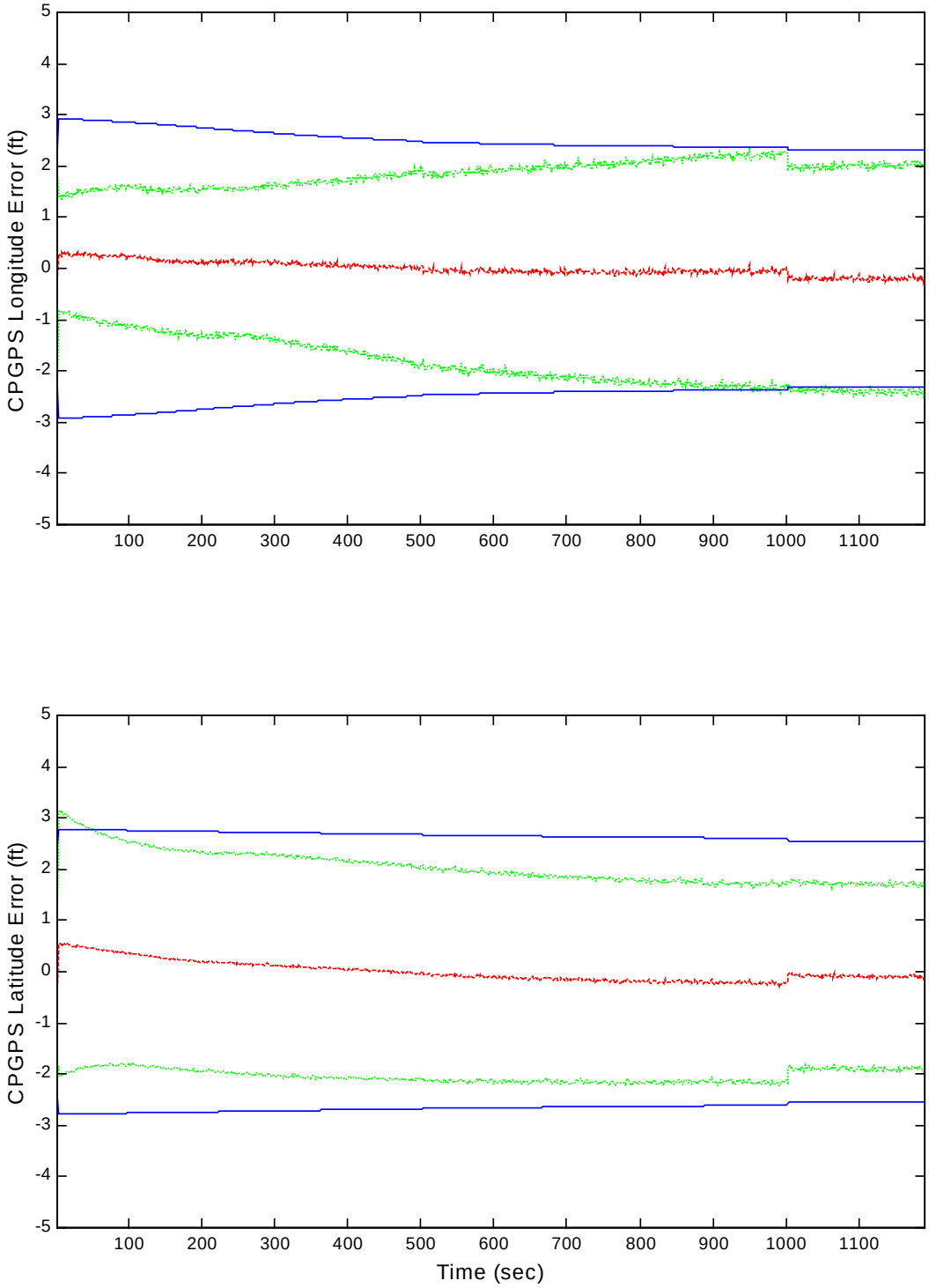

Figure 36. CPGPS Latitude and Longitude Errors

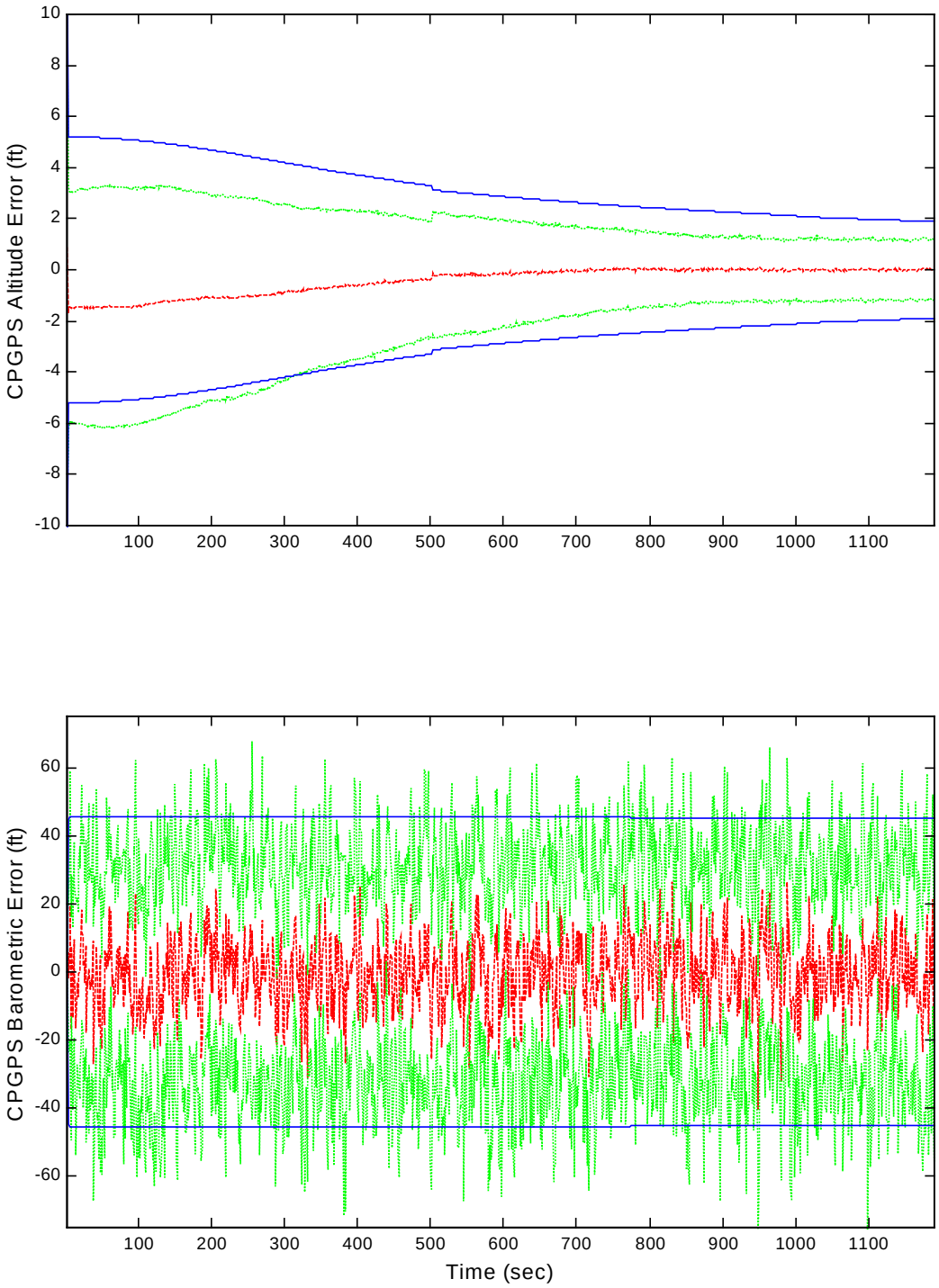

Figure 37. CPGPS Altitude and Barometric Altimeter Bias Errors

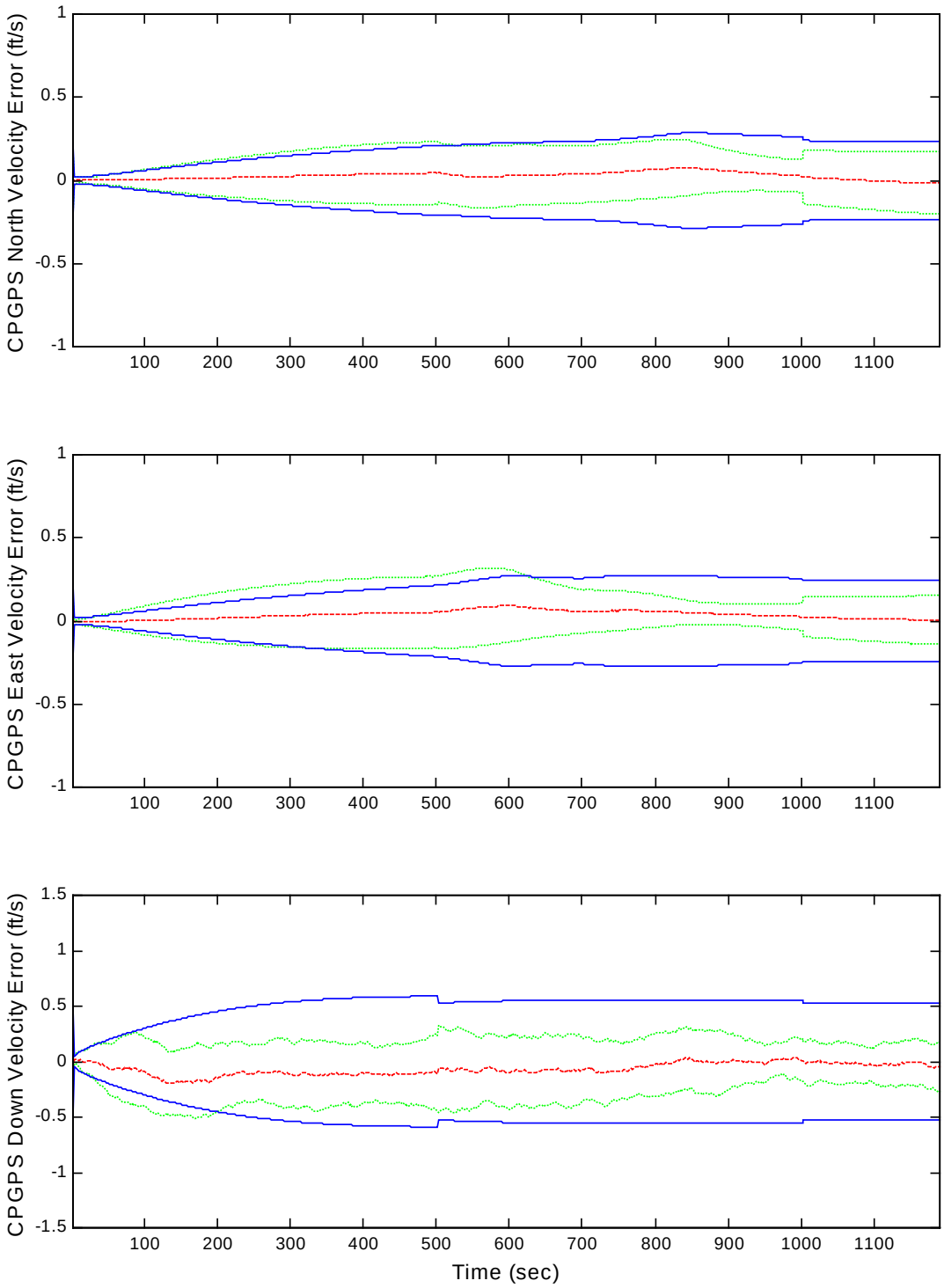

Figure 38. CPGPS North, East, and Down Velocity Errors

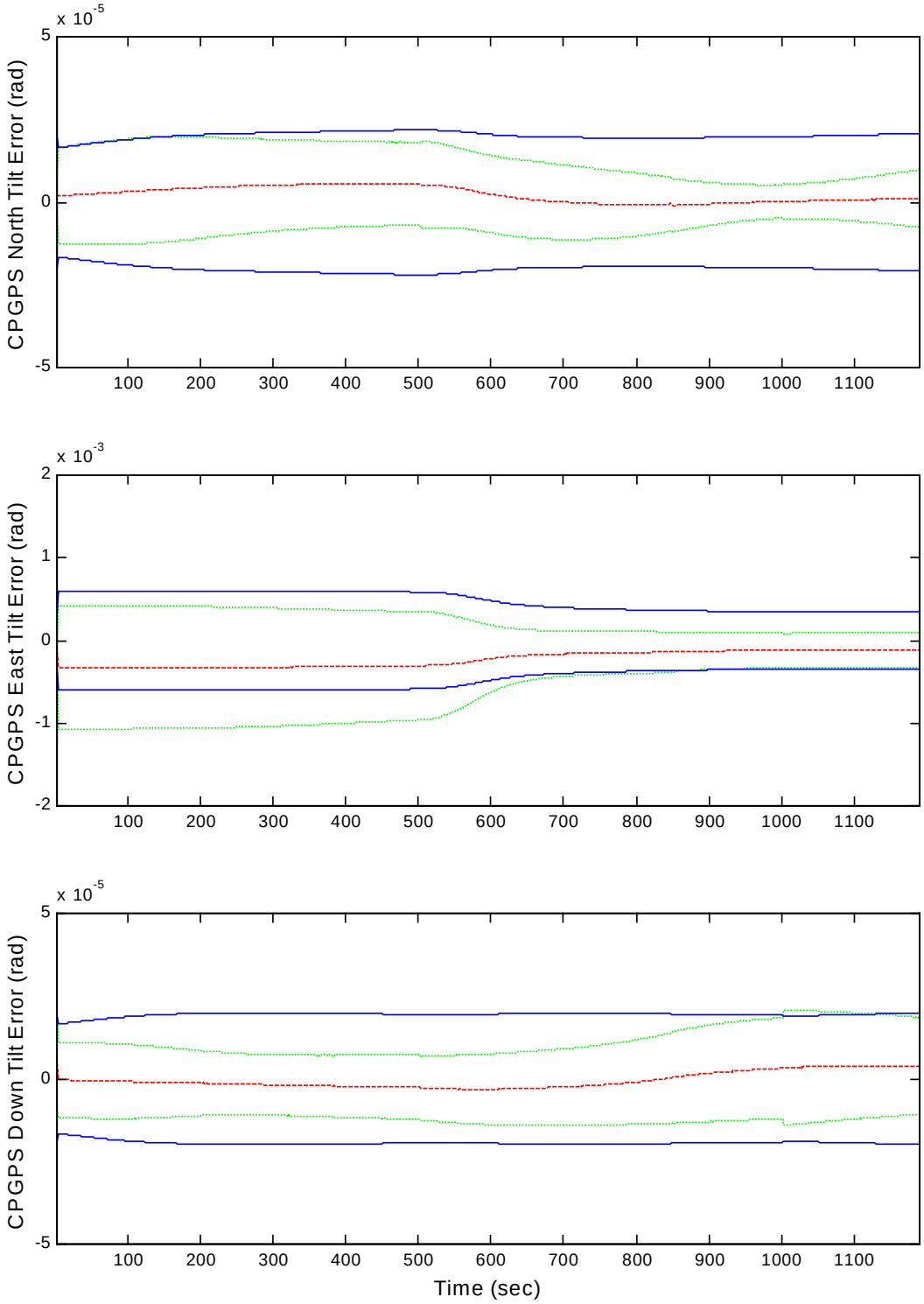

Figure 39. CPGPS North, East, and Down Attitude Errors

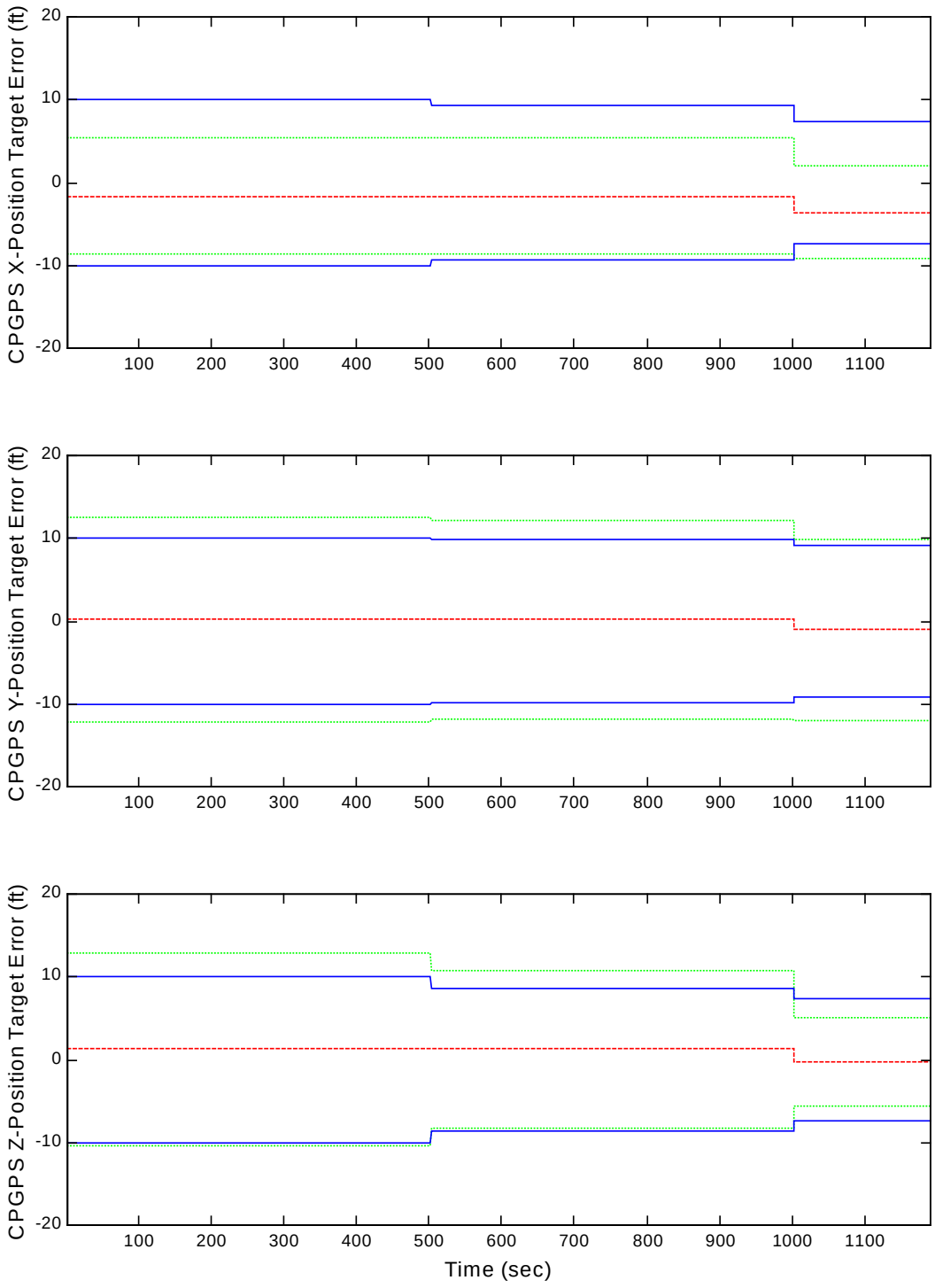

Figure 40. CPGPS SAR X, Y, and Z-Target Position Errors

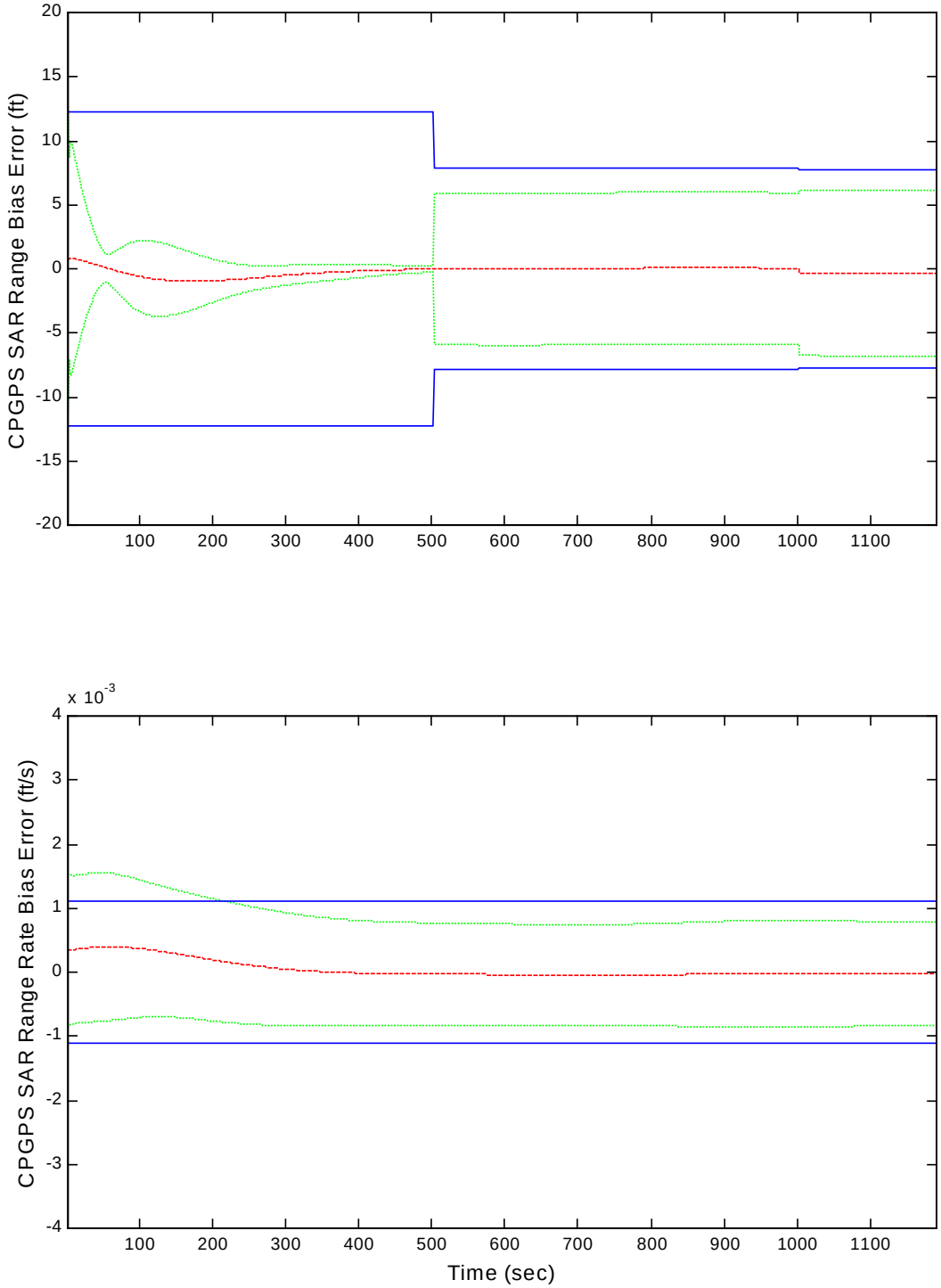

Figure 41. CPGPS SAR Range and Range Rate Bias Errors

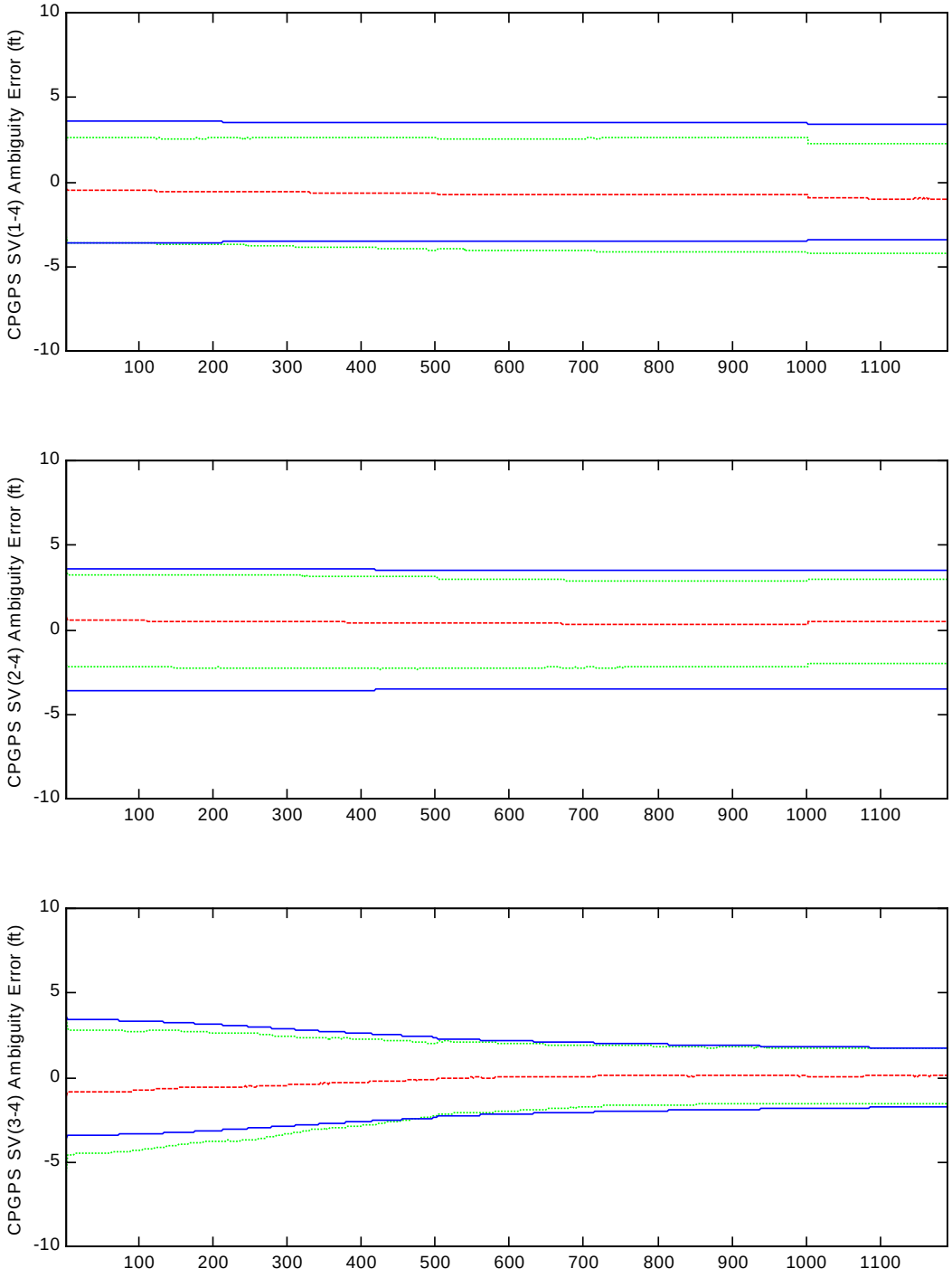

Figure 42. CPGPS Carrier Phase Ambiguity Errors

Appendix F. Flight Profile Plots

The following plots describe the position, velocity, attitude, and attitude rates of the "*U-2Flight*" flight profile generated through PROFGEN. Refer to section 4.2 for a detailed description of the flight profile

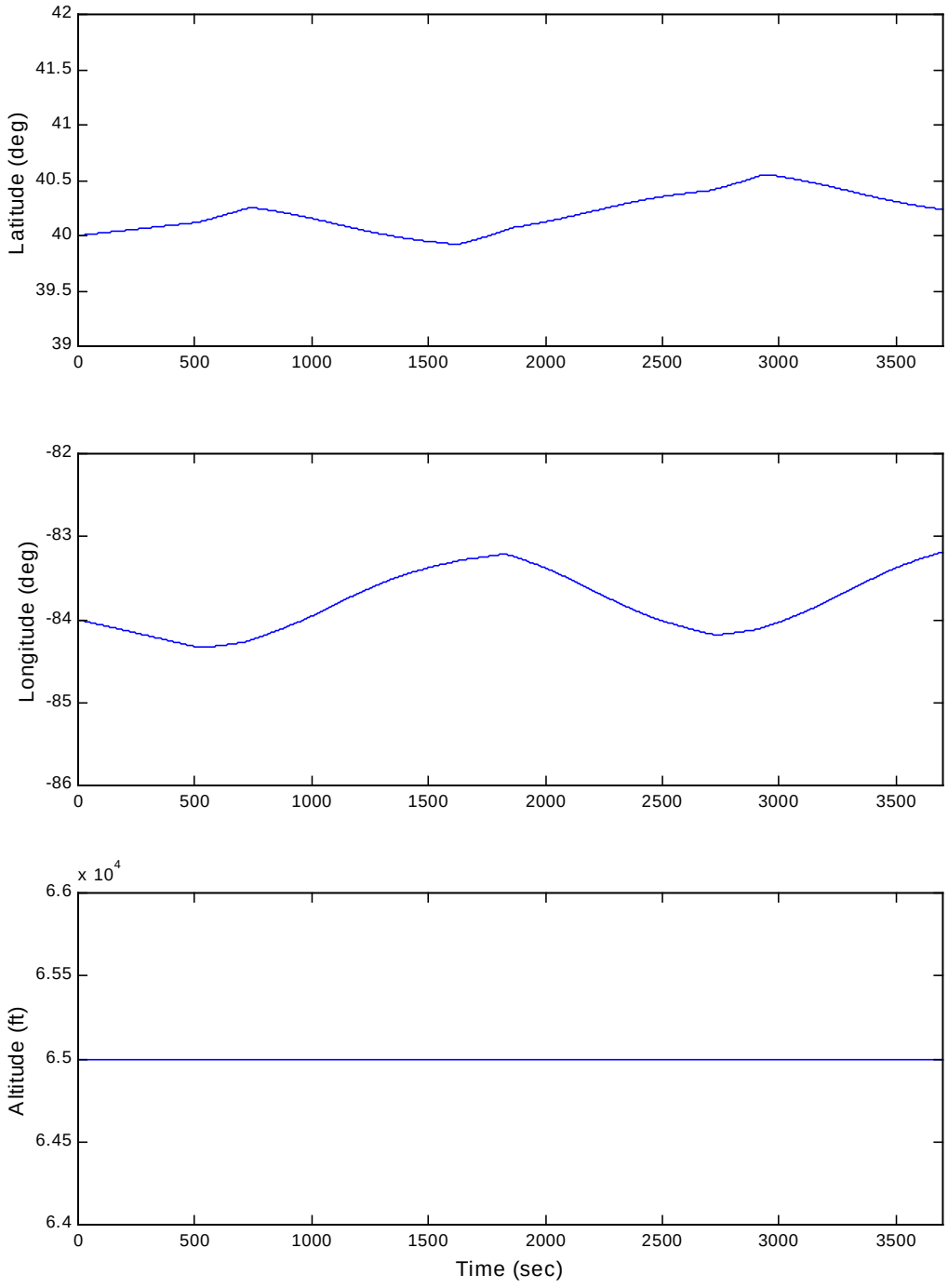

Figure 43. U-2 Flight Profile Latitude, Longitude, and Altitude

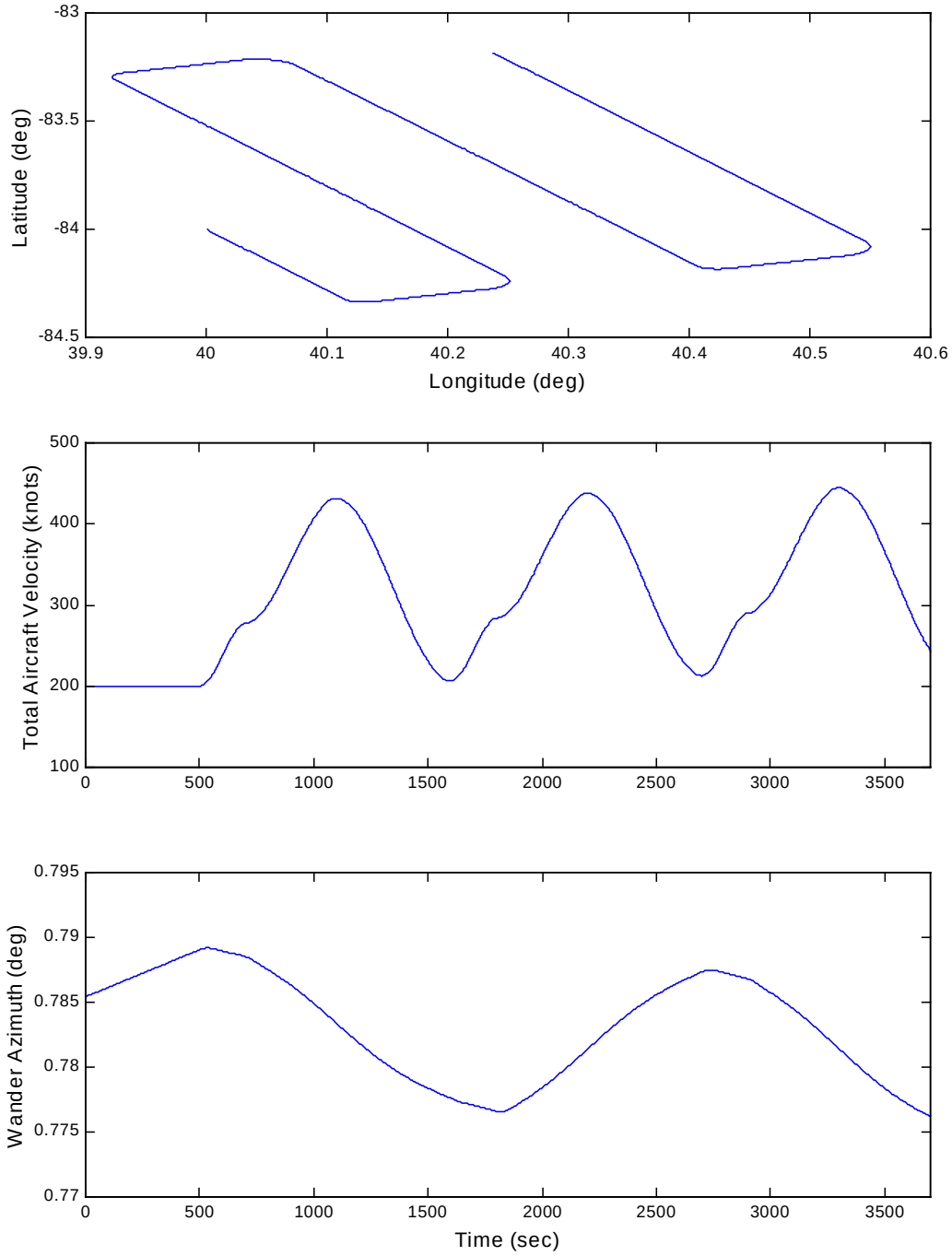

Figure 44. U-2 Flight Profile 2-D Position, Velocity Magnitude, and Wander Angle

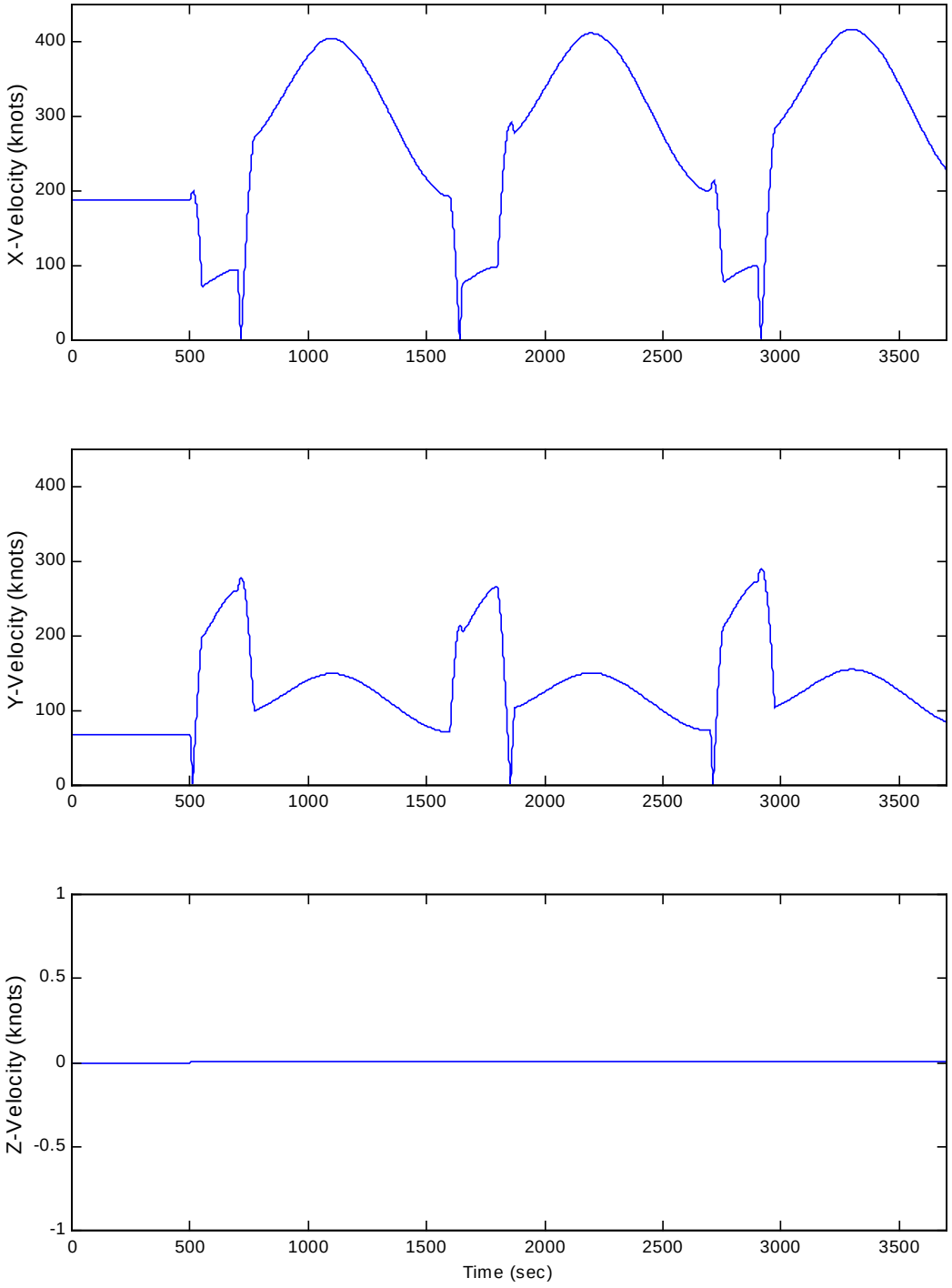

Figure 45. U-2 Flight Profile X-, Y-, and Z-Velocities

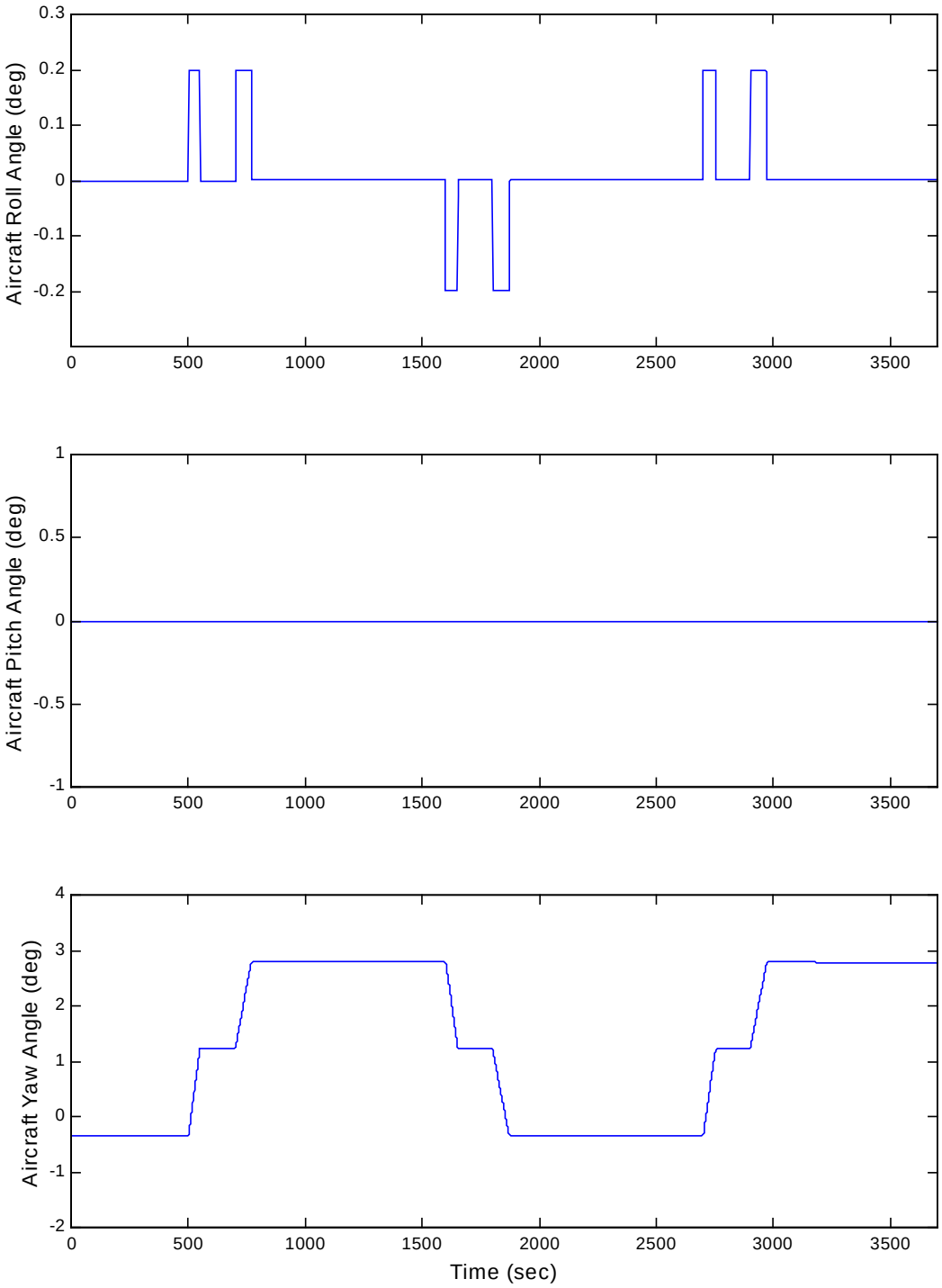

Figure 46. U-2 Flight Profile Roll, Pitch, and Yaw Angles

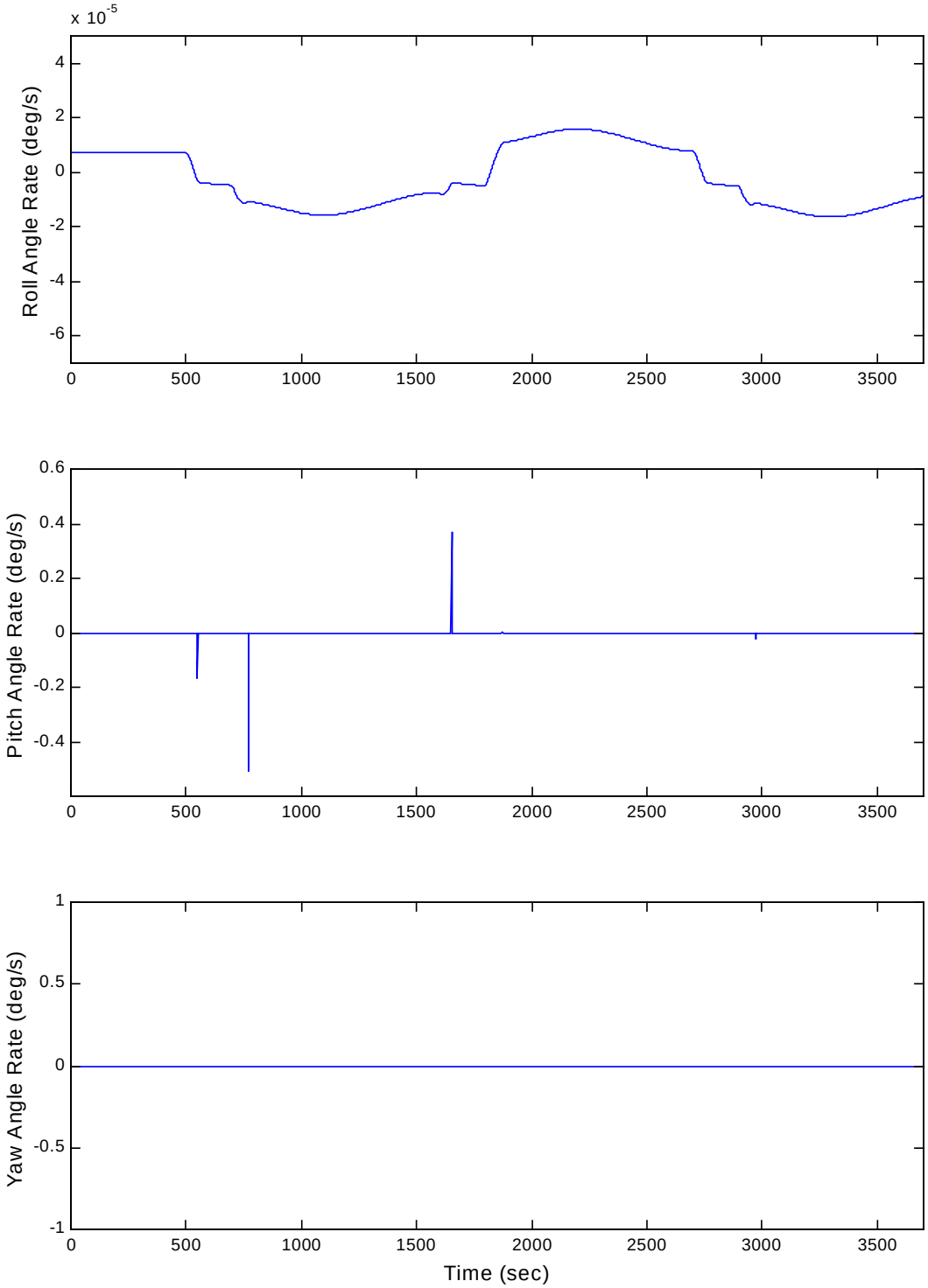

Figure 47. U-2 Flight Profile Roll, Pitch, and Yaw Rates

Bibliography

[1] Miller, Mikel M. *Modified Multiple Model Adaptive Estimation (M^3AE) for Simultaneous Parameter and State Estimation.* Ph.D. dissertation, AFIT/GE/ENG/98-02, School of Engineering, Air Force Institute of Technology, Wright-Patterson AFB, OH, March 1998.

[2] White, Nathan A. *MMAE Detection of Interference/Jamming and Spoofing in a DGPS-Aided INS*. MS thesis, AFIT/GE/ENG/96D-21, School of Engineering, Air Force Institute of Technology, Wright-Patterson AFB, OH, December 1996.

[3] Gray, Robert A. *An Integrated GPS/INS/BARO and Radar Altimeter System for Aircraft Precision Approach Landings.* MS thesis, AFIT/GE/ENG/94D-13, School of Engineering, Air Force Institute of Technology, Wright-Patterson AFB, OH, December 1994.

[4] Maybeck, Peter S. *Stochastic Models, Estimation and Control, I.* New York: Academic Press, Inc., 1982.

[5] Maybeck, Peter S. *Stochastic Models, Estimation and Control, II.* New York: Academic Press, Inc., 1982.

[6] Musick, Stanton H. and Neil Carlson. *User's Manual for a Multimode Simulation for Optimal Filter Evaluation (MSOFE).* Air Force Avionics Laboratory, Wright-Patterson AFB, OH, April 1990. AFWAL-TR-88-1138.

[7] Neilsen, Robert L. *Development of a Performance Evaluation Tool (MMSOFE) for Detection of Failures with Multiple Model Adaptive Estimation (MMAE).* MS thesis, School of Engineering, Air Force Institute of Technology, Wright-Patterson AFB, OH, December 1993.

[8] Negast, William J. *Incorporation of Differential Global Positioning System Measurements Using an Extended Kalman Filter for Improved Reference System Performance.* MS thesis, AFIT/GE/ENG/91D-41, School of Engineering, Air Force Institute of Technology, Wright-Patterson AFB, OH, December 1991.

[9] Lewantowicz, Zdzislaw H. and Randall N. Paschall. "Deep Integration of GPS, INS, SAR, and Other Sensor Information," Proceedings of ION National Technical Meeting 1998.

[10] Sheldon, Stuart N. *An Optimal Parameter Discretization Strategy for Multiple Model Adaptive Estimation and Control*. Ph.D. dissertation, School of Engineering, Air Force Institute of Technology, Wright-Patterson AFB, OH, December 1989.

[11] Layne, Jefferey R. *Integrated Synthetic Aperture Radar and Navigation Systems for Targeting Applications.* WL-TR-97-1185, Air Force Avionics Directorate, Wright-Patterson AFB, OH, September 1997.

[12] Kaplan, Elliott D. *Understanding GPS, Principles and Applications.* Boston: Artech House, Inc., 1996.

[13] Harger, Robert O. *Synthetic Aperture Radar Systems, Theory and Design.* New York: Academic Press Inc., 1970.

[14] Ornedo, Renato S. and Farnsworth, Kenneth A. "GPS and Radar Aided Inertial Navigation System for Missile System Applications," Proceedings of ION National Technical Meeting 1998, Long Beach, CA, January 21-23, 1998.

[15] Abbott, Rich "Synthetic Aperture Radar Location Accuracy Assessment," Lockheed Martin Skunkworks Interdepartmental Communication, ASC/RAP, Wright-Patterson AFB, OH, 8 May 1995.

[16] Grejner-Brzezinska, Dorota A. "Direct Platform Orientation with Tightly Integrated GPS/INS in Airborne Applications," Ohio State University Center for Mapping, Columbus, OH, 1998.

[17] Li, Rongxing "A Study of Referencing Issues in Multi-Platform and Multi-Sensor Based Object Location," AFRL/SNAT, Wright-Patterson AFB, OH, 1998.

[18] Britting, Kenneth R. *Inertial Navigation Systems Analysis*. New York: Wiley-Interscience, 1971.

[19] Vasquez, Juan R. *New Algorithms for Moving-Bank Multiple Model Adaptive Estimation.* Ph.D. dissertation, AFIT/DS/ENG/98-10, School of Engineering, Air Force Institute of Technology, Wright-Patterson AFB, OH, May 1998.

[20] Bohenek, Brian J. *The Enhanced Performance of an Integrated Navigation System in a Highly Dynamic Environment.* MS thesis, AFIT/GE/ENG/94D-01, School of Engineering, Air Force Institute of Technology, Wright-Patterson AFB, OH, December 1994.

[21] Bagley, Daniel, T. *GPS/INS Integration for Improved Aircraft Attitude Estimates.* MS thesis, AFIT/GE/ENG/91D-04, School of Engineering, Air Force Institute of Technology, Wright-Patterson AFB, OH, December 1991.

[22] Baird, Henry D. *Autofocus Motion Compensation for Synthetic Aperture Radar and its Compatibility With Strapdown Inertial Navigation Sensors on Highly Maneuverable Aircraft.* MS thesis, AFIT/GA/ENG/84D-01, School of Engineering, Air Force Institute of Technology, Wright-Patterson AFB, OH, December 1984.

[23] Sokol, Charles W. *Performance Evaluation of a GPS-Aided INS in a Filter-Driving-Filter Configuration.* MS thesis, AFIT/GE/ENG/94M-02, School of Engineering, Air Force Institute of Technology, Wright-Patterson AFB, OH, March 1994.

[24] Knudsen, L. *Performance Accuracy Analysis for the LN-93 Inertial Navigation System Inertial Navigation Unit.* Technical Report: Litton Guidance and Control Systems, January 1985.

[25] Britton, Ryan L. *A Differential GPS Aided INS for Aircraft Landings.* MS thesis, AFIT/GE/ENG/95D-03, School of Engineering, Air Force Institute of Technology, Wright-Patterson AFB, OH, December 1995.

[26] Abbot, Rich *Technical Memo – U-2 System Integration Analysis for ASARS/INS Upgrades.* Lockheed Martin Skunk Works, Interdepartmental Communication, August 1995.

[27] Hirning, James L. *Optimal Kalman Filter Integration of a Global Positioning System Receiver and an LN-94 Inertial Navigation System.* MS thesis, AFIT/GE/ENG/90S-02, School of Engineering, Air Force Institute of Technology, Wright-Patterson AFB, OH, September, 1990.

[28] Hansen, Neil P. *Incorporation of Carrier-Phase Global Positioning System Measurements into the Navigation Reference System for Improved Performance.* MS thesis, AFIT/GE/ENG/93D-40, School of Engineering, Air Force Institute of Technology, Wright-Patterson AFB, OH, December 1993.

[29] Stacey, Richard D. *A Navigation Reference System (NRS) Using Global Positioning System (GPS) and Transponder Aiding.* MS thesis, AFIT/GE/ENG/91M-04, School of Engineering, Air Force Institute of Technology, Wright-Patterson AFB, OH, March 1991.

[30] Mosle, William B. *Detection, Isolation, and Recovery of Failures in an Integrated Navigation System.* MS thesis, AFIT/GE/ENG/93D-28, School of Engineering, Air Force Institute of Technology, Wright-Patterson AFB, OH, December 1993.

[31] The MathWorks, Inc., 21 Elliot Street, Natick, MA 01760. *MATLAB.* December 1997. Version 5.2.

[32] Layne, Jeffery R. *Optimal Performance Analysis of Integrated Synthetic Aperture Radar and Navigation Systems –DRAFT-.* Wright Laboratory, WL/AAAS-3, Wright-Patterson AFB, OH, 1994.

[33] Hall, David L. *Mathematical Techniques in Multisensor Data Fusion*. Boston: Artech House, Inc., 1996.

[34] Hong, Lang. Professor of Electrical Engineering, Wright State University, Fairborn, OH, *EE717 Multisensor Data Fusion Course Notes.* June 1998.

[35] Raquet, John. *Development of a Method for Kinematic GPS Carrier-Phase Ambiguity Resolution Using Multiple Reference Receivers*. Ph.D. dissertation, UCGE Reports Number 20116, Department of Geomatics Engineering, University of Calgary, Calgary, Alberta, Canada, May 1998.

Vita

Captain Brian J. Young was born on November 10, 1971 in Bremerton, Washington. After spending his youth traveling the world, thanks to his father's military career, he graduated from North Kitsap High School in Poulsbo, WA in 1989. He then attended Embry-Riddle Aeronautical University in Prescott, AZ receiving a Bachelor of Science Degree in Electrical Engineering. Having been appointed a Second Lieutenant in the United States Air Force in 1993, his first assignment was to Aeronautical Systems Center (ASC) at Wright-Patterson AFB, OH. After a short term job as Assistant Executive Officer to the ASC Director of Engineering, he moved to the Reconnaissance System Program Office (SPO). At the Reconnaissance SPO, he was assigned to the Airborne Information Transmission Datalink program and Peace Peek German Reconnaissance Aircraft; responsible for systems engineering and planning U-2 and Breguet-1150 flight tests. In 1996 he moved to the Rapid Targeting System as the lead engineer for all Sensor-to-Shooter deployments and demonstrations. In 1997 he was selected to attend the Air Force Institute of Technology to receive a Masters Degree in Electrical Engineering with a focus on GPS, Navigation, and Control. His assignment, following AFIT, is to the Central Inertial Guidance Test Facility at Holloman AFB, NM. Captain Young is married to Corina Young and has three children: Sara, Sadie, and Kemper.